Exploring intersubbands in 2D materials

Doctoral Thesis

by

Peter Schmidt

Thesis Advisor:
Prof. Dr. Frank H.L. Koppens

ICFO – Institut de Ciències Fotòniques
UPC – Universitat Politècnica de Catalunya

December 2018

Thesis committee:

Prof. Dr. Alessandro Tredicucci (University of Pisa, Pisa, Italy)
Prof. Dr. Ido Kaminer (Technion – Israel Institute of Technology, Haifa, Israel)
Prof. Dr. Dmitri K. Efetov (ICFO – Institut de Ciències Fotòniques, Castelldefels, Spain)

Abstract

Transition metal dichalcogenides (TMDs) are semiconducting layered materials that can be isolated up to the limit of a single atomic layer. Next to graphene, they are some of the most intensively studied materials within the larger family of 2D materials. TMDs have been studied thoroughly for both their electrical and optical properties showing intriguing phenomena. All optical studies have so far been limited to the visible to near-infrared wavelength region, exploiting interband transitions from the valence to the conduction band. This is surprising, since the two-dimensionality of TMDs gives rise to additional transitions within the conduction and valence band. These intersubband transitions typically lie in the mid-infrared to THz wavelength region and are a direct consequence of the quantum confinement of the charge carriers' wave functions in the out-of-plane direction, leading to quantized energy states. In systems such as III-V semiconductor heterostructures, intersubband transitions have been well studied and have led to the development of quantum cascade lasers and quantum well infrared photodetectors. Intersubband transitions in TMDs are particularly promising, as the layered nature of 2D materials leads to atomically sharp interfaces between different materials thus limiting the detrimental effects of interface roughness. Furthermore, due to the TMDs' weak van der Waals interactions in the out-of-plane direction, there are no lattice matching conditions. Intersubband transitions can therefore be combined with all kinds of two- and three-dimensional materials, including waveguides and cavities.

In this thesis, we explore intersubband transitions in 2D materials. We first lay the theoretical framework for intersubband transitions in TMDs by using ab initio DFT calculations. We then demonstrate their first experimental observation using scattering scanning near-field optical microscopy (s-SNOM). We employ a doping modulation technique that provides the necessary sensitivity to observe intersubband absorption within a single quantum well. Our measurement technique allows us to quantitatively observe intersubband absorption with a nanometer scale spatial resolution, which is the highest reported spatial resolution of intersubband transitions in any class of material. We perform spectrally resolved measurements, which are in good agreement with our theoretical calculations and show signatures of many-body interactions and non-vertical transitions due to the momentum provided by the sharp AFM tip apex. Finally, we investigate the interaction of intersubband transitions with graphene plasmons and hBN hyperbolic phonon polaritons by transfer matrix method and finite difference time domain simulations and fabricate various van der Waals heterostructures in order to experimentally explore these interactions.

Resumen

Los dicalcogenuros de metales de transición (TMDs) son materiales basados en capas semiconductoras que se pueden aislar hasta una única capa atómica. Tanto el grafeno como los TMDs son los materiales bidimensionales (2D) más estudiados hasta el momento. Los TMDs se han estudiado a fondo debido a sus propiedades eléctricas y ópticas. Sorprendentemente, todos los estudios ópticos realizados hasta la fecha, se han limitado al rango óptico del visible y del infrarrojo cercano. Este rango de frecuencia viene definido por las transiciones entre la banda de valencia y la banda de conducción. Sin embargo, la bidimensionalidad de los TMDs da lugar a transiciones adicionales dentro de la banda de conducción y valencia. Estas transiciones, conocidas como transiciones subbandas, se encuentran normalmente en la región de infrarrojo medio a terahercios, y son una consecuencia directa del confinamiento cuántico de las funciones de onda de los portadores de carga en la dirección fuera del plano. En sistemas como las heteroestructuras semiconductoras III-V, las transiciones subbandas han sido estudiadas ampliamente y han llevado al desarrollo de láseres de cascada cuántica y fotodetectores de pozo cuántico. Las transiciones subbandas en los TMD son particularmente prometedoras, ya que la naturaleza de capas de los materiales 2D conduce a interfaces atómicamente perfectas, lo que limita los efectos perjudiciales acareados por la rugosidad entre interfaces. Además, no hay requerimiento de poseer el complementario estructural de la red cristalina. Por eso, las transiciones subbandas se pueden combinar con todo tipo de materiales bidimensionales y tridimensionales, incluyendo guías de onda y cavidades.

En esta tesis, exploramos las transiciones subbandas en materiales 2D. Primero, establecemos el marco teórico para las transiciones intersubband en TMDs utilizando los cálculos de DFT (ab-initio). Luego demostramos su primera observación experimental utilizando microscopía óptica de campo cercano (s-SNOM). Empleamos una técnica de modulación en el dopaje del TMD, que proporciona la sensibilidad necesaria para observar la absorción intersubband proveniente de un único pozo cuántico. Nuestra técnica de medición nos permite observar cuantitativamente la absorción de subbandas, con una resolución espacial a escala nanométrica, que representa la resolución espacial más alta observada para cualquier clase de material. Realizamos mediciones espectrales, que concuerdan con nuestros cálculos teóricos, y mostramos indicaciones de interacciones de muchos cuerpos y transiciones indirectas debido al momento proveniente de la punta del AFM. Finalmente, investigamos la interacción de las transiciones subbandas con los plasmones de grafeno y los polaritones de fonones hiperbólicos del hBN por simulaciones teóricas y fabricamos varias heteroestructuras de van der Waals para explorar experimentalmente estas interacciones.

Acknowledgments

To Sybille and Konrad for their permanent support, advice and motivation during my entire life. I owe it all to you. A big kiss also to my lovely sister Steffi, who I see way too little and my grandma Lene, who never listens but still manages to grasp it all.

This work would not have been possible without all the people I had the honor to work with. First and foremost, thank you Frank for giving me the opportunity to work on the forefront of science during five years, for providing a fantastic research environment, for sending me to great conferences and giving me the necessary mixture between guidance and freedom needed to develop as a scientist.

A special thanks to the entire NOE group for a great working atmosphere and in particular the 2D team who I have been working closest with: Mathieu, for vivid discussions and for teaching me while I was a still young master's student, Fabien for accompanying the largest part of my PhD, for providing beautiful figures and in particular for reading my entire thesis, and Klaas for always having an open ear to discuss and solve problems of any nature. I also had the privilege to share the office with Mark, who never ceased to amaze me with his encyclopedia-like knowledge and who taught me so much.

Over the years, ICFO has not only been a place for great science but also to find great friends. In particular I would like to thank Achim for way too many beers, Jianbo for teaching me everything about English football and Chinese history, Bernat for being a excellent sparring partner, James for always being up for a good time, Carlotta for ordering Pizza Hawaii (I hope they still let you come back to Italy), Stijn and Bea for providing me shelter in difficult situations, Francesco and Sotiris for introducing me to the tasteful world of atomizers, Gabi for discussing latest news, Bárbara for passing a wonderful time, Noslen and Albert for so many laughters, Nicola for delicious Italian treats, Shuchi for sharing her great Indian culture, and the many more people with whom I shared plenty of beautiful moments, lunches and drinks. Namely: Sebastian, Sebastien, Kevin, Antoine, Iñigo, Iacopo, Laura, Shanti, Ignasi, Mariona, Alberto, Teresa, Michela, Giorgio, Niels, Hitesh, David A. and B., Itai, Tim, Peter, Nicolas, Barbara, Pau, Juan, Lisa, Roland, Miriam, Miquel, Ferran, Gerard, Pamina, Sandra, Joel, Martí, Maria, and the many more I have forgotten.

A big applause goes to the ICFO football team. These games were so much fun and I want to thank you for never injuring me too seriously and that I could always leave the pitch on two feet. A particular thanks goes to Mika for his passionate organization. A note for all newcomers: *NEVER* cancel on short notice.

One of my favorite places in Barcelona has for sure been its beautiful beach. The volleyball matches that we played on Sundays have always been one of the highlights of my week. I want to thank my teammates Jakob, Matteo, Marco, Stefano, Olga, Selim, and whoever else

joined spontaneously for these beautiful days.

Still, there's no place like home. And after having been living for so many years in Barcelona, I am very grateful for still having friends in Germany that make me feel like home when visiting. Special thanks go to Magnus and Olivia, Andrea and Till, Philipp and Franzi, and Felix and Linda for providing me shelter every time that I visit, and Christian and Markus for being reliable squash buddies during the holidays. And as you already know, I am always happy to return the favor when you visit me here, in beautiful Barcelona.

Preface

Before starting my PhD I had already been working for one year in Frank Koppens' group to complete my master's thesis. This thesis was on van der Waals heterostructures designed to act as photodetectors in the visible and near-infrared region. At the beginning of my doctoral thesis I planned to continue on this project and push the detectors towards the telecommunication wavelength range by either using low bandgap semiconductors or interlayer excitons. We started building a PL setup for this experiment but while studying in more depth the literature, I realized that competition in this area was huge, with an unbelievable number of research groups working on similar projects. This gave me the feeling that I had to look for something else. At some point, the idea of intersubband transitions came to my mind. There hadn't been any theoretical nor experimental studies in this field and to my knowledge this topic was not discussed within the 2D community. The more I thought about it the more surprised I got that intersubband transitions in 2D materials had not yet been investigated. Additionally, our labs were well equipped for mid-infrared studies, as we had several FTIR spectrometers available, several quantum cascade and CO_2 lasers and of course our group possessed a large expertise in s-SNOM studies. My first intuition was to fabricate a van der Waals heterostructure acting as a photodetector – similar as I had intended originally but now exploiting intersubband instead of interband transitions. After more thoughts and discussions within the group, we came to the conclusion that we should first characterize the intersubband transitions using FTIR spectroscopy. However, this would require large area few-layer 2D materials, which were not available at that time. Therefore, we decided to start with s-SNOM measurements. When I told Frank about this plan his reply was that 'it is a long shot but you can give it a try'. To our surprise, the experiments started very promising and we observed the first signatures of intersubband absorption directly on the very first samples that we measured. However, we then spent almost two more years collecting the remaining data and understanding the results. In the meantime, we established collaborations with various groups that started investigating intersubband transitions in 2D materials as well. This PhD therefore gave me the unique opportunity to work at the absolute forefront of a newly emerging field within the larger community of 2D materials.

Contents

Introduction

The combination of different semiconducting materials into a single heterostructure allows shaping the electrical potential acting upon charge carriers and therefore the electrical and optical properties of the heterostructure.[1,2] This is fundamental in modern semiconductor technology and has opened the door to major technological applications that have gained more and more importance until today.[3–9] Particular interesting for mid-infrared and terahertz applications is the quantum confinement of charge carriers (electrons or holes) to nanometer scales inside a crystal, which leads to a quantization of the charge carriers' allowed energy states, similar to the quantum mechanical 'particle in a box' problem. Intersubband transitions are the transitions between these quantized energy states (Figure 1). They have first been observed as early as 1974 in the inversion layer of a Si MOSFET.[10] Subsequently, intersubband transitions have been studied extensively, mainly in III-V semiconductor heterostructures grown by molecular beam epitaxy (MBE),[11] where they have first been observed in 1985.[12] Since then, tremendous progress has been made in both fundamental research and applications, leading to commercially available quantum well infrared photodetectors[13,14] and quantum cascade lasers[15] for mid-infrared and THz frequency ranges. However, the epitaxial nature of III-V heterostructures also brings some limitations. Due to the atomic bonds between different materials, a match in the lattice constant of these materials is required in order to grow high-quality heterostructures. This limits the possible materials to combine. Furthermore, the thermal growth leads to diffusion at the interfaces between the materials, giving rise to fluctuations in the well width and hindering the formation of the desired atomically sharp interfaces.

Recently, another material class has sparked tremendous interest within the solid states physics community: Two-dimensional (2D) materials. 2D materials are layered materials that are characterized by strong covalent bonds within individual layers and weak van der Waals interactions between adjacent layers. These weak interactions in the out-of-plane direction allow for the isolation of a single atomic layer from a bulk crystal. The most prominent 2D material is graphene,[16–20] an atomically thin layer of carbon atoms, arranged in a honeycomb lattice structure. It was first observed as early as 1962 by a chemical reduction of graphite oxide.[21] However, it only attracted significant attention after the demonstration of its electrical field effect transistor behavior by Novoselov and Geim in 2004,[22] who isolated a single layer of graphene by thinning highly ordered graphite using conventional scotch tape. It's outstanding importance was underlined by future studies,[23–25] including the demonstration of the room temperature quantum hall effect,[26] which eventually led to Novoselov and Geim being awarded the Nobel Prize in Physics in 2010.[27,28]

Shortly after the discovery of graphene, several other monolayers of 2D materials have been isolated,[29] including semiconductors, semimetals and electrical insulators. Nowadays the family of reported 2D materials also includes ferromagnets,[30,31] topological insulators[32,33] and

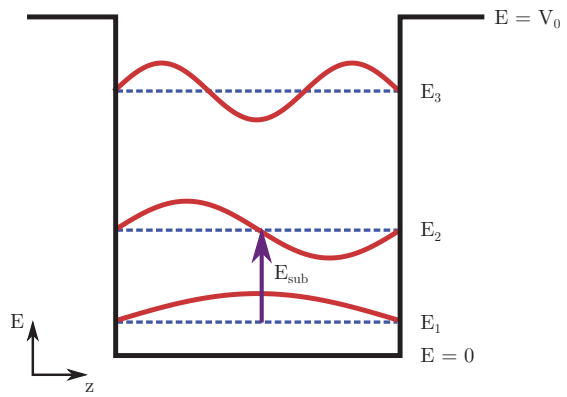

Figure 1: **Schematics of intersubband transitions.** Ideal quantum well potential (black solid line) with a potential height V_0. Charge carriers inside the potential occupy quantized energy states. The charge carrier wave function for the three lowest states is shown in red assuming $V_0 = \infty$. Transitions between the quantized states are called intersubband transitions, as indicated by the purple arrow.

superconductors.[34–39] These materials are not only interesting in itself, but they can also be assembled into layered combinations of different 2D materials – the so-called van der Waals heterostructures.[40,41] In these heterostructures different materials only interact via weak van der Waals forces, giving rise to atomically sharp interfaces without interlayer diffusion as has been confirmed by cross-section TEM images.[17,41,42] Applications of van der Waals heterostructures range from providing an ultraclean environment to graphene in order to achieve room-temperature mobilities >140,000 $\frac{\mathrm{cm}^2}{\mathrm{Vs}}$ and ballistic transport over more than 15 µm at low temperatures,[17] to out-of-plane tunneling devices for logical circuits,[43–46] up to versatile platforms for light matter interaction.[47–50] Each material of a van der Waals heterostructure can individually be contacted electrically, allowing for individual and in-situ control of the doping levels.[43,44,51] Another degree of freedom in van der Waals heterostructures is the alignment angle between individual layers.[52,53] A small rotation between two monolayers of the same material or between two different materials with a small difference in their lattice constants leads to the formation of a moiré pattern, creating an additional periodic potential, whose periodicity depends on the alignment angle.[54–56] In these superlattices new physic emerges, like Hofstadter's butterfly,[57] topological currents[58] and unconventional superconductivity,[59,60] manifesting van der Waals heterostructures as an excellent platform to explore a rich variety of phenomena.

Few-layer 2D materials also naturally form quantum wells, with their well width defined by the number of layers. It is therefore natural to expect intersubband transitions to occur. Surprisingly however, intersubband transitions in 2D materials were a completely unexplored field at the beginning of my PhD thesis. The goal of this thesis is to explore 2D materials as a complementary material for intersubband transitions next to III-V heterostructures. Due to their layered nature, intersubband transitions in 2D materials hold the potential to overcome the aforementioned limitations of III-V semiconductors as they form atomically sharp quantum wells and can be combined with a variety of different materials. During this thesis, we will experimentally observe intersubband transitions in 2D materials, lay their theoretical framework

and explore their interaction with 2D polaritons. The thesis is organized as follows:

- Chapter 1 gives an overview of the relevant properties of TMDs, reviews the well-known theory of intersubband transitions with a particular emphasis on how these transitions are affected by the layered nature of 2D materials, and presents detailed ab initio DFT calculations on intersubband transitions in 2D materials.
- Chapter 2 describes the fabrication and characterization techniques as well as the experimental techniques employed throughout this work.
- Chapter 3 reports the experimental observation of intersubband transitions in 2D materials by using scattering scanning near-field optical microscopy (s-SNOM).
- Chapter 4 explores the interaction between TMD intersubband transitions and graphene plasmons or hBN hyperbolic phonon polaritons by theoretical simulations as well as experimental studies on various van der Waals heterostructures.

1 Theoretical description of intersubband transitions in 2D materials

In this chapter we lay the theoretical framework for intersubband transitions in 2D materials. We first review the properties of transition metal dichalcogenides (TMDs), a group of 2D materials which we will use to study intersubband transitions throughout the thesis. We then review the well-known theory of intersubband transitions, which forms the basis for most of the experimentally studied systems. Next, we discuss how the layered nature of TMDs influences intersubband transitions. Finally, we present a detailed theoretical description for intersubband transitions in TMDs, based on density functional theory (DFT) calculations that have been performed at the Technical University of Denmark and the National Graphene Institute in Manchester in a collaboration as part of my thesis.

1.1 Transition metal dichalcogenides (TMDs)

During this thesis, we will use transition metal dichalcogenides (TMDs) as the 2D material of choice for observing intersubband transitions. TMDs are layered materials with a MX_2 stoichiometry, where the M stands for the transition metal and the X for the chalcogen. The transition metal is sandwiched between two layers of chalcogen atoms and in the common 2H structure that we use for our experiments the chalcogen atoms are aligned vertically, so that the atoms are arranged in a hexagonal lattice structure, similar as in graphene (Figure 1.1a). However, since a monolayer in TMDs consists of a sandwich of three atoms it has a thickness of ∼6.5 Å,[61] which is thicker than a monolayer of graphene (3 Å). The hexagonal lattice of TMDs in real space also leads to a hexagonal lattice in the reciprocal space, as is shown in Figure 1.1b.

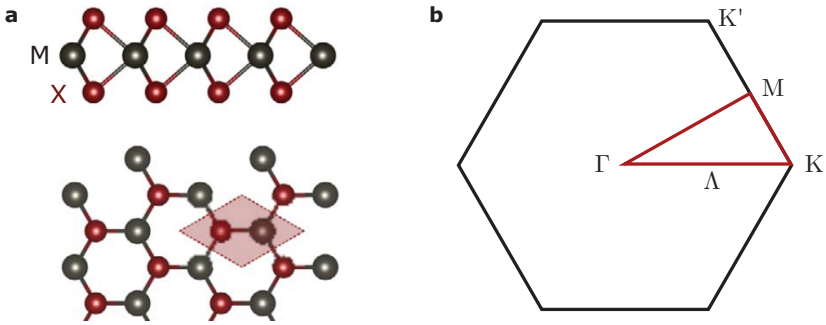

Figure 1.1: **Real-space and reciprocal lattice of 2H-TMDs.** **a**, Lattice structure of a monolayer 2H-MX_2. M stands for the transition metal and X for the chalcogen. A monolayer consists of three layers of atoms, where the transition metal is sandwiched between two layers of chalcogen atoms (top panel). In the 2H-structure the chalcogen atoms are aligned vertically, so that a monolayer of MX_2 forms a hexagonal lattice when viewed from the top (bottom panel). The red shaded area represents the primitive unit cell. Adapted from ref. 62. **b**, First Brillouin zone of 2H-TMDs. The hexagonal real space lattice also leads to a hexagonal reciprocal lattice. High symmetry points are labelled and the corresponding high symmetry lines are shown in red.

The most common TMDs – WS_2, WSe_2, MoS_2 and $MoSe_2$ – are semiconductors with a bandgap in the visible to near-infrared region. Their electrical and optical properties for bulk and thin-film crystals have already been studied in the 1960s.[63] However, they only attracted significant attention after the isolation of a single monolayer[29] and the realization of atomically thin field effect transistors.[61,64,65] TMDs encapsulated in hexagonal boron nitride (which is a common method to reduce substrate-induced disorder) show appealing electrical properties, such as mobilities >30,000 $\frac{\mathrm{cm}^2}{\mathrm{Vs}}$ [42] and the observation of the quantum hall effect.[66] The optical characteristics of TMDs sparked a lot of interest as well, with a single monolayer showing absorption peaks of up to 10% of the incoming light.[67,68] One of the most prominent features of TMDs is the change in bandstructure for varying thicknesses. Few-layer and bulk TMDs have an indirect bandgap, where the valence band maximum is located at the Γ-point of the Brillouin zone and the conduction band minimum is located close to the Λ-point, in the middle between the Γ and K-point of the Brillouin zone. With decreasing TMD thickness

this bandgap increases, which is – for the limit of a monolayer – accompanied by a transition to a direct bandgap at the K-point of the Brillouin zone, as is shown in Figure 1.2a.[68–70] This change in bandgap manifests itself in a drastic (up to 10^4-fold) increase in photoluminescence for a monolayer flake compared to a few-layer thick flake (Figure 1.2b). TMDs are also an excellent platform to study exciton and multi-body effects at room temperature.[71] The spectral response of TMD flakes in the visible and near-infrared wavelength region is dominated by excitonic and multi-body effects, which are extremely strong due to the reduced dielectric screening of the environment.[67,72–74] For example, the exciton binding energy of a monolayer flake is on the order of a few 100 meV[75,76] – in comparison to a few meV for typical 3D semiconductors – and excitonic features are therefore dominant even at room temperature. Recently, a near-unity excitonic reflection has been reported,[77,78] as well as photoluminescence close to the homogeneous exciton linewidth.[79,80]

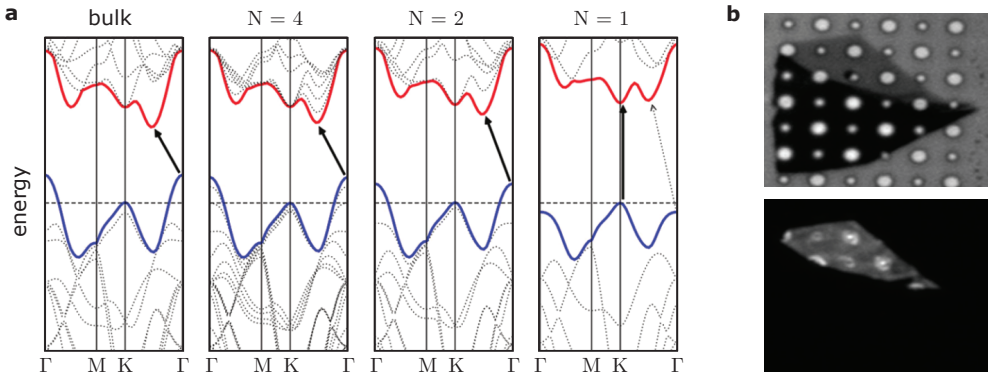

Figure 1.2: **Bandstructure of MoS_2. a**, Calculated bandstructure of MoS_2 for a bulk crystal and few-layer flakes with number of layers N. The solid arrows indicate the smallest energy transitions. This is an indirect transition for bulk and few-layer crystals but becomes a direct transition for a monolayer flake. Adapted from ref. 69. **b**, Top panel: Optical image of a MoS_2 crystal with a monolayer area at the top and few-layers at the bottom on a Si substrate with etched holes. Bottom panel: Photoluminescence (PL) of the same sample. The change in bandgap to a direct transition for the monolayer flake manifests itself in a drastically enhanced PL signal for the monolayer area. The PL of the few-layer area is too weak to be seen in this image. Adapted from ref. 68.

These properties make TMDs to excellent candidates for optoelectronic applications.[71,81,82] TMDs serve as a platform for strong light matter interactions and are building blocks for atomically-thin photodetectors,[47,83,84] light emitting diodes[48,85] and lasers.[86–89] Another intriguing feature of TMDs is the valley-pseudospin locking. This led to the observation of a Hall-voltage without the need of a magnetic field when charge carriers are excited by circularly polarized light,[90] opening the field of valleytronics in 2D materials.[91]

All of the above optical and electrooptical properties exploit interband electronic transitions between the valence and conduction band. However, few-layer TMD flakes also naturally form quantum wells due to their 2D nature. This leads to the formation of additional bands within the conduction and valence band – so-called subbands – as can be seen in Figure 1.2a for few-layer flakes. At the beginning of my PhD thesis, transitions between these subbands had not yet been studied – neither theoretically nor experimentally. In the next sections, we

therefore lay the theoretical framework for intersubband transitions in TMDs.

1.2 General theory of intersubband transitions

In this section we review the well-known theory on intersubband transitions that has mainly been developed in the context of III-V semiconductors. It can be found in standard textbooks, for example refs. 92–94. This general theory can largely be applied to intersubband transitions in other material classes as well, in our case to 2D materials. In the next section we then look at the specific properties of 2D materials and how they influence intersubband transitions.

Intersubband transitions occur within a confined electron system, which has quantized energy levels. Upon absorption of a photon an electron can be excited from one confined electron state to another one. In order to calculate the transition rate W_{if} upon radiation in a real crystal between an initial state Ψ_i and a final state Ψ_f we start by using Fermi's Golden rule:

$$W_{if} = \frac{2\pi}{\hbar} |\langle \Psi_f | H' | \Psi_i \rangle|^2 \delta \left(E_f - E_i - \hbar\omega \right), \tag{1.1}$$

where E_i and E_f are the energies of the initial and final state, $\hbar\omega$ is the photon energy involved in the transition and δ is the Kronecker delta function that ensures energy conservation. $H' = \frac{e}{2m^*} \left(\boldsymbol{A} \cdot \hat{\boldsymbol{p}} + \hat{\boldsymbol{p}} \cdot \boldsymbol{A} \right)$ is the interaction Hamiltonian of an external electromagnetic field. Here $-e$ is the electron charge, m^* is the effective electron mass inside the crystal, $\hat{\boldsymbol{p}}$ is the momentum operator, and $\boldsymbol{A}$ is the vector potential corresponding to an electric field $\boldsymbol{E} = -\frac{\partial \boldsymbol{A}}{\partial t}$. For a linearly polarized plane electromagnetic wave, the electric field can be written as

$$\boldsymbol{E} = E_0 \boldsymbol{e} \cos \left(\boldsymbol{q} \cdot \boldsymbol{r} - \omega t \right), \tag{1.2}$$

with E_0 being the amplitude of the electric field, $\boldsymbol{e}$ the polarization vector, $\boldsymbol{q}$ the wave vector, and $\boldsymbol{r}$ the position vector. Now the corresponding vector potential can be written as

$$\boldsymbol{A} = \frac{iE_0 \boldsymbol{e}}{2\omega} \mathrm{e}^{i(\boldsymbol{q}\cdot\boldsymbol{r} - \omega t)} + c.c. \tag{1.3}$$

We now assume that the wavelength λ of the electromagnetic field is much larger than any characteristic dimension of our system. This is called the dipole approximation. In case of our quantum well systems this approximation is very well fulfilled since we will consider transitions in the mid-infrared region with $\lambda \approx 10$ µm and the quantum well width is typically on the order of a few nanometers. We can then approximate $\mathrm{e}^{i\boldsymbol{q}\cdot\boldsymbol{r}} \approx 1$ and therefore $\hat{\boldsymbol{p}}$ commutes with $\boldsymbol{A}$. We can now write the interaction Hamiltonian H' as

$$H' = \frac{e}{m^*} \boldsymbol{A} \cdot \hat{\boldsymbol{p}}. \tag{1.4}$$

Plugging H' into Equation 1.1 yields for the transition rate W_{if}

$$W_{if} = \frac{2\pi}{\hbar}\frac{E_0^2 e^2}{4m^{*2}\omega^2}|\langle\Psi_f|\,\boldsymbol{e}\cdot\hat{\boldsymbol{p}}\,|\Psi_i\rangle|^2\delta\left(E_f - E_i - \hbar\omega\right). \tag{1.5}$$

In order to evaluate the transition matrix element $\langle\Psi_f|\,\boldsymbol{e}\cdot\hat{\boldsymbol{p}}\,|\Psi_i\rangle$ we can express the electron wave function with the help of a Bloch function

$$\Psi_{\nu,n}\left(\boldsymbol{r},t\right) = u_{\boldsymbol{k},\nu}\left(\boldsymbol{r}\right) f_n\left(\boldsymbol{r}\right). \tag{1.6}$$

Here ν is the band index and n denotes the quantum number of the system (subband index). $u_{\boldsymbol{k},\nu}$ is a periodic function (originating from the atomic orbitals), with the same periodicity as the lattice. This periodic function gives rise to the different bands. $f_n\left(\boldsymbol{r}\right)$ is a slowly varying envelope function. This is a generalized Bloch ansatz, where $f_n\left(\boldsymbol{r}\right)$ reduces to $\exp\left(i\boldsymbol{k}\boldsymbol{r}\right)$, in the case of a bulk crystal. Now, the transition matrix element can be split up into two terms

$$\langle\Psi_f|\,\boldsymbol{e}\cdot\hat{\boldsymbol{p}}\,|\Psi_i\rangle = \underbrace{\boldsymbol{e}\cdot\langle u_{\nu_i}|\,\hat{\boldsymbol{p}}\,|u_{\nu_f}\rangle\,\langle f_{n_i}|f_{n_f}\rangle}_{\text{interband transitions}} + \underbrace{\boldsymbol{e}\cdot\langle u_{\nu_i}|u_{\nu_f}\rangle\,\langle f_{n_i}|\,\hat{\boldsymbol{p}}\,|f_{n_f}\rangle}_{\text{intersubband transitions}}, \tag{1.7}$$

where the first term corresponds to interband transitions and the second term corresponds to intersubband transitions. Since both, $u_{\boldsymbol{k},\nu}$ and f_n form an orthogonal set of functions, interband transitions can only occur between the same subbands (see for example refs. 95,96 for experimental manifestations), while intersubband transitions can only occur within the same band. In the following we are only interested in the second term of Equation 1.7, corresponding to intersubband transitions.

Assuming that the considered heterostructure is isotropic within the x-y plane and that the quantum well is confined to within the z direction, we can separate the envelope wave function $f_n\left(\boldsymbol{r}\right)$ as

$$f_n\left(\boldsymbol{r}\right) = \frac{1}{\sqrt{S}}\mathrm{e}^{i\boldsymbol{k}_{\perp,n}\cdot\boldsymbol{r}_\perp}\phi_n\left(z\right), \tag{1.8}$$

where $\boldsymbol{k}_{\perp,n}$ and $\boldsymbol{r}_\perp$ are the two-dimensional wave and position vectors in the x-y plane of area S, and $\phi_n\left(z\right)$ is the envelope function in the z-direction that depends on the quantum well structure. Now we can evaluate the matrix element for intersubband transitions ($u_{\nu_i} = u_{\nu_f}$):

$$\begin{aligned}\langle\Psi_f|\,\boldsymbol{e}\cdot\hat{\boldsymbol{p}}\,|\Psi_i\rangle &= \langle f_{n_i}|\,\boldsymbol{e}\cdot\hat{\boldsymbol{p}}\,|f_{n_f}\rangle \\ &= \langle\phi_{n_f}|\phi_{n_i}\rangle\,\frac{1}{S}\int dx\,dy\,\mathrm{e}^{-i\boldsymbol{k}_{\perp,n_f}\cdot\boldsymbol{r}_\perp}\left(e_x\hat{p}_x + e_y\hat{p}_y\right)\mathrm{e}^{i\boldsymbol{k}_{\perp,n_i}\cdot\boldsymbol{r}_\perp} \\ &\quad + \delta\left(\boldsymbol{k}_{\perp,n_f} - \boldsymbol{k}_{\perp,n_i}\right)e_z\,\langle\phi_{n_f}|\,\hat{p}_z\,|\phi_{n_i}\rangle.\end{aligned} \tag{1.9}$$

The first term of this equation becomes 0 for different subbands since the envelope functions are orthogonal. Now, the transition rate for intersubband transitions is given as

$$W_{if} = \frac{2\pi}{\hbar}\frac{E_0^2 e^2}{4m^{*2}\omega^2} e_z^2 |\langle \phi_f | \hat{p}_z | \phi_i \rangle|^2 \times \delta\left(\boldsymbol{k}_{\perp,n_f} - \boldsymbol{k}_{\perp,n_i}\right) \delta\left(E_f - E_i - \hbar\omega\right). \tag{1.10}$$

Finally we can choose to write the matrix element in the more common real space notation. For this we exploit the commutation relation $[H_0, z] = \frac{\hbar}{i}\frac{\hat{p}_z}{m^*}$, where H_0 is the unperturbed Hamiltonian of the system. This leads to

$$W_{if} = \frac{2\pi}{\hbar}\frac{E_0^2 e^2}{4} e_z^2 |\langle \phi_f | z | \phi_i \rangle|^2 \times \delta\left(\boldsymbol{k}_{\perp,n_f} - \boldsymbol{k}_{\perp,n_i}\right) \delta\left(E_f - E_i - \hbar\omega\right). \tag{1.11}$$

Several important physical information can be deduced from this representation of the transition matrix element:

- Optical transitions only occur when the polarization of the electromagnetic wave is in z direction, i.e. perpendicular to the layers in the case of 2D materials. This is the well-known polarization selection rule.
- Transitions are only allowed between states with opposite parity. This can be seen by introducing the parity operator $\hat{\sigma}\boldsymbol{r} \equiv -\boldsymbol{r}$. For states with the same parity, the transition matrix element can be written as $\langle \phi_f | z | \phi_i \rangle = \langle \phi_f \hat{\sigma}^* \hat{\sigma} | z | \hat{\sigma}^* \hat{\sigma} \phi_i \rangle = -\langle \phi_f | z | \phi_i \rangle$, for which the only possible solution is 0. This means that only the transitions from 1→2, 1→4, 2→3 etc. are allowed, whereas 1→3, 2→4 etc. are forbidden.
- Within the optical dipole approximation, transitions are vertically in $\boldsymbol{k}$-space ($\boldsymbol{k}_{\perp,n_i} = \boldsymbol{k}_{\perp,n_f}$). That means that we do not assume the photon to transfer momentum.

For the approximation of an infinite square well potential with well width L, the envelope functions can easily be calculated as

$$\phi_n = \sqrt{\frac{2}{L}} \sin\left(\frac{n\pi}{L} z\right). \tag{1.12}$$

The corresponding energy eigenvalues E_n are given as

$$E_n = \frac{h^2}{8m^* L^2} n^2. \tag{1.13}$$

During this thesis we are mainly interested in the transition between the ground state and the first excited state with energy

$$E_{12} = E_2 - E_1 = \frac{3h^2}{8m^* L^2} n^2. \tag{1.14}$$

This approximation of an infinite square well potential is well justified for 2D materials, where the crystals are typically surrounded by large bandgap insulators. It may not hold however, if the potential height is finite or inside a superlattice.

We can now define the dimensionless oscillator strength $f_{n_i n_f}$ in order to compare the transition strength between different transitions

$$f_{n_i n_f} = \frac{2m^* E_{n_i n_f}}{\hbar^2} |\langle \phi_f | z | \phi_i \rangle|^2, \tag{1.15}$$

where $E_{n_i n_f}$ is the transition energy between the considered initial and final states. The oscillator strength obeys the sum rule

$$\sum_{n_f} f_{n_i n_f} = 1 \tag{1.16}$$

We can evaluate $f_{n_i n_f}$ by using the expressions for the infinite square well potential given in Equations 1.12 and 1.13. This yields $f_{12} \approx 0.96$ and $f_{14} \approx 0.03$, showing that transitions from the first to the second subband are much stronger than transitions to higher subbands. Similarly we can calculate the oscillator strengths for transitions from the second subband as $f_{21} \approx -0.96$ (the minus sign represents the emission of a photon), $f_{23} \approx 1.86$ and $f_{25} \approx 0.07$. We see that the transition from the second to the third subband has a large oscillator strength. In our experiments, however, it proves to be difficult to populate the second subband.

We can now proceed to calculate the intersubband absorption coefficient α. We define α as the ratio of the absorbed electromagnetic energy per area S and unit time, $\hbar\omega W_{if}/S$, and the intensity of the incident radiation, $\frac{1}{2} c\eta\epsilon_0 E_0^2$, where η is the refractive index of the absorbing material, ϵ_0 is the vacuum permittivity and c the speed of light in vacuum. We sum α over all possible combinations of initial and final states and take into account their population via the Fermi-Dirac distribution. This yields

$$\begin{aligned} \alpha = & \frac{\hbar\omega}{IS} \sum_{n_i, n_f} \sum_{\boldsymbol{k}_\perp} \frac{2\pi}{\hbar} |\langle \phi_f | \frac{e}{m^*} \boldsymbol{A} \cdot \hat{\boldsymbol{p}} | \phi_i \rangle|^2 \left[f\left(E_{n_i}\right) - f\left(E_{n_f}\right) \right] \\ & \times \delta\left(E_{n_f}\left(\boldsymbol{k}_\perp\right) - E_{n_i}\left(\boldsymbol{k}_\perp\right) - \hbar\omega \right). \end{aligned} \tag{1.17}$$

This equation can be solved analytically and if one assumes a parabolic in-plane dispersion of the subbands we obtain for the $1 \rightarrow 2$ transition at zero temperature T

$$\alpha\left(T = 0\right) = \frac{e^2 \hbar f_{12}}{c\eta\epsilon_0 m^*} n_{2\mathrm{D}} \frac{\gamma}{4\left(E_2 - E_1 - \hbar\omega\right)^2 + \gamma^2}, \tag{1.18}$$

where $n_{2\mathrm{D}}$ is the two-dimensional sheet carrier density of the quantum well. The energy conserving δ-function has also been replaced by a Lorentzian with full width at half maximum γ. When the illumination photon energy $\hbar\omega$ is resonant with E_{12} a particular simple expression is obtained that can be used to estimate the peak absorption strength of intersubband transitions,

$$\alpha = \frac{e^2 \hbar f_{12}}{c\eta\epsilon_0 m^* \gamma} n_{2\mathrm{D}}. \tag{1.19}$$

It is important to note that the peak absorption is proportional to n_{2D} and inversely proportional to m^* and γ.

1.3 Comparison of van der Waals and epitaxial heterostructures

In this section we look at the differences of van der Waals heterostructures with respect to III-V semiconductor heterostructures with particular attention on how these differences influence intersubband transitions. The most striking difference is that epitaxial heterostructures have atomic bonds between different materials while in van der Waals heterostructures different layers are held together by weak van der Waals forces. This has several important consequences. First, the atomic bonds between different materials in III-V semiconductor compounds induce lattice matching conditions that limit the available materials to combine (see Figure 1.3a for typically used materials). A small mismatch in the lattice constant leads to strained heterostructures and the formation of atomic defects,[97] deteriorating the quality of the heterostructure (Figure 1.3b). Additionally, valence mismatch and differences in thermal expansion coefficients need to be taken into account for the material choice.[11] This situation is completely different in van der Waals heterostructure. Due the weak van der Waals interactions between the layers no lattice matching conditions apply and intersubband transitions can be combined with any material within the wide variety of 2D materials.[40,41] Those comprise a wide range of electrical properties, like insulators,[29] semimetals,[22] semiconductors,[29,98] ferromagnets,[30,31] superconductors[34–39] and topological insulators.[32,33] This flexibility opens up new possibilities that are not available in epitaxial heterostructures. Furthermore, 2D materials can be integrated with any crystalline structure, like Si integrated circuits[64,99,100] or cavities.[86–89]

Another difference between van der Waals heterostructures and III-V semiconductor compounds stems from the different assembly methods. III-V heterostructures are grown by molecular beam epitaxy (MBE).[11] It is possible nowadays to grow quantum wells with sub-atomic control of the well width.[103] However, since fractions of atoms cannot be grown this sub-atomic change can only be achieved by averaging quantum well areas with different thicknesses. This variation in thicknesses stems from thermal diffusion during the MBE growth and is a dominant broadening mechanism for absorption and emission linewidths.[104–110] In van der Waals quantum wells on the other hand, different layers can be assembled on top of each other while preserving the truly atomically sharp interfaces, as can be verified by TEM images (Figure 1.4).[17,41,42] This can potentially lead to narrower linewidths, as a major broadening contribution can be suppressed. We note however that the typical stacking approach for assembling van der Waals heterostructures is not yet mature enough for commercial fabrication, although efforts are being made towards mass fabrication.[111]

These mentioned points highlight the potential of 2D materials for intersubband transitions. However, their layered nature also brings some drawbacks. First, the quantum well width in 2D materials cannot be controlled quasi-continuously as in III-V semiconductor heterostructures, but it comes in multiples of the monolayer thickness, which is $\sim$0.65 Å for TMDs.[61] Consequently, the transition energies are also determined by the layer numbers, according to

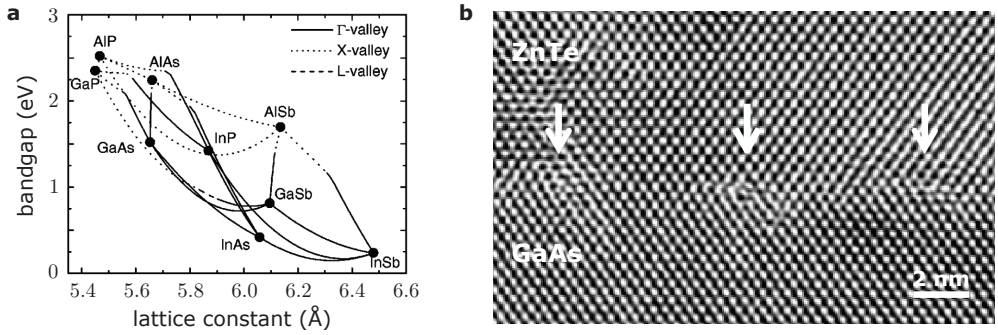

Figure 1.3: **Some commonly used III-V semiconductors and a TEM image of an epitaxial heterostructure.** **a**, Bandgap for common III-V semiconductors (excluding nitrides) as a function of their lattice constant. The displayed materials all show a zinc-blende lattice structure. Lines indicate some of the tertiary alloys. Bandgaps are between the Γ-point in the valence band and Γ, X or L-point in the conduction band, indicated by solid, dotted and dashed lines, respectively. A close match of the lattice constants is required in order to grow strain-free heterostructures. Adapted from ref. 101. **b**, TEM cross-section image of a an epitaxial heterostructure grown by MBE. The heterostructure consists of ZnTe (a II-VI semiconductor, top) and GaAs (bottom). At the interface between the two materials atomic dislocations can be observed (indicated by the arrows), which are the result of the lattice constant mismatch ($\sim$6.1 Å for ZnTe and $\sim$5.65 Å for GaAs) between the two materials. Adapted from ref. 102.

Equation 1.14. Another degree of freedom in III-V heterostructures – in particular for the formation of superlattices – is the use of tertiary or quaternary alloys, which allows for a continuous change in bandgap along the growth direction. In TMDs this has not yet been realized, although tertiary alloys have been grown both as bulk crystals[112–115] as well as monolayers.[116–119]

Intuitively, the layered nature of 2D materials also leads to a larger out-of-plane mass of the charge carriers, due to the reduced coupling between adjacent layers. This is indeed the case, with out-of-plane masses of charge carriers in TMDs being on the order of the electron mass m_0,[120,121] whereas charge carriers in III-V semiconductors have a much smaller mass (e.g. $0.063m_0$ for the electron effective mass in GaAs[122]). A larger electron mass for example leads to reduced intersubband absorption, as can be seen from Equation 1.19. Ultimately, there is an unavoidable trade-off between truly atomically sharp interfaces and low effective masses.

Finally, a more fundamental problem emerges from the layered nature of 2D materials. Ab initio it is not clear that adjacent layers couple well enough in the out-of-plane direction. It could be that charge carriers are confined within their respective layers thus not forming a quantum well potential at all. The fact that the bandgap of TMDs increases with decreasing thickness – which is a confinement effect – indicates that there is coupling between the layers. However, the change from an indirect to a direct gap in the monolayer limit (see section 1.1), indicates that this coupling is dependent on the position within in the Brillouin zone. In section 1.4 we will perform ab-initio calculations to examine this peculiar property in more detail in order to ensure that intersubband transitions can indeed be observed in TMDs.

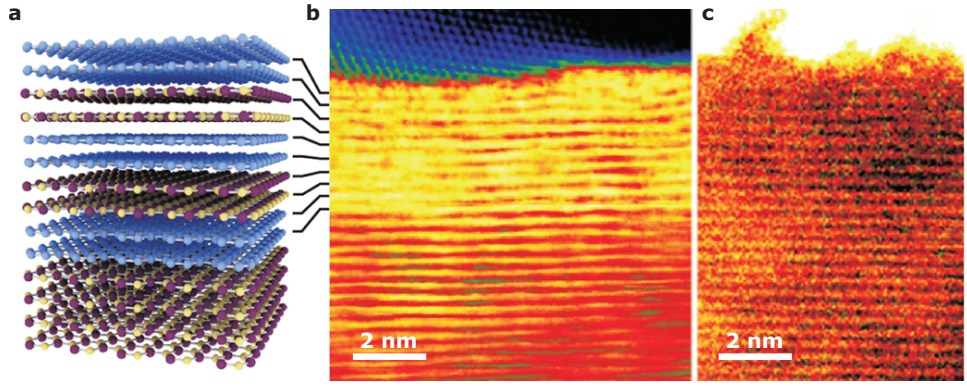

Figure 1.4: **Schematic of a van der Waals heterostructure and corresponding TEM cross-section images. a**, Schematic of the van der Waals heterostructure comprising layers of graphene (atoms in blue) and hexagonal boron nitride (in yellow and purple). **b**, Scanning TEM image of the structure from **a**. The layered van der Waals structure shows atomically sharp interfaces and can be distinguished from the crystalline substrate at the top. **c**, High-angle annular dark field image on the same structure. Adapted from ref. 41.

1.4 Intersubband transitions in TMDs

In this section we present ab-initio density functional theory (DFT) calculations on intersubband transitions in 2D materials. These calculations have been performed as a part of my thesis in collaboration with the groups of Prof. Kirstian Thygesen from the Technical University of Denmark and Prof. Vladimir Fal'ko from the National Graphene Institute in Manchester. We performed all of these calculations for two different TMDs, WSe_2 and MoS_2. In this section we only present the calculations for WSe_2 as this is the material we will mainly use during the experiments. The calculations for MoS_2 are qualitatively similar and can be found in the Appendix A.1.

Sections 1.4.1 and 1.4.2 are based on DFT calculations performed at the Technical University of Denmark. They used the GPAW code,[123] which is available as part of the CAMPOS software. The band structures for the different flakes were calculated at the DFT level with a local density approximation (LDA) exchange correlation functional with a plane-wave basis set. More specifically, a plane-wave basis of 500 eV and a 45×45 k-point grid was used. The reported wave functions are all-electron wave functions as they include the projector augmented wave method (PAW) corrections from the core electrons. As for the geometry of the MoS_2 and WSe_2 the following parameters were used: $a_{MoS_2} = 3.184$ Å and $a_{WSe_2} = 3.319$ Å for the lattice parameters (which is the in-plane metal–metal or chalcogen–chalcogen distance), $d_{S\text{-}S} = 3.127$ Å and $d_{Se\text{-}Se} = 3.359$ Å for the chalcogen-chalcogen distance and $d_{MoS_2} = 6.293$ Å and $d_{WSe_2} = 6.718$ Å for the interlayer distances.

Sections 1.4.3 and 1.4.4 are based on DFT calculations performed at the National Graphene Institute in Manchester. These DFT calculations were performed using a plane-wave basis within the local density approximation (LDA), using the PWSCF ab initio package of Quantum Espresso.[124] The Perdew-Zunger exchange correlation scheme was considered, with fully-

relativistic norm-conserving pseudopotentials, including non-collinear corrections. The cutoff energy in the plane-wave expansion was set to 60 Ry, and the Brillouin zone sampling of electronic states was approximated using a Monkhorst-Pack uniform k-grid of 24×24×1 for all structures. A Methfessel-Paxton smearing of 0.005 Ry was adopted and the total energy convergence was set to less than 10^{-6} eV in all calculations. To eliminate spurious interactions between adjacent supercells, a 20 Å vacuum buffer space was inserted in the out-of-plane direction. The interlayer separations was taken to be the experimental values, with $d_{WSe_2} =$ 6.477 Å.[125]

1.4.1 Bandstructures and out-of-plane wave functions

We first calculate the bandstructure of WSe_2 crystals with layer numbers $N = 2$–6 along the Γ–K axis of the Brillouin zone (Figure 1.5a). The calculations reveal the splitting of both the valence and conduction band into N subbands. This occurs mainly around the valence band maximum and conduction band minimum, which are located at the Γ and Λ-point respectively for few-layer WSe_2.[1] At the Λ-point conduction subbands, the combination of the 2H-stacking and spin-orbit coupling results in an alternating subband structure for even and odd number of layers. For even N, spatial inversion symmetry results in N spin-degenerate subbands, whereas for odd N, the lack of spatial inversion symmetry results in $2N$ spin-polarized subbands. In the valence band at the Γ-point we find each subband to be spin degenerate due to time reversal symmetry.

We now look at the probability distribution of charge carriers in the out-of-plane direction, i.e. the squared wave functions $|\Psi(z)|^2$. For this we integrate the three-dimensional squared wave functions $|\Psi(x, y, z)|^2$ in the x and y direction within the unit cell. Figure 1.5b and c display these in-plane integrated wave functions at the conduction band minimum and valence band maximum, respectively. For $N \geq 3$ one can clearly observe a periodic modulation of the wave functions with the periodicity of the lattice, multiplied by an envelope function. This is in good agreement with the Bloch ansatz from Equation 1.6. We also find a non-zero probability of finding charge carriers between the layers, indicating a good coupling between the layers.

We now examine the out-of-plane wave functions at different points of the Brillouin zone. Figure 1.6 shows the wave functions at the Γ, Λ and K-point of the Brillouin zone for electrons and holes in WSe_2 with $N = 5$. A significant interlayer coupling can only be observed for electrons at the Λ-point and for holes at the Γ-point, which are the minimum of the conduction band and the maximum of the valence band, respectively. At the K-points electrons and holes are completely confined within the layers and there is a vanishing probability of finding a charge carrier between layers. The k-dependent interlayer coupling can be explained by taking into account the spatial distribution of the atomic orbitals making up the highest valence band and lowest conduction band at different points in the Brillouin zone (Figure 1.7).[69,128,130,131]

[1] Due to spin-orbit interactions, the valence band at the K-point of the Brillouin zone gets lifted to higher energies, close to the energies of the Γ-point.[120] The bandstructures in Figure 1.5 actually reveal a change in the valence band maximum between $N = 4$ and $N = 5$ from the K to the Γ-point. In the DFT calculations performed using the PWSCF package of Quantum Espresso this change occurs between $N = 2$ and $N = 3$. Also calculations in literature are not consistent on this topic.[126–129]

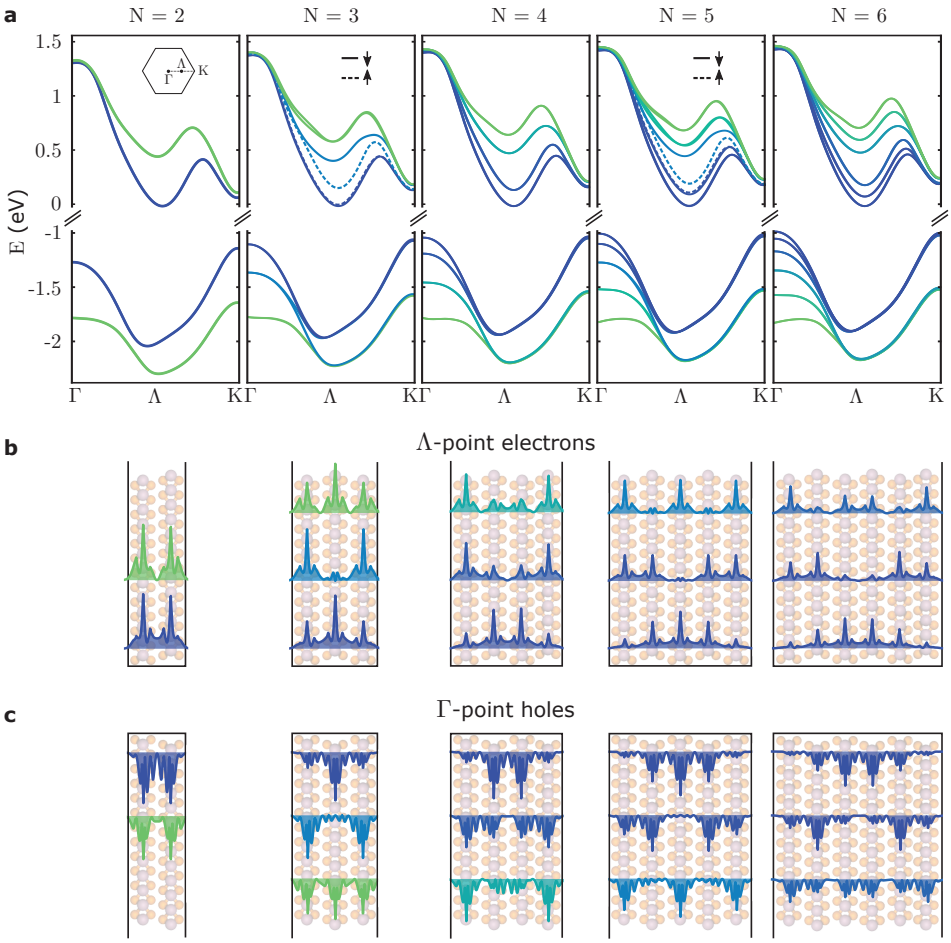

Figure 1.5: **Bandstructure of WSe_2 and wave functions for electrons and holes.** **a**, Ab initio DFT band structure calculations for 2H-WSe_2 crystals with N layers. Shown are the N highest valence bands and N lowest conduction bands, displayed along the Γ–K axis of the hexagonal Brillouin zone, as indicated in the inset. Spin-orbit coupling leads to an additional splitting of the conduction bands for odd N. The lowest conduction bands can then be assigned to spin down (up) and are marked by solid (dashed) lines. **b**, **c**, Calculated out-of-plane wave functions for electrons at the Λ-point of the Brillouin zone (**b**) and holes at the Γ-point (**c**). Shown are the first three subbands (except for $N = 2$ where there only exist two subbands).

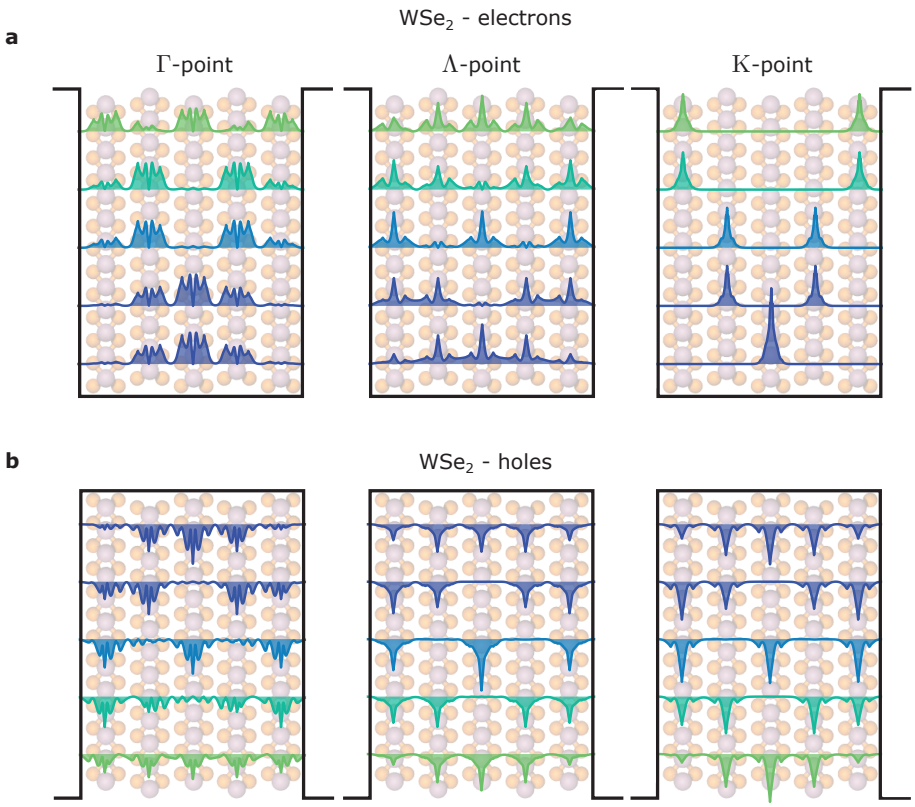

Figure 1.6: **Out-of-plane wave functions of electrons and holes in WSe_2 at selected points in the Brillouin zone.** Calculated out-of-plane wave functions at the Γ, Λ and K-point of the Brillouin zone for electrons (**a**) and holes (**b**) for WSe_2 with $N = 5$. Interlayer coupling can only be observed at the Λ-point for electrons and at the Γ-point for holes. At other points of the Brillouin zone – in particular the K-point – charge carriers are strongly confined within their respective layers.

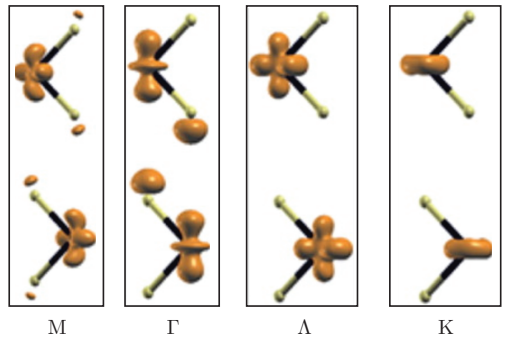

Figure 1.7: **Atomic orbitals in TMDs.** Illustration of the spatial distribution of atomic orbitals in the highest valence band of TMDs at different points in the Brillouin zone. Electronic states at the K-point are made up of transition metal d orbitals located in the middle of a monolayer without an out-of-plane component. At the Γ-point the electronic states consist of a superposition of transition metal d orbitals and chalcogen p_z orbitals with an out-of-plane extension, leading to strong interlayer coupling. Adapted from ref. 130.

Electronic states at the K-point consist of transition metal d orbitals. Since the transition metal is located in the middle of the unit cell – sandwiched between two chalcogen atoms – this leads to a very weak interlayer coupling. On the other hand, electronic states at the Γ-point of the valence band and at the Λ-point of the conduction band consist of a linear combination of transition metal d orbitals and chalcogen p_z orbitals that extend outside the monolayer plane. This leads to a strong interlayer coupling and is also responsible for the transition from a monolayer direct gap (K–K) to a few-layers indirect bandgap (Γ–Λ). The formation of several subbands only occurs at these crystal momenta with a strong coupling between the layers. Since these are precisely the maximum of the valence band and minimum of the conduction band it is possible to dope the first subbands by electrostatic doping, which makes intersubband transitions accessible to be observed in experiments.

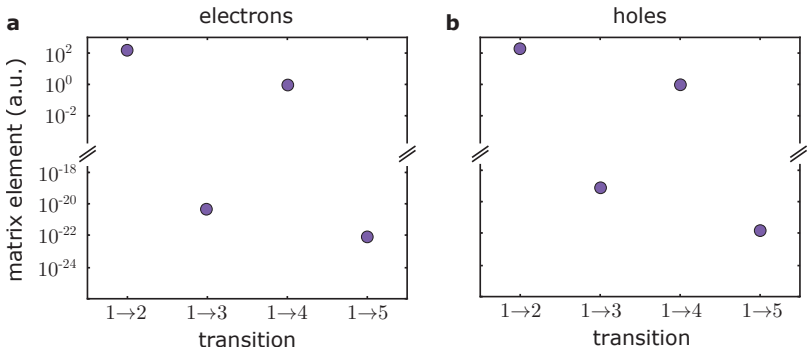

Figure 1.8: **Transition matrix elements for WSe_2.** Calculated transition matrix elements (evaluated as $\langle\Psi_1|\, e^{iqz}\, |\Psi_j\rangle$, $q \to 0$) for electrons at the Λ-point (**a**) and holes at the Γ-point (**b**) for a $N = 5$ WSe_2 crystal. Only transitions from the first subband are shown since it is the only subband that can be populated in our experiment by electrostatic doping.

1.4.2 Transition matrix elements and energies

In order to determine the relevant intersubband transitions we now evaluate the transition matrix elements from the first to the *n*-th subband. We only consider transitions from the first subband since it is the only subband that can be populated with electrons or holes in our experiments by electrostatic doping. The transition matrix element between the first and n-th subband is evaluated as $\langle \Psi_1 | \, e^{iqz} \, | \Psi_n \rangle$ for $q \to 0$ with Ψ_n being the wave function of the n-th subband and q being the momentum in z direction. The calculated transition matrix elements for electrons and holes for a $N = 5$ WSe_2 crystal are shown in Figure 1.8. We see that transitions from the first to the third or fifth subband have a transition matrix element close to zero meaning that these are forbidden transitions. This observation can be explained by the parity selection rule, as we discussed in section 1.2. For the remaining allowed transitions, the transition matrix element from the first to the second subband is about two orders of magnitude larger than the one from the first to the fourth subband and is therefore the only relevant transition that we consider in our experiments.

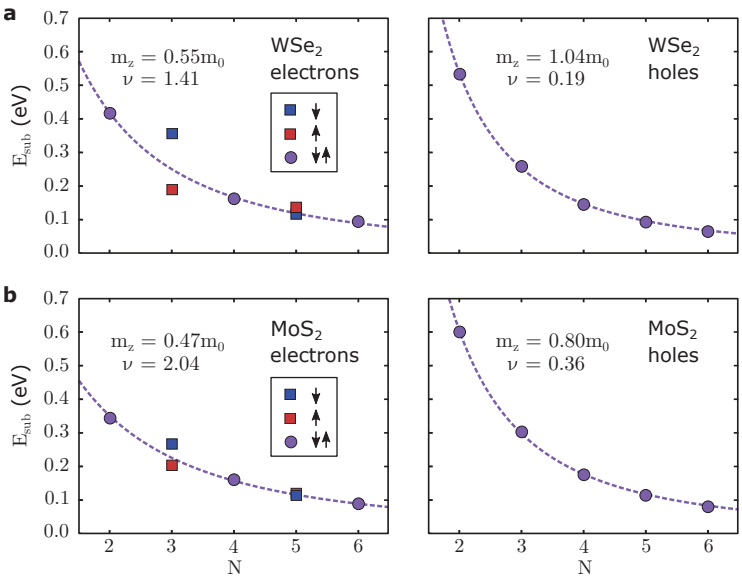

Figure 1.9: **Intersubband transition energies.** Transition energies for electrons in the conduction band and holes in the valence band from the first to the second subband for WSe_2 (**a**) and MoS_2 (**b**) as a function of N. Blue (red) squares correspond to transitions between the spin down (up) polarized subbands, whereas purple circles correspond to transitions between spin-degenerate subbands. The purple dashed line is a fit to the spin-degenerate transitions using the modified infinite square well model $E_{12} = \frac{3h^2}{8m_z d_0^2 (N+2\nu)^2}$ (Equation 1.27). The obtained values for the fitting parameters m_z and ν are displayed in the figure.

Now that we have established the relevant intersubband transitions we can calculate their transition energies E_{12} from the first to the second subband. The calculated energies are shown in Figure 1.9 for WSe_2 and MoS_2 crystals for different N. Electron transitions were evaluated at the Λ-point, while hole transitions were evaluated at the Γ-point of the Brillouin zone, corresponding to the conduction band minimum and valence band maximum, respectively.

For electron transitions with odd N we observe two relevant transition energies due to the spin-orbit induced splitting of the bands.

1.4.3 Analytical description of intersubband transitions in TMDs

A complementary description of the subband structures can be obtained from the limit of many layers ($N \gg 1$). We consider the bulk dispersion near the valence band edge, found at the Γ-point with $k_z = 0$ (Figure 1.10), given by

$$\epsilon(\boldsymbol{k}) = -\frac{\hbar^2 k_z^2}{2m_z} - \frac{\hbar^2 k_{xy}^2}{2m_{xy}}(1 + \zeta k_z^2), \tag{1.20}$$

where k_z is the out-of-plane wave vector and k_{xy} is the in-plane wave vector. The dispersion parameters are: the effective mass in the z-direction $m_z = 1.08m_0$, the in-plane effective mass $m_{xy} = 0.70m_0$, both given in terms of the free electron mass m_0 and were obtained by fitting the bulk dispersions in Figure 1.10, and $\zeta = -5.45$ Å^2, is a parameter related to the non-linearity of the in-plane dispersion.

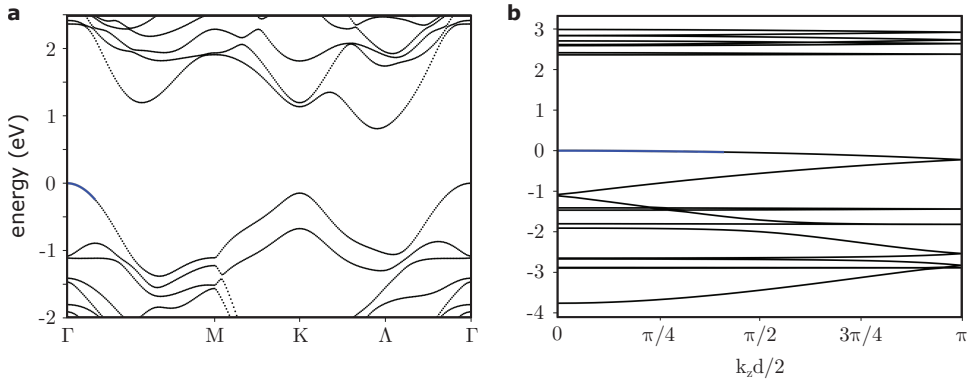

Figure 1.10: **Bulk dispersion of WSe_2.** DFT calculations for bulk WSe_2 showing the in-plane dispersion (**a**) and the out-of-plane dispersion (**b**). The solid blue lines show the fits used to obtain the in-plane and out-of-plane hole effective masses near the Γ-point.

For a finite size crystal we have the following generalized boundary conditions at the top and bottom layers for the electronic wave function $\Psi(z)$, along the z-direction in the crystal,

$$[\pm\nu d_0 \partial_z \Psi(z) + \Psi(z)]_{z=\pm L/2} = 0, \tag{1.21}$$

where d_0 is the interlayer distance, L is the crystal size, ν is a dimensionless parameter of order 1, and the $\pm$ correspond to the top and bottom layers, respectively (Figure 1.11). The physical origin of the parameter ν in the boundary condition is to allow the node of the wave function to be shifted away from the center of the layer, taking into account the band's orbitals extension in the z-direction. In particular, the condition $\Psi(\delta) = 0$ for small

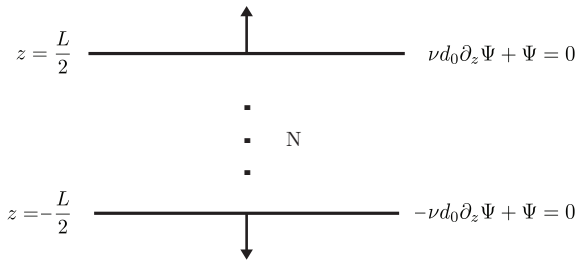

Figure 1.11: **Boundary conditions.** General boundary conditions on the top and bottom layers for a finite size crystal with N layers, interlayer distance d_0, and total size L.

δ translates following expansion to $\psi(0) + \delta\partial_z\psi(0) = 0$, which is the form of the boundary condition.

The general solution to the one-dimensional, time-independent Schrödinger equation in the crystal is given by traveling waves,

$$\Psi(z) = ve^{ik_z z} + ue^{-ik_z z}. \tag{1.22}$$

Inserting Equation 1.22 into the generalized boundary conditions in Equation 1.21 and solving for k_z we get,

$$1 = e^{2i[Lk_z + 2\arctan(\nu d_0 k_z)]}. \tag{1.23}$$

This gives the quantization condition for k_z in the finite size crystal,

$$Lk_z + 2\arctan(\nu d_0 k_z) = \pi n. \tag{1.24}$$

For the top most subbands with large number of layers we have $k_z \sim 1/L \ll 1/d_0$, such that we can approximate the second term as $\arctan(x) \sim x$, finally giving the quantization relation for k_z,

$$k_z = \frac{\pi n}{d_0(N + 2\nu)}. \tag{1.25}$$

Inserting Equation 1.25 into the bulk dispersion (Equation 1.20) gives the description of the valence edge subbands energies and dispersions,

$$E_n(k) = \frac{\hbar^2}{2m_z}\frac{\pi^2 n^2}{d_0^2(N + 2\nu)^2} + \frac{\hbar^2 k_{xy}^2}{2m_{xy}}\left[1 + \frac{\zeta\pi^2 n^2}{d_0^2(N + 2\nu)^2}\right]. \tag{1.26}$$

Using Equation 1.26 we obtain the intersubband transition energies at the Γ-point. In particular, we obtain the formula for the transition energies from the first to the second subband,

$$E_{12} = \frac{3h^2}{8m_z d_0^2 (N+2\nu)^2}. \tag{1.27}$$

This expression is very similar to the formula for the perfect infinite square well potential (Equation 1.14), only that the thickness dependence is modified by the parameter ν. We now use this analytical expression to fit the transition energies calculated by DFT simulations (Figure 1.9) and see that we obtain a good agreement between the two approaches. The values of the fitting parameters m_z and ν are displayed in the figure.

The second term of Equation 1.26 describes the subband in-plane dispersions, with the subband in-plane effective masses as a function of N given by,

$$m_n^{-1} = m_{xy}^{-1}\left[1 + \frac{\zeta\pi^2 n^2}{d_0^2(N+2\nu)^2}\right]. \tag{1.28}$$

1.4.4 Line shape of intersubband absorption

In this section we obtain the line shape resulting from the intersubband absorption of out-of-plane polarized light. The subband states wave functions and in-plane dispersions, which are necessary in order to obtain the optical matrix elements and absorption rates, are taken from a **k·p** tight binding model described in more detail in ref. 121.

The optical matrix element is given by the out-of-plane dipole moment $d_z = e\langle 2|\, z\, |1\rangle$, given by the matrix element of the z coordinate operator between the two subband states. The valence band intersubband absorption line shape is obtained using Fermi's Golden rule for the transition between the first and second top most valence subbands,

$$W_{12} = \frac{2\pi}{\hbar} g_s |E_z(\hbar\omega) d_z|^2 \sum_{\boldsymbol{k}} f(\boldsymbol{k})\delta(E_2(\boldsymbol{k}) - E_1(\boldsymbol{k}) - \hbar\omega), \tag{1.29}$$

where $E_z(\hbar\omega)$ is the out-of-plane electric field component of the incoming light of energy $\hbar\omega$, $g_s = 2$ is the spin degeneracy, $f(\boldsymbol{k})$ is the carrier distribution function, taken to be the Boltzmann distribution for a lightly p-doped sample at room temperature. The delta function ensures energy conservation for the transition between the two subbands with parabolic dispersions with given effective masses, $E_n(\boldsymbol{k}) = E_n(0) - \frac{\hbar^2 k_{xy}^2}{2m_n}$. For the valence subbands in 4-layer WSe_2, we obtain for the effective masses $m_1 = 0.76m_0$, $m_2 = 1.14m_0$ given in terms of the free electron mass, and $E_2(0) - E_1(0) = 154$ meV for the intersubband energy spacing.

Phonon broadening

We consider the contribution of three optical phonon modes taken to have a constant dispersion, homopolar HP (A_1'), longitudinal LO (E'), and out-of-plane ZO (A_2''), with the corresponding irreducible representations of D_{3h} point group given in parenthesis. The detailed derivation of the multilayer electron-phonon couplings is given in ref. 132.

To model the multilayer phonon modes, we approximate the phonons in each layer to be degenerate and independent, allowing to form linear combinations of the phonons in each layer, forming N modes for a given phonon type (HP, LO and ZO), with N the number of layers. The carrier in a given subband state has components on all layers, such that the intersubband phonon scattering matrix element is given by the coupling of the carrier's component on each layer with the phonons in all layers,

$$M_{\mu,\nu}(\boldsymbol{q}) = \frac{1}{\sqrt{N}} \sum_j g_\mu(\boldsymbol{q}) f_\nu(j) c^*_{1,j}(\boldsymbol{q}) c_{2,j}(0). \tag{1.30}$$

The summation is taken over the number of layers N, $g_\mu(\boldsymbol{q})$ is the carrier-phonon coupling for the given phonon mode μ with wave vector $\boldsymbol{q}$, $c_{n,j}(\boldsymbol{k})$ is the amplitude of the carrier wave function in subband n with wave vector $\boldsymbol{k}$ on layer j, and $f_\nu(j)$ is the phase of the given multilayer phonon mode on layer j, $(\nu = 1, .., N)$. The broadening is given by $\gamma = \hbar/\tau$, with the total scattering rate given by Fermi's golden rule,

$$\begin{aligned} \tau^{-1} &= \frac{m_1}{\hbar^2} \sum_{\mu,\nu} |M_{\mu,\nu}(q_*)|^2 \Theta(E_2 - E_1 - \hbar\omega_\mu)[1 + n(\hbar\omega_\mu)]; \\ q_* &= \sqrt{\frac{2m_1}{\hbar^2}(E_2 - E_1 - \hbar\omega_\mu)}. \end{aligned} \tag{1.31}$$

Here the summation is over the three phonon modes μ = HP, LO and ZO, with $\hbar\omega_\mu$ the phonon energy and $n(\hbar\omega_\mu) = \frac{1}{e^{\hbar\omega_\mu/k_B T} - 1}$ is the phonon occupation given by the Bose-Einstein distribution. The summation over ν corresponds to the N multilayer phonon modes for a given phonon μ, with electron-phonon matrix element $M_{\mu,\nu}(q)$, and the Heaviside function Θ restricts the phonon induced intersubband relaxation such that the phonon energy must be smaller than the intersubband energy spacing. The energy conservation in the scattering process sets the emitted phonon wave vector to be q_*.

The carrier-phonon coupling for the HP phonon mode is modeled through the phonon induced deformation potential, $D = 2.2$ eV/Å for Γ-point holes in monolayer WSe_2.[133] The LO phonon mode coupling is modeled through the phonon induced electrostatic potential due to the polar nature of the material and the in-plane Born effective charge $Z = -1.08$ for WSe_2.[132] Similarly, the ZO phonon coupling is modeled through the phonon induced out-of-plane dipole, with the out-of-plane Born effective charge, $Z_z = -0.12$ for WSe_2.[134] Summing the contributions of the HP, LO and ZO phonons results in a broadening of $\gamma = 0.66$ meV in WSe_2 with $N = 4$ for low temperatures. At room temperature, this broadening increases to a few meV due to the thermal occupation of phonon modes (∼2–3 meV for hole intersubband transitions in WSe_2[121]) and is therefore on the same order of magnitude as the phonon-induced broadening in III-V semiconductors.[105,106]

Thermal broadening

Another broadening mechanism stems from different in-plane effective masses of different subbands. For parallel subbands (meaning equal masses), vertical intersubband transitions

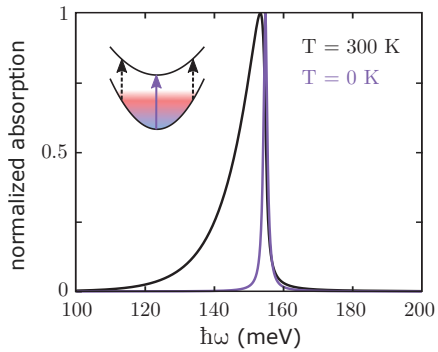

Figure 1.12: **Simulated absorption of intersubband transitions in WSe_2.** Simulated absorption including thermal and phonon broadening. At $T = 0$ K thermal broadening is suppressed and the linewidth is dominated by phonon broadening with a full width at half maximum $\gamma = 0.66$ meV. At room temperature thermal broadening becomes larger than the phonon broadening and governs the line shape, with a linewidth $\sigma = 5.9$ meV and a tail towards lower energies. Calculations were made for transitions from the first to the second subband of the valence band in WSe_2 with $N = 4$. The schematic shows possible transitions for $T = 0$ K (purple solid line) and $T = 300$ K (black dashed lines).

from thermally excited carriers would have the same energy as transitions from the bottom of the subband. However, in WSe_2 with $N = 4$ we obtain $m_1 = 0.76m_0$ and $m_2 = 1.14m_0$ for the in-plane masses of the first two valence subbands. This means that the second subband is flatter than the first one, leading to a lower transition energy of thermally excited charge carriers for transitions from the first to the second subband. The resulting thermal broadening of the absorption is given by

$$\sigma = \left(1 - \frac{m_1}{m_2}\right) k_B T \log 2, \tag{1.32}$$

for low-doped crystals with the Fermi energy $\epsilon_F \ll k_B T$. At room temperature this results in a broadening of $\sigma = 5.9$ meV for 4-layer WSe_2 and is therefore larger than the phonon induced broadening.

We can now compare the different broadening mechanisms. At low temperatures, thermal broadening is small and phonon broadening governs the linewidth. We can introduce phonon broadening by replacing the delta function in Equation 1.29 by a Lorentzian with full width at half maximum γ. At room temperature, the thermal broadening due to different effective masses of the subbands becomes dominant over phonon broadening. Thermal broadening also results in an asymmetric line shape, with a tail towards lower energies. The resulting line shapes are presented in Figure 1.12. In addition to the two mentioned broadening mechanisms there might be additional contributions to the linewidth due to fluctuations in the quantum well potential acting upon the charge carriers. These fluctuations can for example be caused by interface roughness, substrate induced disorder or defect induced disorder. We assume the effect of interface roughness to be small in 2D materials due to their layered nature and substrate induced disorder can be reduced by encapsulation in hexagonal boron nitride, which

provides atomically flat surfaces. However, the effect of defect induced disorder is hard to quantify and it remains to be seen if it has a significant influence on the linewidth.

2 Fabrication and experimental methods

In the first part of this chapter we introduce the fabrication and characterization methods used throughout this work, from the exfoliation of 2D materials to the assembly of van der Waals heterostructures up to the formation of one-dimensional contacts to graphene.
In the second part we then discuss the working principle of the s-SNOM and introduce a model to quantitatively recover the absorption of the measured 2D material. Finally, we identify the main noise sources of our experiments and demonstrate solutions that allow us to suppress this noise and enhance the signal to noise ratio.

2.1 Fabrication and characterization methods

In order to observe intersubband transitions in TMDs, we need TMD crystals with thicknesses of a few atomic layers. There are two main approaches that can be distinguished to obtain few-layer thick TMDs. The thinning of a bulk crystal by mechanical[22,29] or liquid-phase exfoliation[135] or layer-by-layer growth using techniques such as chemical vapor deposition (CVD),[136,137] chemical vapor transport (CVT)[138] or van der Waals epitaxy.[139] Generally, the use of growth methods results in large area flakes and is therefore a promising path for applications. However, the defect density in the grown films is still significantly higher than in mechanically exfoliated flakes.[140] Furthermore, for our work it is important to obtain flakes with sufficiently large areas of constant layer numbers $N \approx 4$–5, since this is when intersubband transitions occur in the mid-infrared wavelength region. It has been proven difficult for a long time to accurately control N when using layer-by-layer growth and experiments have therefore so far almost exclusively been limited to monolayer films. Recently, however, progress has also been made towards the growth of few-layer TMDs with an accurate control of N and wafer-scale few-layer TMD flakes can even be purchased commercially nowadays (for example from 2DLayer). This is promising for future large-area experiments on intersubband transition in TMDs. However, it remains to be seen if the surface is atomically flat over the whole area of the crystal and if the different layers couple well to each other, which is essential for the formation of a quantum well potential. For our work we therefore chose to use mechanical exfoliation to obtain few-layer TMD flakes since it yields the lowest defect densities, ensures that layers are coupled well and that N is well defined. We employed the same mechanical exfoliation technique when other 2D materials were required, such as graphene or hexagonal boron nitride.

2.1.1 Mechanical exfoliation and characterization

For the mechanical exfoliation of TMD flakes we either use a wafer processing tape (for example R1011 from Ultron Systems) or an adhesive polymer (gelfilm from Gel-Pak®). Both approaches leave no detectable residues on the TMD flakes during the exfoliation process. The gelfilms are more cumbersome to work with but result in larger thin flakes and are therefore usually our method of choice for the exfoliation of TMD flakes. For the exfoliation process, we first place a bulk TMD crystal (commercially available from HQgraphene) in between two gelfilms and apply gentle pressure from both sides. After the removal of the bulk crystal, thinner TMD crystals adhere to the gelfilm. We then repeatedly bring the two gelfilms in contact and separate them again, thinning the TMD crystal with each repetition. After several iterations (3–4 for the exfoliation of TMD flakes) we bring the gelfilm in contact with the target substrate, apply uniform pressure and remove the gelfilm as slowly as possible. The slow removal of the gelfilm is critical, as it ensures that the majority of the flakes stick to the target substrate.

As a substrate we use a highly doped Si wafer (from UniversityWafer, Inc.) covered by a thin oxide layer. This field effect transistor (FET) geometry allows us to electrostatically dope the TMD flake by applying a backgate voltage between the Si and TMD. For the oxide layer it is most common to use commercially available 285 nm thermally grown SiO_2,

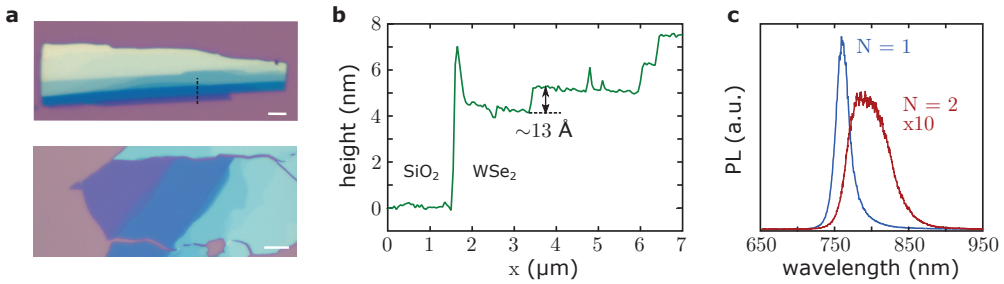

Figure 2.1: **Optical contrast of exfoliated TMD flakes. a**, Optical microscope images of exfoliated WSe_2 flakes on a Si/SiO_2 substrate. The images were taken with an Axio Scope.A1 microscope from Zeiss with 50x magnification. Different layer numbers can be identified by their different colors. The scale bars correspond to 5 µm in both images. **b**, AFM scan along the black dashed line in **a**. The indicated step of 13 Å corresponds to a step of two monolayers. There is a systematic measurement offset of 1–2 nm from SiO_2 to the first TMD layer. **c**, PL measurements of an exfoliated WSe_2 flake placed on a SiO_2 substrate taken at an illumination wavelength of 532 nm. Monolayer areas can be identified by their largely increased PL signal compared to few-layer areas.

as it provides excellent contrast to identify monolayer graphene and TMD flakes under the optical microscope due to optical interference.[141] For our experiments it is sometimes also advantageous to use HfO_2 as an oxide since it does not have phonons in the mid-infrared region.[142] In this case we grow a ~30 nm thick layer of HfO_2 on a bare Si wafer using atomic layer deposition. As a drawback, the TMD flake density after exfoliation is significantly lower on HfO_2 than on SiO_2 and it is furthermore much more difficult to identify different layer thicknesses under the microscope since HfO_2 provides a worse optical contrast.

Exfoliated TMD flakes come in random shapes and sizes, often with terraces of different layer numbers within a single flake. Figure 2.1a shows optical microscope images of typical exfoliated few-layer TMD flakes on a SiO_2 substrate. For our experiments it is crucial to reliably identify the number of monolayers N in a particular region of a flake. For this we use a combination of optical contrast and atomic force microscopy (AFM). The resolution of AFM is sufficiently high to measure a monolayer step of a TMD flake and it is therefore an excellent tool to determine the number of layers of a terraced flake, as is shown in Figure 2.1b. However, AFM produces a varying offset of 1–2 nm when measuring the step from the substrate to the first TMD layer. It is therefore necessary to determine N of at least one area of the exfoliated TMD flake, from which all other thicknesses can be deduced by AFM measurements. Luckily it is possible for $N = 1$–4 to reliably identify N just by the color of the flake under the optical microscope.[1] A monolayer area can additionally be identified by the increased photoluminescence (PL) compared to other thicknesses, as is shown in Figure 2.1c. For the PL measurements we assembled a custom setup based on the Andor SR193i spectrometer.

Additionally, we performed Raman spectroscopy (using the commercially available Renishaw inVia^{TM} system) to identify N of a TMD flake. The spacing between the two different TMD

[1] This requires some patience and experience but one for sure gains both of these skills during the several years of a PhD.

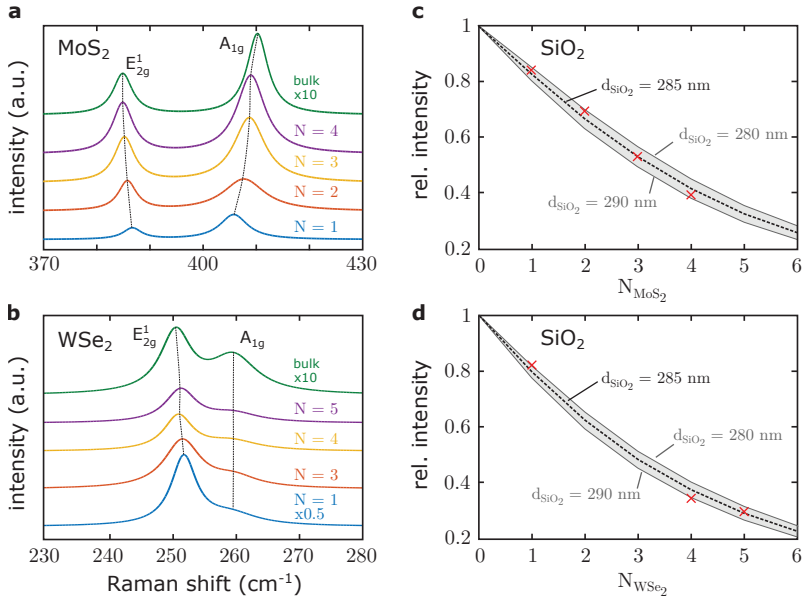

Figure 2.2: **Raman spectroscopy of TMDs. a**, **b**, Measured Raman signals for MoS_2 (**a**) and WSe_2 (**b**) for areas of different number of layers N within the same flake. The dashed lines are guides to the eye for the two vibrational modes E^1_{2g} and A_{1g}. E^1_{2g} is an in-plane movement of the atoms, while A_{1g} is a movement in the out-of-plane direction. Spectra of the different layer numbers are offset for clarity. **c**, **d**, Measured relative intensity of the SiO_2 phonon mode (red crosses) underneath an exfoliated MoS_2 flake (**c**) and WSe_2 flake (**d**), normalized to the intensity without TMD flakes. The dashed black lines are calculations according to ref. 145 for a SiO_2 thickness of 285 nm. The shaded area corresponds to a varying SiO_2 thickness between 280 and 290 nm. All measurements were taken at an excitation wavelength of 532 nm.

Raman modes E^1_{2g} and A_{1g} increases for increasing N, providing a signature for the number of layers.[143,144] However, this change is not very pronounced for both MoS_2 and in particular WSe_2 (Figures 2.2a and b). Furthermore, the measured Raman signals depend on many factors like the quality and strain of the flake, its intrinsic doping, the dielectric environment and illumination wavelength, making a reliable identification of N very hard. A more suitable method makes use of the decrease in intensity of the underlying SiO_2 substrate Raman signal for increasing N.[145] The relative intensity of the SiO_2 phonon is shown in Figures 2.2c and d for an exfoliated MoS_2 flake with $N = 1$–4 and a WSe_2 flake with $N = 1$, 4, 5. In both cases, the intensity of the SiO_2 phonon matches well with the calculations. We therefore use Raman spectroscopy of the substrate phonon as a complementary method to determine N.

Raman spectroscopy is furthermore an excellent tool to distinguish monolayer graphene flakes from few-layer graphene flakes.[146,147] In the monolayer case the 2D Raman peak has a single Lorentzian shape and the $\frac{2D}{G}$ ratio is > 2. Already for bilayer graphene the 2D peak becomes non-Lorentzian and the $\frac{2D}{G}$ ratio decreases significantly, as can be seen in Figure 2.3.

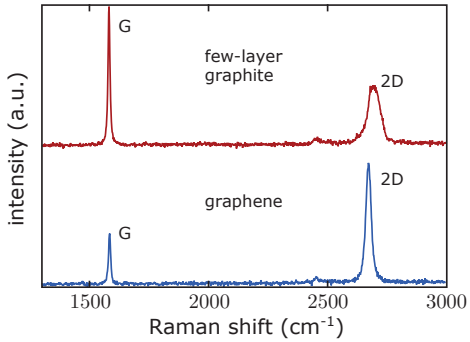

Figure 2.3: **Raman spectroscopy of graphene.** Raman spectrum of graphene (blue) and few-layer graphite (red). Graphene can be identified by the ratio $\frac{2D}{G} > 2$, and the single Lorentzian shape of the 2D peak.

2.1.2 Assembling of van der Waals heterostructures

We now describe the dry-transfer technique that we used throughout the thesis to fabricate van der Waals heterostructures from individually exfoliated flakes. It is based on the transfer technique described in ref. 148 and relies on the subsequent pick-up of individual layers of exfoliated 2D materials and the drop-down of the complete van der Waals heterostructure on the desired substrate. Figure 2.4a shows a schematic of the individual steps that will be described in more detail in the following. In order to perform the pick-ups we use a thin film of polycarbonate (PC) with a thickness of a few µm, which is placed on a thicker polymer for better handling (home-made polydimethylsiloxane – PDMS) attached to a microscope glass slide (see Appendix A.2 for more details and recipes). The glass slide is fastened to a micromanipulator stage allowing for micrometer alignment in all three dimensions. The substrate containing the desired 2D flake is placed on a stage that can additionally be rotated, allowing to control the angle between adjacent layers. Additionally, the substrate stage contains a resistive heater and a temperature controller. For the pick-up, the PC film is brought in contact with the 2D material at a substrate temperature $T \approx 60$ °C. This elevated temperature assures a better adhesion between the PC film and the 2D flake. Once the PC film is in complete contact with the 2D material the transfer pad is lifted by using the micromanipulator stage and the 2D material detaches from the substrate and adheres to the PC film. This technique is repeated until the complete van der Waals heterostructure has been assembled on the PC film. We note that the first pick-up is the most critical step as it can happen that the 2D material flake cannot be detached from the substrate. In subsequent pick-ups the van der Waals forces between adjacent flakes are strong enough to reliably lift the 2D flake from the substrate. Once all flakes have been assembled into a van der Waals heterostructure on the PC film, the complete heterostructure can be deposited on a target substrate. For this, the heterostructure is brought in contact with the desired substrate and the temperature is increased to $T \approx 170$ °C. This melts the PC film, which detaches from the PDMS sheet and sticks to the substrate, where it solidifies after cool-down. The PC can then be removed by chloroform and isopropanol leaving behind the van der Waals heterostructure. It is important to note that apart from the topmost layer, no layer gets in contact with PC or liquid

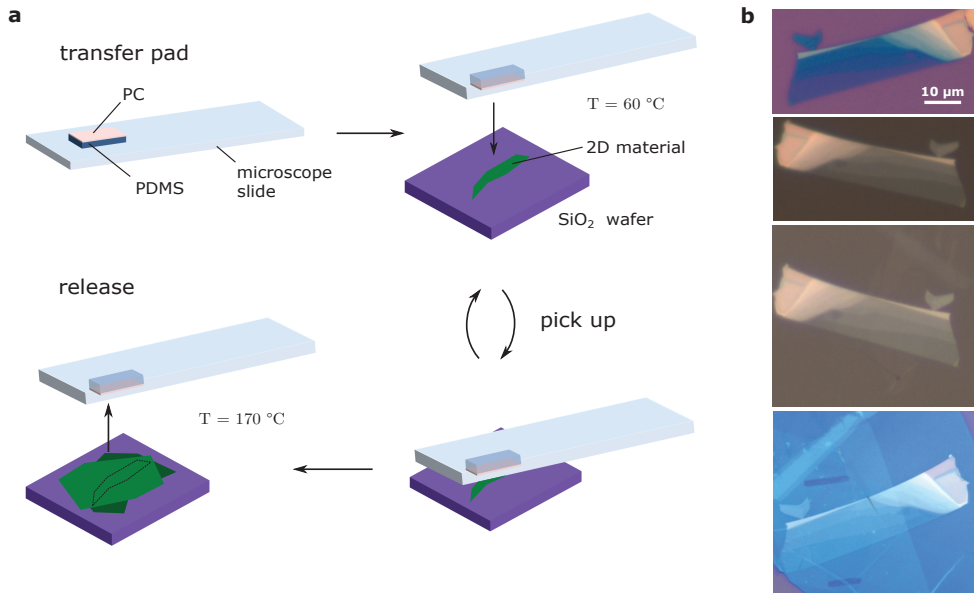

Figure 2.4: **Schematic and optical images of the dry-transfer technique. a**, Schematic of the steps involved in the employed dry-transfer technique for fabricating van der Waals heterostructures. **b**, Optical images of different stages during the fabrication of a boron nitride-graphene-boron nitride-WSe_2 van der Waals heterostructure, where WSe_2 is the topmost layer. The upper image shows the exfoliated WSe_2 flake on a SiO_2 substrate. The next image shows the WSe_2 flake on the PC film after it has been picked up from the substrate. In the subsequent image, the boron nitride (∼5 nm thick) and graphene flake have been picked up, forming a van der Waals heterostructure on the PC film. The boron nitride is not visible on the PC film due to its lack of absorption of visible light. The graphene flake can be seen faintly, ranging over the WSe_2 flake. The final image shows the complete the heterostructure deposited on a SiO_2 substrate. Graphene is encapsulated in between two flakes of boron nitride and cannot be seen in the optical image. On each side of the graphene the boron nitride has been removed by reactive ion etching in preparation for the formation of one-dimensional contacts to graphene.

solvents – hence the terminology 'dry-transfer'. This prevents contamination at interfaces between layers and yields highest quality van der Waals heterostructures. With our transfer setup we can align the different flakes with a precision of up to a few micrometers. Figure 2.4b shows an example of an assembly process with optical microscope images at different stages during the fabrication of a boron nitride–graphene–boron nitride–WSe_2 van der Waals heterostructure.

2.1.3 Definition of electrical contacts

In order to electrostatically dope or perform transport measurements on our devices, we need to fabricate metallic contacts. We employ optical lithography in order to define our contacts. Optical lithography is much faster than electron beam lithography while still achieving a spatial resolution of up to 1 µm, which is sufficient for our purposes. We use the positive photoresist

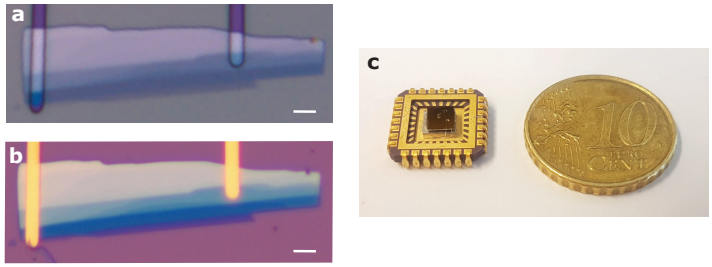

Figure 2.5: **Defining electrical contacts to TMDs. a**, An exfoliated WSe_2 flake covered by photoresist. Contacts have been defined by UV lithography and the sample has been developed for ∼42 s, removing the photoresist from the exposed areas. **b**, The same flake after the evaporation of 2 nm of Ti and 100 nm of Au and subsequent removal of the photoresist. Scale bars in **a** and **b** are 5 µm. **c**, A contacted WSe_2 flake glued and wire bonded to a chip carrier with 28 contacts.

AZ 5214E, which we deposited on our samples by spin-coating at 4000 rpm for 40 s. For the exposure we apply a dose of ∼300 $\frac{\text{mJ}}{\text{cm}^2}$ using the laser writer LW405-B from Microtech. The laser writer allows us to instantly adjust the shapes and sizes of our contacts to the respective device geometries, which is not possible by using for example a shadow mask exposure. We develop the exposed samples for 42 s in a solution of four parts of deionized water and one part of developer AZ 351B, removing the exposed areas of the photoresist (Figure 2.5a). We then metalize our samples with the chosen contact materials. For this we use an evaporator, either the model Univex 350 from Leybold or Lab 18 from Lesker. The standard contact materials that we use for graphene and MoS_2 are 2 nm of Ti and 100 nm of Au. Here, the Ti acts as a sticking layer for Au, which in turn prevents oxidation of the contacts and provides a soft surface for subsequent wire bonding. For WSe_2 we found that Cr yields better p-type contacts and we therefore use 20 nm of Cr and 100 nm of Au to contact WSe_2. After the metalization, we place the samples in acetone for several hours, which dissolves the photoresist and removes the metal thereon, leaving behind only the metal in the areas previously exposed by optical lithography (Figure 2.5b). Finally, we rinse the sample in isopropanol to remove any residues of acetone and blow-dry it. We now cut the substrate into a small rectangle of ∼5×5 mm and glue it into a chip carrier with 28 electrical connections (from Chelsea Technology, Inc.) using electrically conductive silver paste as a glue. Finally, we use a wire bonder (model 7476E from West Bond, Inc.) to connect the electrical connections from the chip carrier to contact pads that we have previously defined on the substrate, with a typical size of 200×200 µm^2. An example of a complete device is shown in Figure 2.5c.

For contacting each layer of a van der Waals heterostructure individually, we also need to be able to define contacts to layers that are completely encapsulated by other materials. This can be done by defining one-dimensional side contacts to graphene, as is described in ref. 17. For this, we need to perform an additional etching step in between the photolithography and metalization. We use reactive ion etching (Plasmalab System 100 from Oxford Instruments) with gas flows of 40 sccm of CHF_3 and 4 sccm of O_2 and a RF power of 60 W. This enables us to etch any of the employed 2D materials. The etching rates are 10–15 $\frac{\text{nm}}{\text{min}}$ for hexagonal boron nitride and 7–10 $\frac{\text{nm}}{\text{min}}$ for SiO_2. TMDs show a much faster etching rate and for the

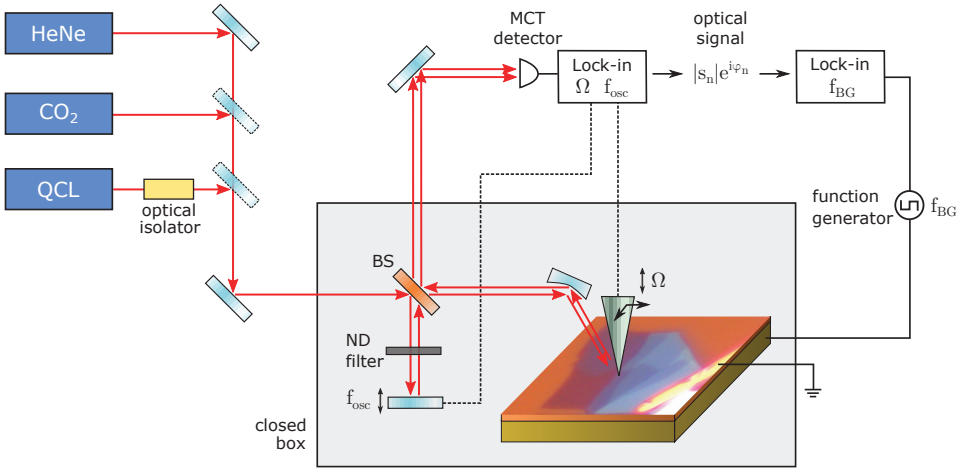

Figure 2.6: **Schematic of the s-SNOM measurement setup.** We employ a CO_2 gas laser (laser lines at 9.3–9.6 and 10.2–10.7 µm) and a quantum cascade laser (MIRcat from Daylight Solutions, Inc. with four modules, emitting at 4.5–5.1, 5.3–5.9, 6.2–6.9, 7.0–7.6 µm, respectively) as our mid-infrared continuous wave illumination sources. The HeNe laser is used for alignment. For the quantum cascade laser we additionally use an optical isolator to avoid the detrimental effect of back reflections into the laser cavity (see section 2.2.3). The gray shaded area represents a closed box to limit environmental fluctuations, which introduce noise into our measurement. The laser beam path is split into two parts by using a ZnSe window as a beam splitter. One path is focused on the oscillating AFM tip with an oscillation frequency $\Omega \approx 285$ kHz by using a parabolic mirror. At the tip apex the light interacts with the sample in the near-field and is collected again by the same parabolic mirror. The other beam path is reflected by a mirror oscillating at $f_{osc} \approx 300$ Hz. We use a neutral density filter in this reference beam with an optical density 0.5 in order to reduce its power and increase the signal to noise ratio. The combined beams are detected by a nitrogen-cooled HgCdTe (MCT) detector (from Kolmar Technologies, Inc.), from which a built-in lock-in amplifier calculates the complex optical signal $s_n = |s_n|e^{i\varphi_n}$ at the n-th harmonic ($n = 1, 2, 3, 4$). Using a home-built electrical setup, we can further apply potentials to any of the contacts of our van der Waals heterostructure. Most importantly, we use a waveform generator to apply a backgate voltage V_{BG} between the Si wafer and the TMD flake with a frequency $f_{BG} \ll f_{osc}$, Ω. We then employ an additional lock-in technique to only extract the optical signal induced by doping the TMD (see section 2.2.4).

thicknesses that we use in our experiments we can assume them to be etched instantaneously. After exposing the edges of graphene (an example is the last image of Figure 2.4b) we can proceed with the metalization as described above.

2.2 Experimental setup

The observation of absorption due to intersubband transitions in TMDs holds many challenges. First, TMD flakes obtained by mechanical exfoliation are very small and an area with one given thickness is typically smaller than the spot size of a mid-infrared laser. This hinders

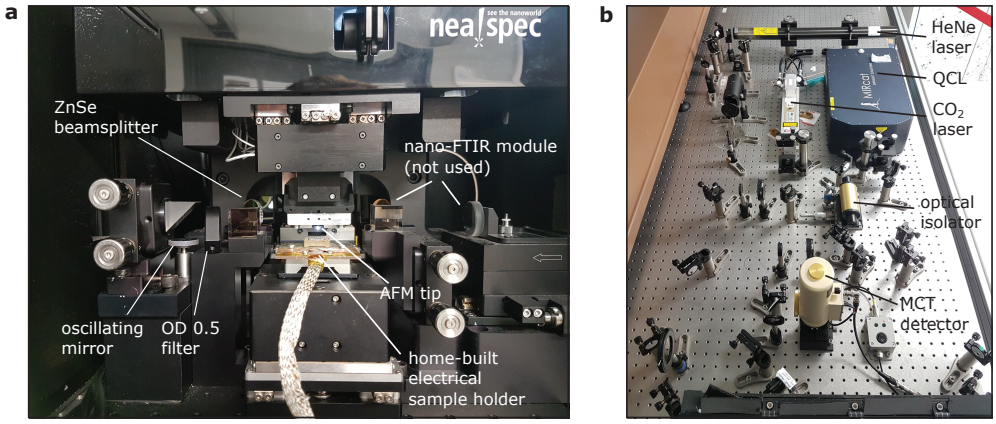

Figure 2.7: **Photos of the s-SNOM measurement setup.** **a**, Photo of the commercially available s-SNOM from neaspec GmbH, as used throughout this thesis. **b**, Photo showing the optical table with the various components used in the experiments.

the implementation of standard absorption measurement techniques, like Fourier-transform infrared spectroscopy. Second, in order to excite intersubband transitions, the electric field of the incoming light needs to have a polarization component in the out-of-plane direction. In III-V semiconductor heterostructures, this is achieved by for example tilting the sample with respect to the k-vector of the incident light[12,149] or by using metallic gratings,[150,151] leading to additional constraints in the sample design. Finally, the expected absorption of a single quantum well is very small. In III-V semiconductors this is overcome by the use of waveguides, in which light passes several times through the same quantum well. Additionally, by using a metal coating, the out-of-plane component of the electric field can be enhanced in close proximity of the quantum well, leading to enhanced absorption. For TMD quantum wells, these approaches result in complicated fabrication and again require large area flakes.

Instead, we therefore use scattering scanning near-field optical microscopy (s-SNOM)[152] to overcome these challenges and to measure intersubband absorption in exfoliated TMD flakes. Our measurement setup is based on a commercially available s-SNOM from neaspec GmbH that we modified with optical and in particular electrical components needed for our experiments. Figure 2.6 shows a sketch of the s-SNOM setup and Figure 2.7 shows a photo of its implementation in the lab. In a s-SNOM a laser beam is focused on a PtIr-coated AFM tip (from NanoWorld), creating a near-field around the tip apex. This near-field interacts with the sample underneath the tip and the back-scattered light is collected and read out in the far-field by a detector. It now carries information about the local optical properties of the sample underneath the tip. This is an established technique to measure the absorption of a sample at the illumination frequency.[153–155] By using the s-SNOM, we can even probe smallest flakes since the light-matter interaction happens in the near-field around the AFM tip. Therefore, the spatial resolution is approximately equal to the tip radius ($\sim$10 nm), far beyond the diffraction limit of light. Crucially, we can also excite intersubband transitions since the near-field around the tip contains out-of-plane polarization components. Finally, we use a home-built electrical sample holder, that allows us to apply voltages to each contacted layer in a van der Waals heterostructure. When we measure the devices on a Si/oxide substrate,

we can use the Si as a backgate and in-situ tune the doping of the TMD flake. Therefore, we can either populate the conduction band or the valence band, and measure the intersubband transitions for electrons and holes without having to change the device.

2.2.1 Working principle of the s-SNOM

The working principle of the s-SNOM is precisely described in refs. 152,156. Here we summarize its main aspects relevant for our experiments.

In order to model the tip-sample interaction, we assume the AFM tip to be a point dipole at the tip apex sphere's center with polarizability

$$\alpha = 4\pi a^3 \frac{\epsilon_t - 1}{\epsilon_t + 2}, \tag{2.1}$$

where ϵ_t is the relative permittivity of the tip at the illumination frequency and a is the tip radius (Figure 2.8a). This dipole introduces a mirror dipole inside the sample with polarizability $\alpha\beta$, where

$$\beta = \frac{\epsilon_s - 1}{\epsilon_s + 1}, \tag{2.2}$$

is the quasi-static reflection coefficient and ϵ_s is the relative permittivity of the sample. The two dipoles now interact with each other, yielding an effective polarizability of the coupled tip-sample system

$$\alpha_{\text{eff}} = \frac{\alpha(1+\beta)}{1 - \alpha\beta/(16\pi(a+z)^3)}, \tag{2.3}$$

where z is the tip-sample distance. Equation 2.3 is key for the understanding of the working principle of the s-SNOM since the scattered field from the tip is proportional to α_{eff}. First, we observe that the scattered signal only depends – apart from the tip parameters and tip-sample distance – on the relative permittivity of the sample. Therefore, the s-SNOM is essentially a tool to locally measure the permittivity of a sample. Second, we note that α, β and α_{eff} are generally complex valued quantities. This motivates the use of interferometric detection as is shown in Figure 2.6. Finally, α_{eff} depends non-linearly on z. This is crucial for the suppression of the large background signal. The background arises since the majority of the incoming light does not interact with the sample but is directly reflected from the metalized AFM tip. To eliminate this background, it has been suggested to filter the scattered signal at the tapping amplitude Ω. Since the focal spot of the incoming light is much larger than the tapping amplitude – which is on the order of the tip radius a – the background remains constant, whereas the scattered near-field signal depends strongly on z. However, this is generally not sufficient to suppress the background. More efficiently, the signal can be demodulated at higher harmonics n of Ω, which occur due to the non-linear dependence of α_{eff} on z. However, when using this modulation technique it can be shown that background still influences the detector signal. For a complete elimination of the background, a more sophisticated technique

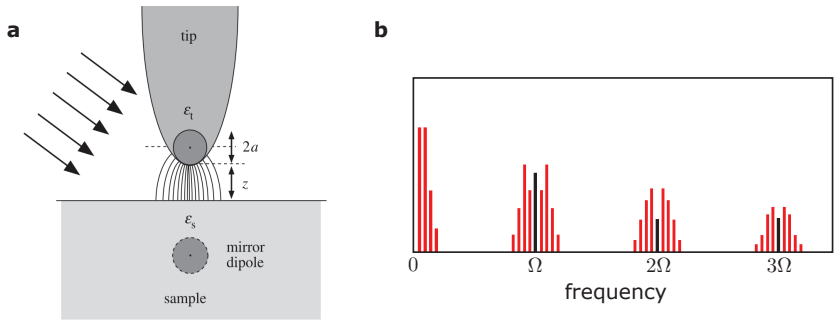

Figure 2.8: **Point dipole approximation of the AFM tip and generation of sidebands. a**, Schematic of the AFM tip and its approximation as a point dipole source. Solid lines around the tip apex represent the field lines induced by the tip under illumination. The relevant parameters of the tip are its relative permittivity ϵ_t and apex radius a. The point dipole is assumed to be placed in the center of the sphere at the tip apex. A mirror dipole is induced in the sample with relative permittivity ϵ_s. Adapted from ref. 156. **b**, Generation of sidebands in the pseudo-heterodyne detection mechanism. Higher harmonics (black) of the tip oscillation frequency Ω occur due to the non-linear dependence of the scattered signal on the tip-sample distance z. The reference arm mirror is additionally modulated with f_{osc}, which leads to the generation of sidebands around the harmonics. The optical signal is read out from these sidebands. In our experiment $\Omega \approx 285$ kHz and $f_{\text{osc}} \approx 300$ Hz. Adapted from ref. 152.

has to be used. It has been shown that a heterodyne interference method is capable of completely eliminating the background.[156] In this work, the reference beam was frequency shifted by 80 MHz with an acousto-optic modulator. A more practical approach that can be extended to a broader frequency range including mid-infrared and THz frequencies is the so-called pseudo-heterodyne interference method.[152] In this method, a phase shift is introduced into the reference beam by a sinusoidal oscillation of the reference arm mirror. This oscillation introduces sidebands in the detector signal around the higher harmonics $n\Omega$ (Figure 2.8b). The signal is now extracted from these sidebands, avoiding any interference from background. In our s-SNOM we use this pseudo-heterodyne method and the detected complex optical signal is then given as $s_n = |s_n|e^{i\varphi_n}$.

2.2.2 Quantitative recovery of the local permittivity

The point-dipole model discussed in the previous section is sufficient to explain the qualitative features of the s-SNOM. However, it has been shown that it fails to quantitatively reproduce the measured optical signals. Instead, the AFM tip has to be considered as an elongated dipole with a length equivalent to the tip length. Using this more complex finite-dipole model, it has been shown that the complex permittivity of an unknown bulk material can be accurately obtained by measuring its optical signal and normalizing it to the optical signal obtained on a material with known permittivity.[155,157] The devices measured in our experiments are more complex, however, as they consist of a thin TMD flake place on an oxide, which we assume to be infinitely thick (Figure 2.9). This is a good assumption as the oxide is thick enough for the Si substrate not to significantly influence the optical signal. While the recovery of the complex

permittivity is generally not possible for an arbitrary sample geometry, a theoretical model and experimental demonstration has been reported for a thin film on top of a bulk substrate,[158] which is the precise sample geometry of our experiments. We used this model to obtain the complex permittivity of WSe_2 and therefore its absorption. In the following section we summarize its main aspects and confirm its validity for our sample geometry.

In the finite-dipole model, the effective polarizability of the coupled tip-sample system (see section 2.2.1) is given as

$$\alpha_{\text{eff}} = C\left(2 + \frac{f_0(H)\,\beta}{1 - f(H)\,\beta}\right), \tag{2.4}$$

where H is the height of the tip above the sample surface, C is a constant and $f_0(H)$ and $f(H)$ are height-dependent functions, whose values are defined by the tip properties (their expressions are given in Appendix A.3). For commercially available AFM tips, these tip properties do not vary significantly. H is furthermore time-dependent, varying sinusoidally with the AFM tip oscillation frequency Ω and amplitude A.

The scattering coefficient $\sigma = E_s/E_i$, relating the field scattered from the tip E_s to the field incident upon it E_i, can be written as

$$\sigma = \alpha_{\text{eff}}(1 + r_s)^2, \tag{2.5}$$

where the reflection coefficient r_s accounts for light scattered by the sample substrate before interacting with the AFM tip. However, the measured scattering coefficient in experiments is dominated by background scattering, which is why the optical signal is evaluated at higher harmonics of the tip oscillation frequency $n\Omega$. Mathematically, this can be described by the complex Fourier transform of $\sigma(H)$. The n-th Fourier coefficient

$$\begin{aligned}\sigma_n(\beta) &= \hat{F}_n[\sigma(\beta, H(t))] \\ &= \int \sigma(\beta, H(t)) \exp(in\Omega t)\mathrm{d}t\end{aligned} \tag{2.6}$$

is proportional to the n-th order demodulated detector signal. The inversion of Equation 2.6 for an unknown permittivity of the sample – and therefore unknown β – represents a non-trivial mathematical problem. In order to solve this problem numerically, α_{eff} needs to be Taylor expanded in powers of $f\beta$

$$\alpha_{\text{eff}} = \sum_{j=0}^{\infty} \alpha_j (f\beta)^j, \tag{2.7}$$

with the expansion coefficients α_j, which are independent of the sample's relative permittivity. Now, the demodulated detector signal can be written as a power series

$$\sigma_n = (1 + r_s)^2 \sum_{j=1}^{\infty} \hat{F}_n[\alpha_j f^j]\beta^j. \tag{2.8}$$

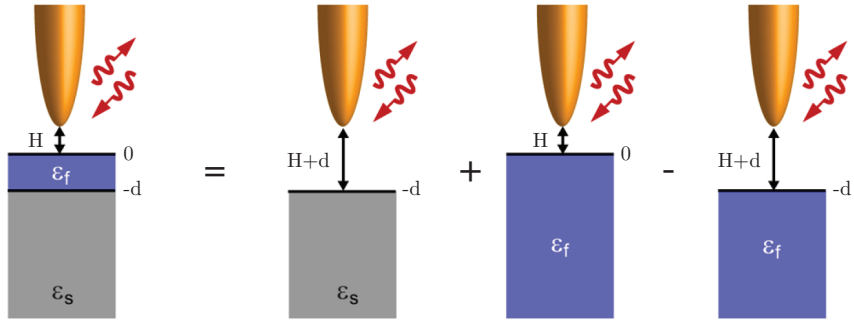

Figure 2.9: **Schematic illustration of the quantitative permittivity recovery.** Illustration of our typical sample geometry consisting of a thin film with relative permittivity ϵ_f and thickness d on top of a substrate with relative permittivity ϵ_s. The interaction of the tip with this particular sample geometry can be split into a sum of three parts, as illustrated. The corresponding effective polarizability of the tip-sample system using this expansion is given in Equation 2.10. Adapted from ref. 158.

Truncated at a particular order J (for our analyses we typically use $J = 21$), this is a polynomial equation that can be solved using standard numerical methods. Finally, in order to get rid of influences of the setup, the demodulated detector signal σ_n has to be normalized by a reference measurement, $\sigma_{n,\text{ref}}$, on a substrate with well known properties and effective polarizability $\alpha_{\text{eff,ref}}$. This yields the complex normalized near-field contrast

$$\eta_n = \frac{\sigma_n}{\sigma_{n,\text{ref}}} = \sum_{j=1}^{J} \frac{\hat{F}_n[\alpha_j f^j]}{\hat{F}_n[\alpha_{\text{eff,ref}}]} \beta^j, \tag{2.9}$$

which can be directly measured in experiments. Equation 2.9 is therefore the central equation relating the measured optical signals to a theoretical equation that can be inverted by standard numerical methods.

Until now, however, we have assumed the sample to have one effective relative permittivity and did not take into account the special geometry of our samples, being a thin film on top of a bulk substrate. We take this geometry into account by splitting the tip-sample interaction into three terms, as is illustrated in Figure 2.9. The thin film with permittivity ϵ_f is assumed to be at $z = 0$ with a thickness of d. The substrate with permittivity ϵ_s starts at -d and extends up to minus infinity. The effective polarizability of this expansion can now be written as

$$\alpha_{\text{eff}} = C \left(2 + \frac{f_0 (H+d) \beta_s}{1 - f (H+d) \beta_s} + \frac{f_0 (H) \beta_f}{1 - f (H) \beta_f} - \frac{f_0 (H+d) \beta_f}{1 - f (H+d) \beta_f} \right), \tag{2.10}$$

where β_s and β_f are the quasi-static reflection coefficients of the substrate and thin film, respectively. Each of these terms can be extended into a power series of β_f by using the relationship $\frac{1}{1-x} = \sum_n x^n$ for $|x| < 1$. This leads to the constraint $|f\beta_f| < 1$, which is fulfilled for weak resonances as is the case in our experiments. After the expansion of α_{eff} into

a power series we can use Equation 2.9 to directly calculate ϵ_f from the measured normalized near-field contrast η_n.

Verification of the permittivity recovery

We now verify the above model by comparing the predicted near-field contrast with optical values obtained from our experiment. For this, we first simulate the expected optical signal of a WSe_2 flake with varying thicknesses on top of an infinitely thick HfO_2 substrate. We employ simulation parameters that we typically use in our experiments, namely an AFM tip oscillation amplitude $A = 75$ nm and tip frequency $\Omega = 250$ kHz. We assume the permittivity of the underlying HfO_2 to be $\epsilon_{HfO_2} \approx 2.8$, which corresponds to an illumination wavelength of 7.5 µm.[142] For the permittivity of WSe_2 we have to take into account its anisotropy, with an in-plane component $\epsilon_{WSe_2,xy} = 12.7$ and an out-of-plane component $\epsilon_{WSe_2,z} = 4.2$.[159] Since we probe both components by using the s-SNOM, we use an effective permittivity $\epsilon_{WSe_2} = \sqrt{\epsilon_{WSe_2,xy} \times \epsilon_{WSe_2,z}} = 7.3$ for our simulations. The simulated absolute value of the optical signal $|s_n|$ normalized to the signal on HfO_2 is shown in Figure 2.10a for demodulation orders $n = 2, 3, 4$. We observe a monotonic, sublinear increase with the WSe_2 thickness for all demodulation orders. This effect can intuitively be understood since $\epsilon_{WSe_2} > \epsilon_{HfO_2}$. With increasing WSe_2 thickness the AFM tip is probing a larger fraction of WSe_2, leading to a stronger near-field contrast. In order to quantitatively validate this model, we performed s-SNOM measurements on a WSe_2 flake with terraces of different thicknesses, exfoliated on top of a HfO_2 substrate. We found very good agreement between the simulated and measured optical signals (Figure 2.10a) for all WSe_2 thicknesses that we use in our experiments. This is a first confirmation of the validity of the thin-film inversion model for our samples.

Next, we model how absorption in WSe_2 and therefore a change in $\mathrm{Im}(\epsilon_{WSe_2})$ is reflected in the measured s-SNOM signal. To do so, we model a 4-layer thick WSe_2 crystal on top of HfO_2 at an illumination wavelength of 7.5 µm. The change in phase of the optical signal $\Delta\varphi_n$ for increasing $\mathrm{Im}(\epsilon_{WSe_2})$ is plotted in Figure 2.10b. We observe a linear increase of $\Delta\varphi_n$ for all demodulation orders. $|s_n|$ does not depend significantly on $\mathrm{Im}(\epsilon_{WSe_2})$. Therefore, for a given layer thickness, $\Delta\varphi_n$ provides a direct measure of the relative absorption of WSe_2.

Finally, we verify that the reconstruction of $\mathrm{Im}(\epsilon_{WSe_2})$ from the optical signal using the thin-film inversion model is independent of any measurement parameters. To do so we measured a WSe_2 flake exfoliated on a Si/SiO_2 substrate at an illumination wavelength of 10.6 µm. We took several measurements for different tapping amplitudes and recorded the different demodulation orders $n = 2, 3, 4$ (Figure 2.10c). First, we observe a distinctively larger $\Delta\varphi_n$ for higher demodulation orders n. Second, we observe a slight decrease of $\Delta\varphi_n$ with tapping amplitude, especially for higher n. These features should not appear in the obtained $\mathrm{Im}(\epsilon_{WSe_2})$, as they do not represent any physical property of the probed WSe_2 flake. Indeed, after the inversion using the thin-film model (Figure 2.10d) we see that $\mathrm{Im}(\epsilon_{WSe_2})$ shows no more dependence on the used tapping amplitude. We also observe that the difference between different demodulation orders reduces drastically, although it does not vanish completely. These findings further confirm that the thin-film inversion model is well-suited for our sample geometries.

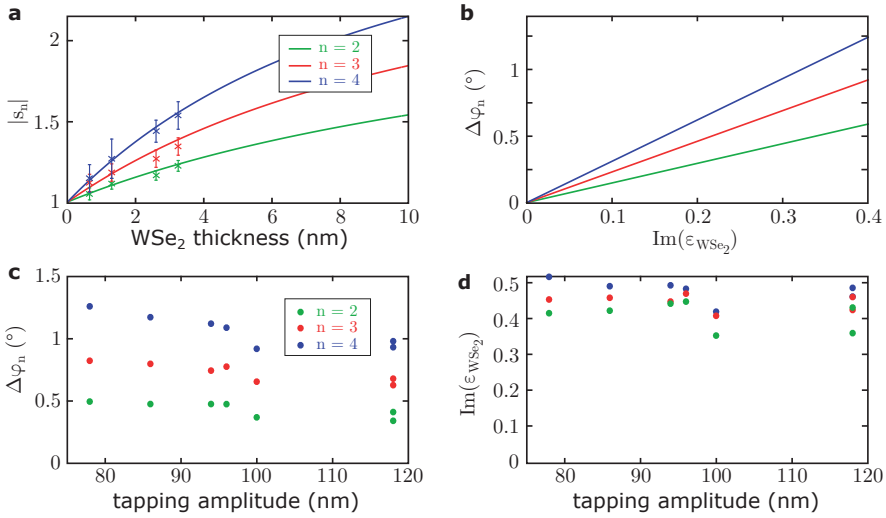

Figure 2.10: **Verification of the permittivity recovery. a**, Simulation of the absolute value of the optical signal $|s_n|$ for different thicknesses of a WSe_2 flake ontop of a HfO_2 substrate. Shown are the demodulation orders $n = 2$, 3, 4. The simulations were performed using the thin-film inversion model discussed in section 2.2.2 with a tip frequency $\Omega = 250$ kHz and a tip oscillation amplitude $A = 75$ nm, which are typical values used in our experiments. The used relative permittivities are $\epsilon_{HfO_2} = 2.8$ and $\epsilon_{WSe_2} = 7.3$. Crosses indicate experimental values, obtained at an illumination wavelength of 7.5 µm. Error bars indicate the root mean square in the analyzed areas of the flake. **b**, Simulated change in the phase of the optical signal $\Delta\varphi_n$ as a function of $\mathrm{Im}(\epsilon_{WSe_2})$ for a 4-layer thick WSe_2 flake on top of HfO_2. **c**, Measured $\Delta\varphi_n$ on a 5-layer thick WSe_2 flake on top of a SiO_2 substrate at an illumination wavelength of 10.6 µm for different tapping amplitudes and demodulation orders. **d**, The obtained $\mathrm{Im}(\epsilon_{WSe_2})$ from the data in **c** using the thin-film inversion model as described in section 2.2.2.

Calculation of the absorption

In classical far-field absorption measurements of intersubband transitions, the absorption is typically given as the 2D sheet absorption α_{2D}.[12,149] In order to obtain α_{2D} from the relative permittivity ϵ we first calculate the complex refractive index

$$\widetilde{N} = \sqrt{\epsilon}. \tag{2.11}$$

Its imaginary part $\mathrm{Im}(\widetilde{N}) = \kappa$ is related to the attenuation coefficient μ as

$$\mu = 4\pi\kappa/\lambda, \tag{2.12}$$

with the illumination wavelength λ. Using the Beer-Lambert law we can then approximate α_{2D} for small absorption within a crystal of thickness d as

$$\alpha_{2D} = 1 - \mathrm{e}^{-\mu d} \approx \mu d. \tag{2.13}$$

2.2.3 Main noise sources

The measurement of intersubband transitions in TMDs requires a high signal to noise ratio, since the absorption of a single quantum well is very small. Here, we identify the main noise sources of our setup and present solutions on how to suppress this noise.

Ambient instabilities

The s-SNOM does not only have to be isolated from vibrations (as is the case for every AFM) but it is also sensible to instabilities in its surrounding atmosphere. These instabilities can for example be caused by air flows due to the air conditioning system or the chillers of the lasers. They mainly cause fluctuations in the relative path lengths of the two interferometer arms, which lead to fluctuations in the phase of the optical signal φ_n. We avoid these instabilities by enclosing the SNOM system within a specifically designed box. If such a box is not available any other provisional enclosement also helps to drastically reduce the noise. Figure 2.11a shows the use of commercial aluminium foil to achieve this. Figure 2.11b shows a time trace of the measured phase of the optical signal φ_3 with and without the enclosement of aluminium foil. A significant decrease in fluctuations is readily visible by using this primitive enclosure.

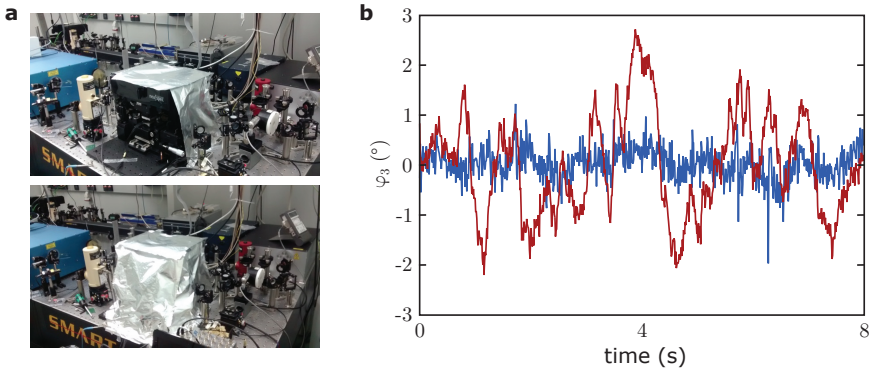

Figure 2.11: **Provisional enclosement of the s-SNOM. a**, Enclosement of the s-SNOM in commercial aluminium foil to reduce the detrimental impact of ambient instabilities. **b**, Time traces of the phase of the optical signal φ_3 with (blue) and without (red) the aluminium foil enclosement. Measurements were taken with a CO_2 laser on a few-layer WSe_2 flake placed on a Si/SiO_2 substrate. The integration time per pixel was 20 ms.

Back reflections into the laser cavity

A major problem arose when we used the quantum cascade laser as an illumination source. The optical signal seemed to have two or more stable values, in between which it jumped randomly while introducing significant noise at the same time. Figure 2.12a shows a time trace of these fluctuations. We concluded that they were caused by back reflections of the laser beam into the optical cavity of the quantum cascade laser. It has been reported that quantum cascade

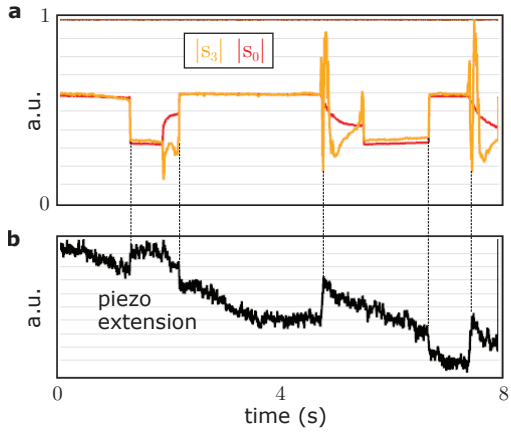

Figure 2.12: **Fluctuations caused by back reflections into the laser cavity. a**, Time trace of the optical signals $|s_3|$ (yellow) and $|s_0|$ (red). The time trace was measured using the quantum cascade laser operating at 7.55 µm on the Au contact of one of our samples. The laser output cw power was 80 mW, which was reduced to 20 mW by two cross-polarized polarizers before interacting with the sample. The fluctuations are caused by back reflections into the laser cavity and can be overcome by using an optical isolator. **b**, Simultaneously measured time trace of the piezo extension of the sample stage in z-direction. Jumps in the signal are caused by sudden thermal expansion of the Au when the incoming light intensity fluctuates.

lasers can be extremely sensitive to back reflections, causing a modulation of all relevant lasing parameters at re-injected powers as low as 10^{-8}–10^{-6} of the emitted power.[160] We could even observe the fluctuations when we blocked the reference arm, indicating that back reflections from the light focused on the AFM tip alone were enough to corrupt the laser output. In the time trace shown in Figure 2.12 we placed the AFM tip on one of the Au contact pads. The fluctuations were then not only limited to the optical signal but could also be observed in the mechanical signal (Figure 2.12b). More precisely, this signal is a measure for the piezo extension of the sample stage in the z-direction. We attribute this observation to rapid thermal extension of the Au contact pads, an effect that is used to spectrally measure infrared absorption with nanoscale resolution in a technique called atomic force microscope infrared-spectroscopy.[161] For our experiments it is therefore likely that the power that was focused on the AFM tip was fluctuating, which could for example be caused by mode-hopping inside the laser cavity. This also explains the observed bistabilities.

In order to overcome these fluctuations we made use of an optical isolator. Here, time-reversal symmetry is broken by the magnetic field inside a Faraday rotator, which rotates the incoming linearly-polarized laser light by 45°. Together with two polarizers – before and after the Faraday rotator – the backscattered light can be suppressed efficiently. By adjusting the second polarizer after the Faraday rotator for each wavelength we were able to completely eliminate the fluctuations shown in Figure 2.12.

2.2.4 Charge carrier density modulation

After eliminating the most detrimental noise sources, we analyzed the spectrum of the remaining noise. For this, we took a time trace of the optical signal on a MoS_2 flake placed on a Si/SiO_2 substrate at an illumination wavelength of 6.2 µm. We Fourier transformed this time trace to identify the dominant frequencies contributing to the measured noise (Figure 2.13). We find large noise contributions at very low frequencies (<0.2 Hz), which we attribute to drifts of the interferometer arm or within the laser cavity. For all higher frequencies, the noise remains constant.

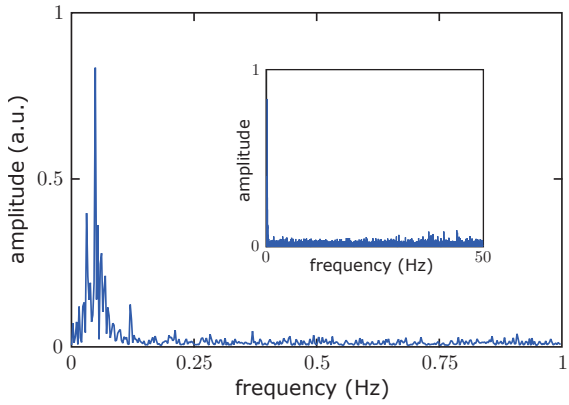

Figure 2.13: **Noise components in typical s-SNOM measurements.** Single-sided amplitude spectrum of the Fourier transform of a time trace taken on a few-layer MoS_2 flake placed on a Si/SiO_2 substrate. The inset shows the same data over a larger frequency range. The time trace was taken over 6.5 minutes at an illumination wavelength of 6.2 µm, illumination power of 12 mW and a sampling interval of 10 ms.

In order to suppress the low-frequency noise components we made use of the fact that we need to populate the highest valence band or lowest conduction band with holes or electrons, respectively, in order to observe intersubband transitions. The optical signal when the TMD flake is charge neutral does not exhibit intersubband absorption and can be used as a reference signal. We can therefore isolate absorption due to intersubband transitions by modulating the charge carrier density by applying an AC backgate voltage between the Si wafer and the TMD flake. A frequency of a few Hz is sufficient to effectively suppress the main noise contributions at low frequencies and should significantly increase the signal to noise ratio.

We considered several possibilities on how to implement the backgate modulation into our s-SNOM measurements. s-SNOM measurements are saved as digital images, where the sampling time per pixel can be adjusted. The challenge lies in synchronizing the AC backgate voltage V_{BG} with the pixels of the s-SNOM images, so that after a measurement each pixel can be assigned to a particular V_{BG}.

Ideally, we would change V_{BG} for each pixel and reconstruct two images out of one scan – one for a doped TMD flake and another one for an undoped flake. The s-SNOM also has a pixel counter that outputs a TTL signal that can be used for counting the pixels. Unfortunately, however, we found this TTL signal to be out-of-phase with the sampling interval of the s-

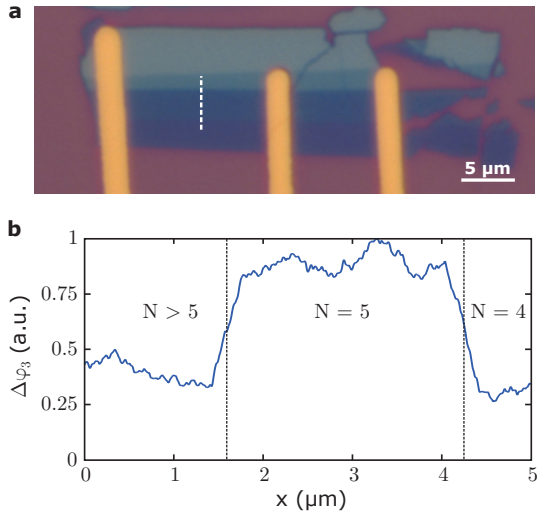

Figure 2.14: **Observation of intersubband transitions by using a lock-in amplifier. a**, Optical image microscope image (100x magnification) of the measured WSe_2 flake, exfoliated on a Si/SiO_2 substrate. **b**, Signal obtained by using the lock-in amplifier, corresponding to the change in optical phase of the third harmonic with doping, $\Delta\varphi_3$. The shown data is a single line scan along the dashed line in **a**. We modulated V_{BG} with a sine wave with a frequency of 90 Hz. The integration time per pixel and the integration time of the lock-in amplifier were set to the same value of 100 ms. The line scan consists of 1250 pixels, meaning that it has been acquired in $\sim$2 minutes. The absorption due to intersubband transitions manifests itself in an increased signal in the area of the WSe_2 flake with $N = 5$. In order to highlight this increased signal, we smoothed the obtained data by using a moving average filter over 101 pixels. This reduces the spatial resolution and the observed sharpness of the step at interfaces between adjacent layers does not correspond to the intrinsic resolution of the s-SNOM. Compare also to Figure 2.15c and d for similar measurements acquired without modulation of V_{BG} and measurements with a 'manual' modulation technique, respectively.

SNOM and we therefore cannot use it to trigger V_{BG} since one pixel would contain a mixture of several V_{BG}. Additionally, we occasionally found a pixel to be skipped, which renders the s-SNOM scan useless from that moment on.

Another possibility that we explored is to use a lock-in amplifier. For this, we used the analog output of the s-SNOM system as an input for the lock-in amplifier. We modulated V_{BG} as a sine wave with a frequency of 90 Hz by using a function generator, which served as the reference signal for the lock-in amplifier. We then used the output signal from the lock-in amplifier as an input to the s-SNOM, where the analog signal was converted into a digital signal by assigning an averaged value from the lock-in to each pixel. By using this method we could indeed observe absorption due to intersubband transitions, as is shown in Figure 2.14. The signal to noise ratio is significantly higher than in DC measurements and scans can be acquired much faster. The disadvantage is that we would need one lock-in amplifier to monitor one signal, for example the amplitude or phase of one given harmonic n. Additionally, the only 'clean' recorded optical signal is the one from the lock-in amplifier. In all other optical signals, V_{BG} is varied several times within one pixel. For the quantitative calculation of the

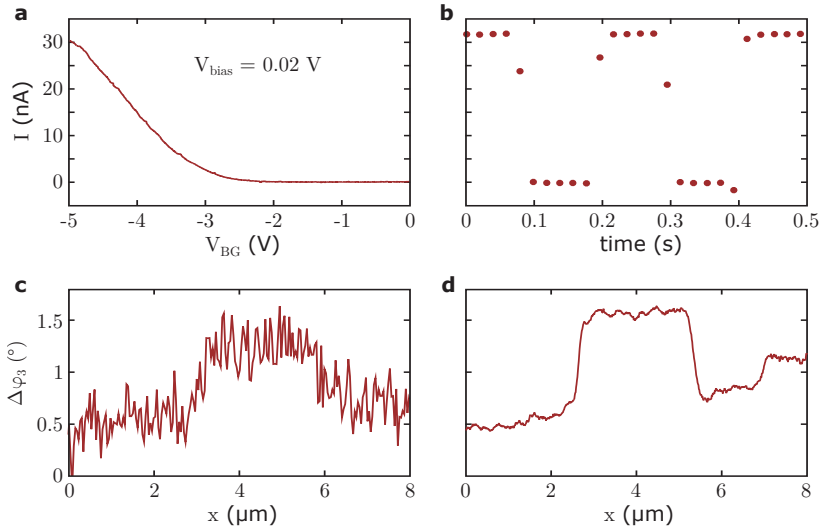

Figure 2.15: **Employed backgate modulation technique. a**, p-type FET behavior of a few-layer WSe_2 flake placed on a Si/HfO_2 substrate. The intrinsic hole doping of WSe_2 manifests itself in a strong p-type field effect. **b**, Modulation of V_{BG} between 0 and -5 V with a square wave using a frequency of 4.9 Hz. The measurement was performed on the same flake as the one in **a**. The integration time per pixel was ∼20 ms. Pixels during which the flake was partially doped and partially undoped are disregarded from subsequent analysis. **c**, Difference in the phase of the optical signal $\Delta\varphi_3$ between two DC line scans with V_{BG} = 50 V and V_{BG} = -50 V, respectively. The measurement was performed on a terraced MoS_2 flake exfoliated on a Si/SiO_2 substrate at an illumination wavelength of 10.6 μm. **d**, Same measurement as in **c** but using the modulation technique as described in the text. The total time needed for acquiring the measurements in **c** and **d** is roughly equal with ∼5–10 minutes, depending on the chosen scanning parameters.

permittivity (section 2.2.2), however, we do not only need the difference between doped and undoped TMD but we need both optical signals, where the optical signal of the undoped TMD serves as a reference value. Due to these practical difficulties it is not ideal to use a lock-in amplifier for our experiments.

Instead, we decided to use a 'manual' lock-in technique. Here, we exploited the FET behavior of the TMD flakes to monitor when the flake was doped or charge neutral. Typically, WSe_2 is intrinsically p-doped and therefore shows a strong p-type field effect (Figure 2.15a) but we also observe ambipolar behavior. MoS_2, on the other hand, is intrinsically n-doped and only a n-type field effect can be observed. We applied a small bias voltage $V_{bias} < 0.1$ V between a source and drain contact on the TMD flake and modulated V_{BG} as a square wave by using a function generator. We converted the resulting source-drain current into a voltage by using a transimpendence amplifier with variable sensitivity and a bandwidth of up to 200 MHz (DHPCA-100 from Femto) and used this voltage as an input signal to the s-SNOM. In this way we were able to monitor the conductance of the TMD flake and hence its doping for each pixel (Figure 2.15b). We chose the frequency of V_{BG} in such a way that we obtained 4–5 pixels during which the TMD flake was doped and charge neutral,

respectively. We disregarded pixels during which the flake was partially doped and partially charge neutral. By averaging and interpolating each of the resulting pixel clusters we then obtained two scans out of one measurement, one for the doped and one for the charge neutral TMD flake. During this process we lose spatial resolution, for which we compensated by oversampling, i.e. scanning in smaller steps than the spatial resolution of the s-SNOM. The improvement using this modulation technique is illustrated in Figures 2.15c and d. Here, we repeatedly scanned over the same line of a terraced MoS_2 flake with areas of different N, exfoliated on a Si/SiO_2 substrate. Figure 2.15c shows the difference in the optical phase $\Delta\varphi_3$ between two DC scans with V_{BG} = 50 V and V_{BG} = -50 V, respectively. In Figure 2.15d, we scanned over the same areas but employed the above described modulation technique of V_{BG}. First, we observe that the main features of the experiment are visible in both, the DC and AC measurements. Second, it becomes evident that the modulation technique significantly enhances the signal-to-noise ratio indicating that we are able to successfully suppress the low-frequency noise components.

2.2.5 Tip-induced doping

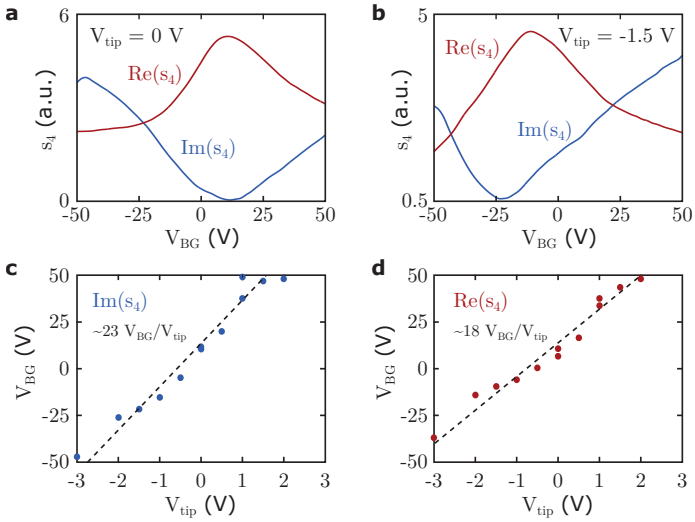

Figure 2.16: **Quantification of the tip-induced doping. a, b,** Measured optical signal s_4 corresponding to the local complex conductivity of graphene underneath the AFM tip for V_{tip} = 0 V (**a**) and V_{tip} = -1.5 V (**b**). Measurements were performed on a graphene flake, exfoliated on a Si/SiO_2 substrate at an illumination wavelength of 10.6 µm. **c, d** Minimum of $\mathrm{Im}(s_4)$ (**c**) and maximum of $\mathrm{Re}(s_4)$ (**d**) obtained from measurements as in **a** and **b** for different V_{tip}. The dashed lines are linear fits to the data, whose slopes indicate the needed V_{BG} in order to compensate for the effect of V_{tip}.

We can also use the metallic AFM tip to locally dope our samples[162,163] and enhance the doping of our TMD flakes. This enhances the intersubband absorption and helps us to reach ambipolar absorption behavior. For this, we apply a constant potential V_{tip} to the TMD crystal, which locally induces charge carriers (holes for $V_{tip} > 0$ and electrons for $V_{tip} <$

0) due to the coupling with the grounded, metallic AFM tip. We can furthermore apply a backgate voltage V_{BG}, globally controlling the charge carrier density. In order to estimate the magnitude of the tip-induced doping we performed s-SNOM measurements on a separate graphene flake exfoliated on a Si/SiO_2 substrate and made use of the fact that the optical signal s_4 measures the local complex permittivity underneath the tip. At the graphene charge neutrality point the imaginary part of the permittivity and therefore $\mathrm{Im}(s_4)$ shows a minimum, while $\mathrm{Re}(s_4)$ shows a maximum.[49] We now vary V_{BG} and record s_4 for different potentials V_{tip} applied to the graphene flake. For $V_{tip} = 0$ (Figure 2.16a) we see that the charge neutrality point of graphene is at about $V_{BG} = 10$ V, indicating that the graphene flake is slightly hole doped. For $V_{tip} = -1.5$ V the local charge neutrality point of graphene shifts to negative V_{BG}, indicating that the graphene flake becomes locally electron doped due to the interaction with the AFM tip (Figure 2.16b). We repeated this measurement for various V_{tip} and find that V_{tip} influences the local charge carrier density of graphene as $V_{tip} \approx -20 V_{BG}$ (Figures 2.16c and d). This means that by applying a constant V_{tip}, we can effectively shift the range of doping that is induced electrostatically by V_{BG} towards the p- or n-doped regime, depending on what we require for our experiments.

3 Observation of intersubband transitions

In this chapter we demonstrate absorption due to intersubband transitions in WSe_2 and MoS_2. We first perform spatially resolved measurements by exploiting the nanometer scale resolution of the s-SNOM. We then spectrally resolve the intersubband transitions and compare the measured absorption line shape to the previously developed theory. Finally, we study the charge carrier density dependence of intersubband absorption and demonstrate ambipolar intersubband absorption due to electrons and holes within the same flake.

3.1 Spatially resolved measurements

We first exploit the unprecedented lateral resolution of ∼20 nm of the s-SNOM to obtain spatial absorption maps of our TMD flakes. For this, we scan the AFM tip over our samples and simultaneously record both, the height of the flake measured by AFM and the detected optical signals. In a first set of measurements we use a fixed illumination photon energy of $E_{\mathrm{ph}} = 117$ meV (corresponding to a wavelength of 10.6 µm), since we obtain the highest signal to noise ratio for this CO_2 laser line. Figure 3.1a shows the obtained AFM image of a WSe_2 flake on top of a Si/SiO_2 substrate. Figure 3.1b shows the corresponding difference in the phase of the optical signal $\Delta\varphi_3$ between two scans with $V_{\mathrm{BG}} = 0$ V and $V_{\mathrm{BG}} =$ -50 V, taken on the same area of the flake. As we discussed in section 2.2.2, $\Delta\varphi_3$ is directly proportional to the absorption of the TMD flake. Figure 3.1b therefore shows the absorption induced by p-doping the WSe_2 flake ($V_{\mathrm{BG}} =$ -50 V), where charge-neutral WSe_2 ($V_{\mathrm{BG}} = 0$ V) serves as a reference. We observe enhanced absorption in one particular thickness of the WSe_2 flake, which corresponds to $N = 5$.

We observe the same behavior on several WSe_2 flakes. Figure 3.1c shows a different WSe_2 flake exfoliated and contacted on a Si/SiO_2 substrate and Figure 3.1d shows a spatial map of $\Delta\varphi_3$, acquired in the area indicated by dashed lines. We observe the same quantitative feature as in the previous scans, with enhanced absorption in the area with $N = 5$. In contrast to the previous measurement, however, this spatial map was acquired in one scan by modulating V_{BG} between 0 and -50 V with a frequency of 4.9 Hz and using the modulation technique as described in section 2.2.4.

We also performed the same measurements on a MoS_2 flake exfoliated on a Si/SiO_2 substrate. Figures 3.1d and e show the AFM image and the measured $\Delta\varphi_4$, acquired by taking the difference between two scans with $V_{\mathrm{BG}} =$ -50 V and $V_{\mathrm{BG}} = +50$ V, respectively. Here, $V_{\mathrm{BG}} =$ -50 V depletes the strongly intrinsically n-doped MoS_2 flake, while $V_{\mathrm{BG}} = +50$ V increases its n-doping. Again, we observe enhanced absorption in the area with $N = 5$. In contrast to the previous measurements, however, this enhanced absorption is due to the electrostatically induced electrons in MoS_2.

We now compare the observed enhanced absorption to the intersubband transition energies obtained by DFT calculations (Figure 1.9). We find that the calculated transition energies for both, holes in WSe_2 and electrons in MoS_2 are predicted to occur close to the used illumination energy $E_{\mathrm{ph}} = 117$ meV. These overview scans are therefore a first indication that we observe intersubband transitions in TMDs. In order to corroborate this interpretation, we now aim to observe enhanced absorption at a different N when varying E_{ph}. However, this is difficult on a SiO_2 substrate since its strong phonon resonance for higher E_{ph} corrupts the detected optical signal (see section 3.2.3 below). We therefore repeat the same measurements on a HfO_2 substrate, whose phonon resonances lie at much lower energies, outside of our laser range.[142]

Figure 3.2a shows the optical image of an exfoliated WSe_2 flake on a HfO_2 substrate and Figure 3.2b shows the absolute value of the optical signal $|s_3|$ obtained in the area of 13x10 µm^2 indicated by the dashed lines. We can clearly distinguish different layer thicknesses in the optical signal due to the change in dielectric environment probed by the AFM tip. A

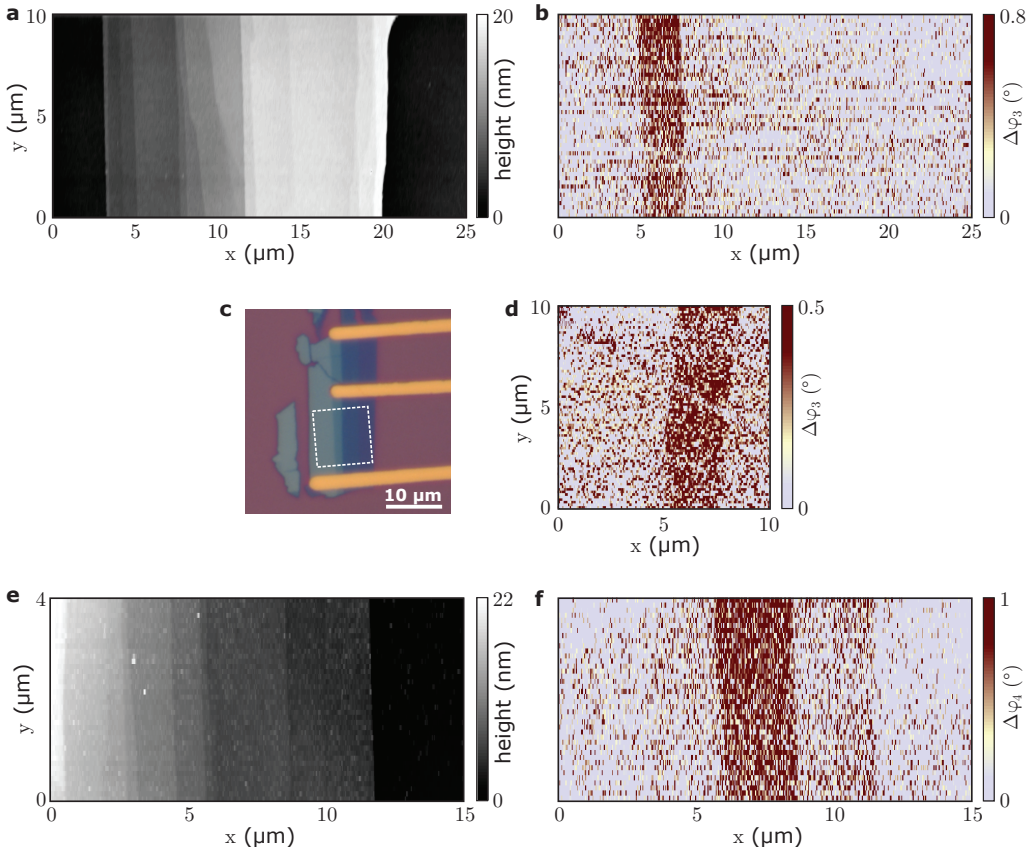

Figure 3.1: **Spatially resolved absorption maps.** All scans were taken at $E_{\text{ph}} = 117$ meV and the flakes were exfoliated on a Si/SiO_2 substrate. **a**, AFM image of a terraced WSe_2 flake. **b**, $\Delta\varphi_3$ on the same area of the flake as in **a**, obtained by taking the difference between two measurements with V_{BG} = -50 V and V_{BG} = 0 V, respectively. $\Delta\varphi_3$ is therefore directly proportional to the absorption due to electrostatically induced holes in WSe_2. The area with higher absorption corresponds to $N = 5$. **c**, Optical microscope image of another contacted WSe_2 flake, taken with 100x magnification. **d**, Spatial absorption map due electrostatically induced holes. The scan was taken over the region indicated by the dashed square in **a**. V_{BG} was modulated between 0 and -50 V with a frequency of 4.9 Hz. Enhanced absorption is observed in the area with $N = 5$. We note that during a previous measurement, the WSe_2 flake was damaged, resulting in a scratch that can be seen in **d** but was not yet present in the optical image of **c**. **e**, AFM image of a terraced MoS_2 flake. **f**, $\Delta\varphi_4$ on the same area of the flake as in **e**, obtained by taking the difference between two measurements with V_{BG} = -50 V and $V_{\text{BG}} = +50$ V, respectively. Here, $\Delta\varphi_4$ is proportional to the absorption due to electrostatically induced electrons. Enhanced absorption is observed in the area of the flake with $N = 5$.

simultaneously acquired spatial map of the absorption $\Delta\varphi_3$ for $E_{\text{ph}} = 117$ meV is shown in Figure 3.2c. We observe a clearly enhanced absorption in the areas of the flake with $N = 1$ and $N = 5$. When repeating the same scan at $E_{\text{ph}} = 165$ meV, we only observe absorption in the area with $N = 4$ (Figure 3.2d). This distinct behavior originates from two different

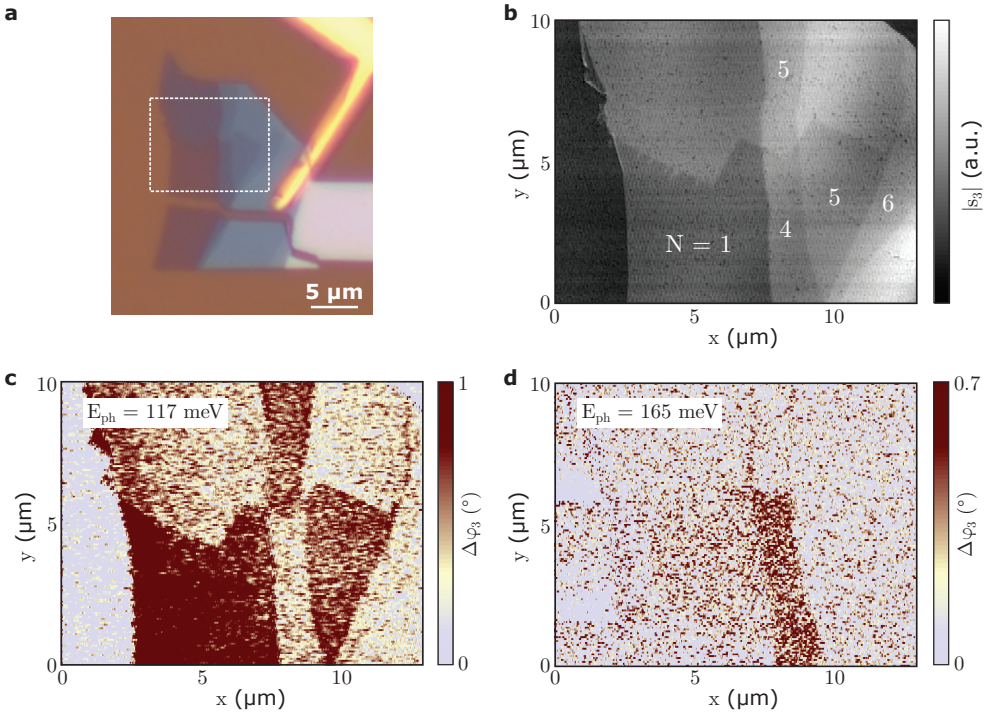

Figure 3.2: **Spatially resolved absorption at different illumination energies.** **a**, Optical microscope image of a WSe_2 flake on a home-grown HfO_2 substrate. **b**, Spatial map of $|s_3|$ in arbitrary units obtained by scanning the AFM tip over the area of the flake marked by the dashed lines in **a**. Different layer numbers can be identified by their optical signal and are indicated in the map. **c**, Spatial map of $\Delta\varphi_3$ obtained during the same scan as shown in **b** with $E_{\text{ph}} = 117$ meV. V_{BG} was modulated between 0 and -50 V with a frequency of 4.9 Hz. **d**, Same as in **c** but with $E_{\text{ph}} = 165$ meV.

absorption contributions. i) The enhanced absorption at $E_{\text{ph}} = 117$ meV in the area of $N = 5$ is the same effect that we had already observed in previous measurements. Observing enhanced absorption in the area with $N = 4$ for $E_{\text{ph}} = 165$ meV is a strong indication that this absorption indeed stems from intersubband transitions. ii) The absorption in the monolayer region at $E_{\text{ph}} = 117$ meV can be attributed to Drude absorption: Since the charge carriers induced by the applied V_{BG} are confined within a single atomic layer, the absorption due to free charge carriers is much higher than in the few-layer regions, where the same number of charge carriers is distributed over several layers. We study this effect in more detail in section 3.2.1.

3.2 Spectrally resolved measurements

In order to confirm our interpretation of absorption due to intersubband transitions and a Drude response, we took spectrally resolved measurements for different number of TMD layers N. In order to do so we used the s-SNOM to repeatedly scan one single line and

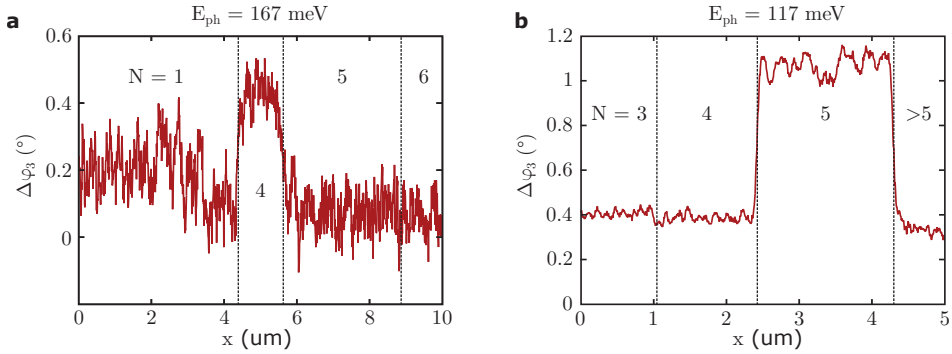

Figure 3.3: **Line scans for different illumination energies. a**, Average of 15 line scans on a terraced WSe_2 flake, exfoliated on a Si/HfO_2 substrate. The line scan was obtained by using the quantum cascade laser at $E_{ph} = 167$ meV. The modulation frequency of V_{BG} was 1.5 Hz and the integration time per pixel ∼50 ms. **b**, Similar measurement on a different WSe_2 flake, exfoliated on a Si/SiO_2 substrate. Here, we used the CO_2 laser at $E_{ph} = 117$ meV. The modulation frequency of V_{BG} was 3 Hz and the integration time per pixel ∼50 ms.

averaged these line scans. Examples of the resulting $\Delta\varphi_3$ are shown in Figures 3.3a and b for $E_{ph} = 167$ meV and $E_{ph} = 117$ meV, respectively. We observe that the signal to noise ratio under similar experimental conditions is much higher when using the CO_2 laser ($E_{ph} = 117$ meV), compared to the quantum cascade laser ($E_{ph} = 167$ meV), which we attribute to the excellent coherence properties of the CO_2 laser. Line scans with the CO_2 laser can therefore be acquired in a much shorter time compared to the quantum cascade laser, where we typically need to average more lines and also use a longer integration time per pixel in order to obtain a sufficiently high signal to noise ratio.

From the obtained averaged line scans, we took the average of $\Delta\varphi_3$ for each N, resulting in one spectral point for a given N. By repeating these measurements for varying E_{ph}, we obtained a complete spectrum of $\Delta\varphi_3$ for a WSe_2 flake exfoliated on Si/HfO_2 substrate (Figure 3.4a). We also calculated the relative permittivity ϵ_{WSe_2} by using the thin-film inversion model as described in section 2.2.2. Its imaginary part $\mathrm{Im}(\epsilon_{WSe_2})$ is shown in Figure 3.4b, where we assumed $\mathrm{Im}(\epsilon_{WSe_2}) = 0$ for charge-neutral WSe_2 in the mid-infrared frequency range. We observe that the qualitative features are similar in both $\Delta\varphi_3$ and $\mathrm{Im}(\epsilon_{WSe_2})$, but $\mathrm{Im}(\epsilon_{WSe_2})$ takes into account the flake thickness, the effect of the substrate, as well as any measurement parameters like tapping amplitude and demodulation order.

First, we identify a general decrease of $\mathrm{Im}(\epsilon_{WSe_2})$ with E_{ph} for all layer thicknesses, which we attribute to Drude absorption of free holes. Second, we observe a distinct absorption peak for $N = 4$ at $E_{ph} \approx 165$ meV, as well as enhanced absorption for $N = 5$ for low photon energies. These peaks in absorption fit well to the expected behavior of intersubband transitions. However, in order to be able to precisely quantify the absorption, we first model the Drude response due to the electrostatically induced free holes.

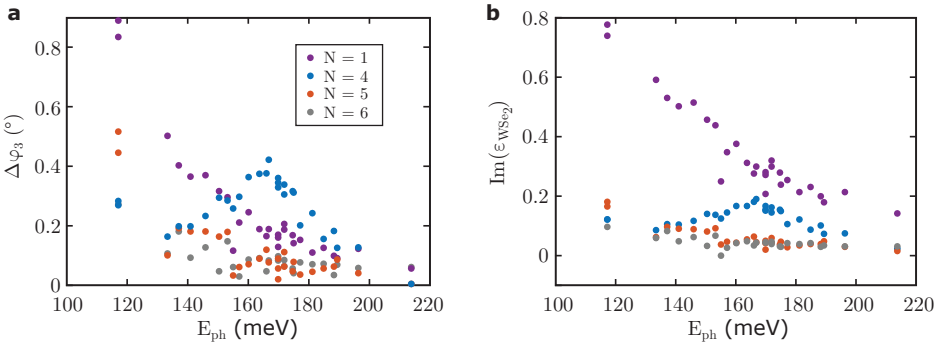

Figure 3.4: **Spectrally resolved measurements.** **a**, Experimentally obtained $\Delta\varphi_3$ for different E_{ph} on a single terraced WSe_2 flake (on a HfO_2 substrate) with different layer numbers N. **b**, Corresponding $\mathrm{Im}(\epsilon_{WSe_2})$, obtained by using the thin-film inversion model described in section 2.2.2. The thin-film inversion model takes into account the flake thickness, as well as any measurement parameters.

3.2.1 Modeling the Drude response

In our s-SNOM experiment we measure the complex permittivity of the sample at $E_{\mathrm{ph}} = \hbar\omega$, with $\hbar$ being the reduced Planck constant and ω the light angular frequency. However, the complex permittivity of any material that contains free charge carriers varies with ω. This can be seen by looking at the complex conductivity $\sigma(\omega)$ derived from the Drude model.[164,165]

In the Drude model, electrons or holes are assumed to behave like a free ideal gas[1] that scatter within the material with an average time of τ. We also assume the electrons to be driven by the oscillating electric field of our laser $\boldsymbol{E}_0 \mathrm{e}^{i\omega t}$. The equation of motion for the charge carriers can then be written as

$$m^*_{\mathrm{xy}} \frac{\mathrm{d}\boldsymbol{v}}{\mathrm{d}t} + \frac{m^*_{\mathrm{xy}} \boldsymbol{v}}{\tau} = e\boldsymbol{E}_0 \mathrm{e}^{i\omega t}, \tag{3.1}$$

where $\boldsymbol{v}$ is the drift velocity, m^*_{xy} is the in-plane effective mass (since charge carriers can only move freely in the in-plane dimensions) and e is the electron charge. We can solve this differential equation by using the ansatz $\boldsymbol{v} = \boldsymbol{v}_0 \mathrm{e}^{i\omega t}$ and obtain

$$\boldsymbol{v}_0 = \frac{e}{m^*_{\mathrm{xy}}} \frac{\boldsymbol{E}_0}{\tau^{-1} - i\omega}. \tag{3.2}$$

We can now derive σ by using the definition of the current density $\boldsymbol{j} = n_{3\mathrm{D}} e \boldsymbol{v}_0 = \sigma \boldsymbol{E}_0$, where $n_{3\mathrm{D}}$ is the three-dimensional charge carrier density (in SI units m^{-3}). This yields

[1] The Drude model is a classical model and does not take into account the quantum mechanical nature of the electrons. Surprisingly, however, it yields the same conductivity as the free electron (or Drude-Sommerfeld) model, which takes into account the Fermi-Dirac distribution of electrons.[166]

$$\begin{aligned}\sigma(\omega) &= \frac{n_{3D}e^2}{m^*_{xy}}\frac{1}{\tau^{-1}-i\omega} \\ &= \frac{D}{\tau^{-1}-i\omega},\end{aligned} \tag{3.3}$$

where we introduced the Drude weight $D = \frac{n_{3D}e^2}{m^*_{xy}}$. The material's complex relative permittivity $\epsilon(\omega)$ is related to $\sigma(\omega)$ as

$$\begin{aligned}\epsilon(\omega) &= \epsilon_{\text{core}}(\omega) + i\frac{\sigma(\omega)}{\epsilon_0\omega} \\ &= \epsilon_{\text{core}}(\omega) + \epsilon_{\text{Drude}}(\omega),\end{aligned} \tag{3.4}$$

where ϵ_0 is the vacuum permittivity and $\epsilon_{\text{core}}(\omega)$ summarizes other contributions to the permittivity, which can for example include exciton and phonon resonances. Furthermore, we can relate the scattering time τ to the material's charge carrier in-plane mobility $\mu = \frac{\tau e}{m^*_{xy}}$.

We can now fit ϵ_{Drude} to the measured ϵ_{WSe_2} for all N that do not show a resonance due to intersubband transitions. In the investigated range of E_{ph} these are the $N = 1$ and $N = 6$ areas of the WSe_2 flake. Figure 3.5 shows the measured doping-induced changes in permittivity $\Delta\,\text{Im}(\epsilon_{WSe_2})$ and $\Delta\,\text{Re}(\epsilon_{WSe_2})$ and the fits according to Equation 3.4. Each fit contains two free fitting parameters, D and τ, whose obtained values are listed in Table 3.1. We now assume effective in-plane hole masses of $m_{xy,N=1} = 0.64m_0$ [129] for $N = 1$ (at the K point of the Brillouin zone) and $m_{xy,N=6} = 0.82m_0$ [128] for $N = 6$ (at the Γ point). Furthermore, we can assume that V_{BG} induces a constant sheet carrier density n_{2D} for all N, so that $n_{3D} = n_{2D}/Nd_0$, where d_0 is the thickness of a single WSe_2 layer. This allows us to express D and τ in terms of the hole mobility μ and sheet carrier density n_{2D}. The obtained values are given in Table 3.1 with their corresponding 90% confidence values from the fit. We find hole mobilities that are consistent with previously reported values [81,167] and

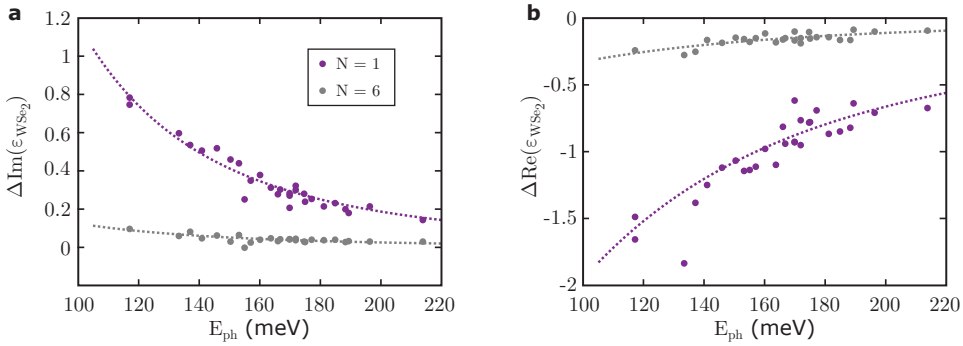

Figure 3.5: **a**, Measured hole-induced change in $\text{Im}(\epsilon_{WSe_2})$ for $N = 1$ (purple) and $N = 6$ (gray) on a WSe_2 flake exfoliated on a Si/HfO_2 substrate. The observed behavior can be well described by fitting a Drude model (dashed lines), according to Equation 3.4. **b**, Measured hole-induced change in $\text{Re}(\epsilon_{WSe_2})$ from the same measurement as in **a**. Dashed lines show the Drude fit.

layer numbers	fitted data	D in 10^{17} S/sm	τ in fs	n_{2D} in 10^{11} cm^{-2}	μ in cm^2/Vs
$N = 1$	$\mathrm{Re}(\epsilon_{WSe_2})$	6 ± 1	11 ± 6	$8.8^{+1.2}_{-1.5}$	30 ± 16
	$\mathrm{Im}(\epsilon_{WSe_2})$	5.3 ± 1.2	10^{+4}_{-3}	7.8 ± 1.8	28^{+10}_{-9}
$N = 6$	$\mathrm{Re}(\epsilon_{WSe_2})$	1.0 ± 0.3	9 ± 7	11^{+4}_{-3}	20 ± 15
	$\mathrm{Im}(\epsilon_{WSe_2})$	0.5 ± 0.1	7 ± 4	5.6 ± 1.4	15^{+8}_{-9}

Table 3.1: **Parameters obtained from the Drude fit to the data in Figure 3.5.**

sheet carrier densities that agree well with capacitance measurements performed on a separate device, yielding n_{2D} = 9x10^{11} cm^{-2}. This confirms that we can accurately model the Drude response of our device.

In order to account for the Drude contributions in the layer numbers that additionally show intersubband absorption ($N = 4$ and $N = 5$), we use the same fitting parameters as obtained from the fit to the $N = 6$ data and the relationship $n_{3D} = n_{2D}/Nd_0$. In this way we can extend the $N = 6$ fit to the $N = 4$ and $N = 5$ data without introducing any new fitting parameters. In order to quantitatively address the intersubband absorption resonances, we subtract the Drude contribution from the obtained $\mathrm{Im}(\epsilon_{WSe_2})$ (Figure 3.6a). We can now clearly distinguish an absorption peak for $N = 4$, as well as enhanced absorption for $N = 5$ at low photon energies. A Gaussian fit to the $N = 4$ data yields a center energy of 167.5 $\pm$ 1.5 meV and a full width half maximum $\Gamma = 33 \pm 4$ meV. The obtained $\mathrm{Re}(\epsilon_{WSe_2})$ for $N = 4$ (Figure 3.6b) also shows a resonance behavior at the same energy, supporting our conclusion that we indeed observe a resonant absorption. We can estimate the peak absorption for the $N = 5$ resonance to be located at 105 meV, assuming the same linewidth Γ and maximum absorption strength as for the $N = 4$ resonance. The corresponding guide to the eye for the $N = 5$ resonance is shown in Figure 3.6a. The experimentally observed resonance energies (168 meV and 105 meV for $N = 4$ and $N = 5$, respectively) are slightly higher than the theoretical predictions (144 meV and 92 meV – see Figure 3.6c), which may be due to many-body effects. It is well-known that many-body effects in thin TMD materials are extraordinary strong due to the reduced environmental screening and therefore dominate the observed optical absorption spectra in the visible and near-infrared region.[68,71,81,168,169] In future studies, it will therefore be interesting to see how the various many-body effects that are well-known from intersubband transitions in III-V semiconductors[170–173] manifest itself in TMD materials.

3.2.2 Discussions on the observed linewidth

We proceed with discussing the observed linewidth of the intersubband transitions. As we discussed in section 1.3, we expect that due to their atomically smooth surfaces the linewidth of intersubband transitions in TMDs is not significantly broadened by interface roughness scattering, which is a dominant broadening mechanism in III-V semiconductor quantum wells.[104–108] In section 1.4.4 we calculated the expected room-temperature linewidth $\Gamma = 5.9$ meV, which originates from thermal broadening due to differences in the in-plane effective masses of the

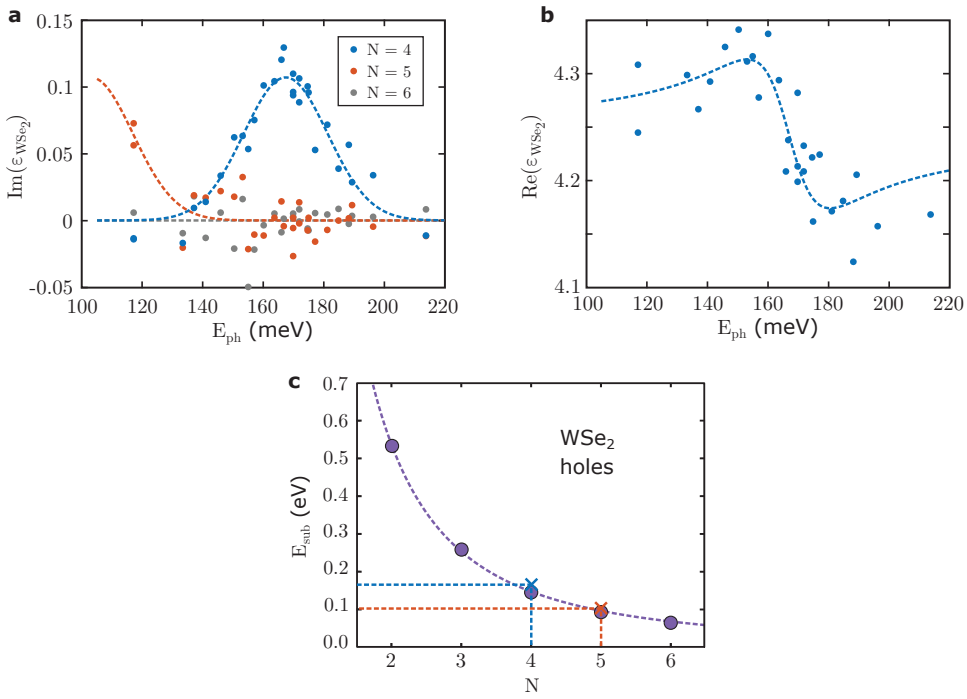

Figure 3.6: **Intersubband transitions in TMDs. a**, Experimentally obtained $\mathrm{Im}(\epsilon_{WSe_2})$ for different excitation photon energies E_{ph} and layer numbers N. The Drude contribution to the permittivity was subtracted in order to isolate the contributions due to intersubband transitions. The blue dashed line is a Gaussian fit to the $N = 4$ resonance and the orange dashed line is a guide to the eye to the $N = 5$ resonance. The experiment was performed at a sheet carrier density $n_{2D} = 9\text{x}10^{11}$ cm^{-2}. **b**, Experimentally obtained out-of-plane $\mathrm{Re}(\epsilon_{WSe_2})$ on the same flake as in **a**. The blue dashed line is a fit to the data using the real part of a complex Lorentzian function. **c**, Calculated transition energies from the first to the second subband for holes in WSe_2. Crosses indicate the experimentally obtained resonance peaks from **a**.

two subbands. The observed linewidth of $\Gamma = 33$ meV is much larger than this theoretical estimate. In order to account for this difference we need to examine in more detail the hot spot around the AFM tip apex that excites intersubband transitions. The near-field around the tip apex does not only provide the necessary out-of-plane polarization component, but the sharp tip apex also provides in-plane momentum $\boldsymbol{\xi}$. This leads to the excitation of non-vertical transitions with a finite momentum transfer. The effect of this momentum transfer is schematically shown in the insets of Figure 3.7a. Inset i) shows a possible transition from the bottom of the first subband to the second subband. It can be seen that this transition occurs at a larger photon energy than a transition excited by far-field light, which is vertical. This larger transition energy leads to a blue-shift of the resonance center energy. Insets ii) and iii) show transitions of thermally excited charge carriers. We can see that these transitions can either occur at higher or lower photon energies, leading to a low and high energy tail in the absorption spectrum.

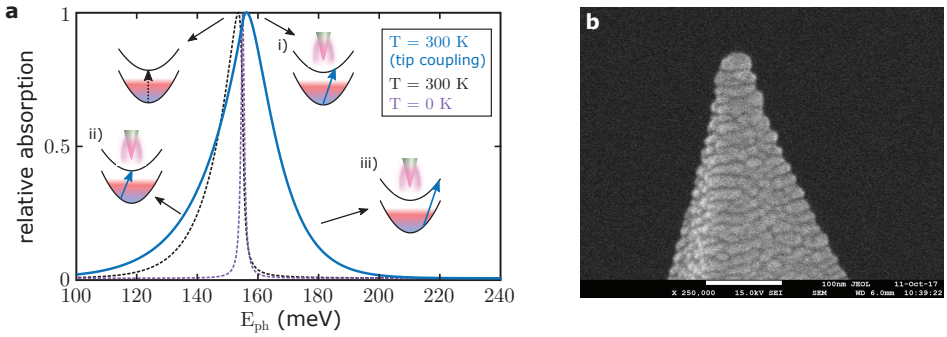

Figure 3.7: **Tip-induced linewidth broadening.** **a**, Calculated line shape of intersubband transitions mediated by the AFM tip with radius $a = 12$ nm (solid blue line) obtained by numerical integration of Equation 3.6. The thermally broadened (black dashed line) and phonon-limited (purple dashed line) line shapes are also shown for comparison. The insets show the different transitions responsible for i) the blue-shift of the resonance peak energy, ii) the tail towards lower and iii) towards higher energies. **b**, Scanning electron microscope (SEM) image of a PtIr-coated AFM tip as used for our experiments. The scale bar at the bottom is 100 nm. This particular tip has an apex radius of about 12 nm. The image was provided by NanoWorld AG.

In order to mathematically describe these transitions we need to model the momentum distribution around the AFM tip apex. It is given by a broad Bell shaped function, peaking at a momentum that is inversely related to the tip curvature.[174] The tip form factor is given in terms of the momentum $\boldsymbol{\xi}$ as

$$\rho_{\text{tip}}(\boldsymbol{\xi}) = \frac{1}{12\pi\xi_0^4}\xi^2 e^{-\xi/\xi_0}, \tag{3.5}$$

where $\xi_0 = \frac{\pi}{a}$, the tip radius a. The nominal tip radius of the AFM tips used in the experiment is $a < 10$ nm. However, a SEM image (Figure 3.7b) of a typical tip used in our experiments shows $a \approx 12$ nm, which we used for our calculations. We note that smaller features can occur due to smaller Pt grains at the AFM tip apex and smaller a leads to both a larger linewidth broadening and blue-shift of the resonance center energy. Due to the allowance of non-vertical optical transitions, the crystal momentum conservation is relaxed, which results in a modification of the transition rates (Equation 1.29) as follows

$$W_{12} = \frac{2\pi}{\hbar} g_s |E_z(\hbar\omega) d_z|^2 \sum_{\boldsymbol{\xi},\boldsymbol{k}} \rho_{\text{tip}}(\boldsymbol{\xi}) f(\boldsymbol{k}) \delta(E_2(\boldsymbol{k}+\boldsymbol{\xi}) - E_1(\boldsymbol{k}) - \hbar\omega). \tag{3.6}$$

This equation can be integrated numerically, resulting in the line shape displayed in Figure 3.7a. We obtain a linewidth $\Gamma = 24$ meV, indicating that tip-induced broadening plays an important role for the experimentally observed linewidth. However, we cannot exclude additional contributions to the linewidth broadening due to various forms of disorder.[105,175,176]

3.2.3 Spectrally resolved measurements on a SiO_2 substrate

In order to demonstrate the importance of the used substrate for the quantitative evaluation of the absorption, we performed spectrally resolved measurements on a WSe_2 flake exfoliated on a Si/SiO_2 substrate. The main issue of using a SiO_2 substrate can be readily seen from Figure 3.8a, which displays its relative permittivity ϵ_{SiO_2}.[177] We see that at around 130 meV (9.5 µm), SiO_2 shows a strong phonon resonance. This phonon resonance also influences $\mathrm{Re}(\epsilon_{SiO_2})$ at $E_{ph} \approx 165$ meV, the energy where we expect the intersubband transition for a $N = 4$ WSe_2 flake to occur. According to Equation 2.10, both the permittivity of the substrate and the permittivity of WSe_2 influence the optical signal and the impact of a change in the permittivity of WSe_2 depends on the substrate permittivity. In particular, we find that $\epsilon_{SiO_2} \approx 1$ at $E_{ph} \approx 165$ meV, which leads to a vanishing quasi-static reflection coefficient $\beta_{SiO_2} = \frac{\epsilon_{SiO_2}-1}{\epsilon_{SiO_2}+1}$. According to Equation 2.10 this makes the optical signal independent of ϵ_{SiO_2} and any change in the permittivity of WSe_2 will therefore be strongly reflected in the measured optical signal. One can intuitively understand this behavior as the permittivities of SiO_2 and the surrounding air become equal at $E_{ph} \approx 165$ meV, meaning that we essentially probe a suspended WSe_2 flake.

We can readily see this effect in the spectral measurements of a terraced WSe_2 flake with $N = 3$, 4, 5, 8, exfoliated on Si/SiO_2 substrate. The change in the phase of the optical signal $\Delta\varphi_3$ when V_{BG} was varied between -50 V (p-doped) and 0 V (charge neutral) is shown in Figure 3.8b. For a substrate with constant permittivity for all E_{ph}, $\Delta\varphi_3$ would directly be proportional to the absorption due to electrostatically induced holes. However, the spectrally varying permittivity of the underlying SiO_2 make this analysis more complicated. We first qualitatively examine the different features present in Figure 3.8b. First, we observe enhanced absorption for a WSe_2 thickness with $N = 5$ at $E_{ph} = 117$ meV. We have observed this behavior before and can attribute it to hole intersubband transitions. We now focus on the range of $E_{ph} = 165$–270 meV. Here, we observe a strong increase of $\Delta\varphi_3$ for $N = 3$ and $N = 4$ when approaching $E_{ph} = 165$ meV from higher energies. As in our previous analysis we can attribute the increase in $\Delta\varphi_3$ to a Drude response of free holes, but this effect is largely magnified since ϵ_{SiO_2} approaches 1. We can furthermore see that $\Delta\varphi_3$ is larger for $N = 4$ than for $N = 3$. This cannot be explained by a simple Drude response, since the Drude absorption due to free charge carriers is proportional to N^{-1}. Therefore, another absorption mechanism must be present for $N = 4$.

In order to investigate this additional absorption, we first calculate the relative permittivity of WSe_2 from the experimentally obtained optical signals by using the thin-film inversion model described in section 2.2.2. In principle, this model should completely eliminate any effect of the varying permittivity of SiO_2. However, possible deviations between the theoretical and actual values of ϵ_{SiO_2} introduce significant uncertainties. After the recovery of ϵ_{WSe_2}, we observe a monotonic decrease of $\mathrm{Im}(\epsilon_{WSe_2})$ for all N over our complete range of E_{ph} (Figure 3.8c). We are now in a position to model the Drude response of WSe_2 as described in section 3.2.1. We decided to fit $\mathrm{Im}(\epsilon_{WSe_2})$ for $N = 3$ with Equation 3.4 since we do not expect it to show any intersubband resonance in the experimental range of E_{ph} and it shows a much stronger Drude response than the area of the flake with $N = 8$. From the fit we obtained a Drude weight $D = 2.1 \pm 0.8$ S/sm and a scattering time $\tau = 2.4 \pm 1.7$ fs. These values

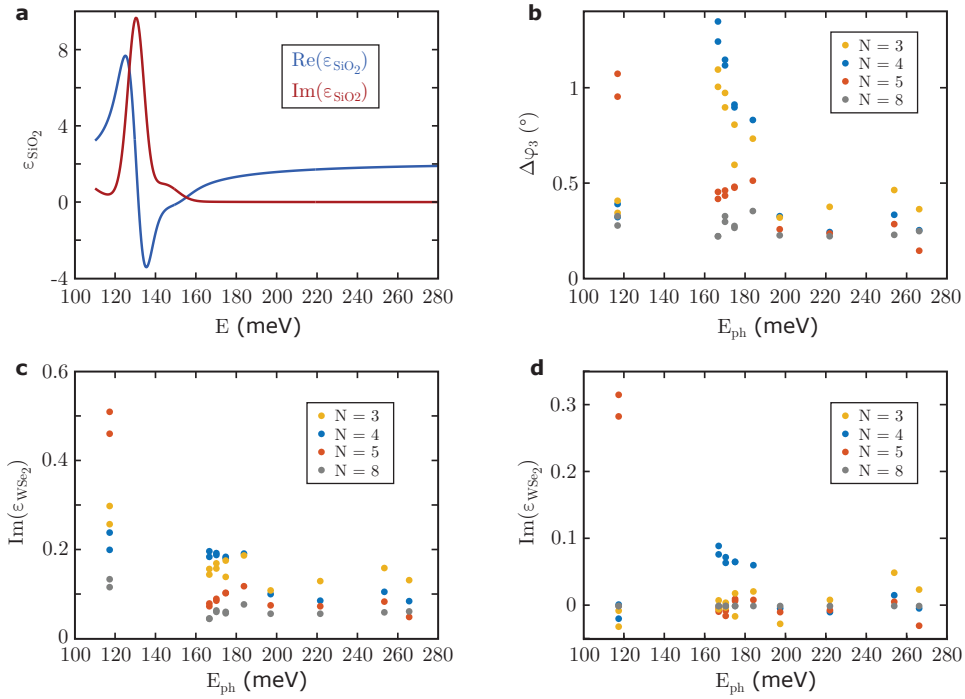

Figure 3.8: **Spectrally resolved measurements on a Si/SiO_2 substrate.** **a**, Real and imaginary part of the permittivity of SiO_2. Data taken from ref. 177. **b**, Experimentally obtained $\Delta\varphi_3$ for a terraced WSe_2 flake with different thicknesses N = 3, 4, 5, 8, exfoliated on Si/SiO_2 substrate. V_{BG} was varied between -50 V (p-doped) and 0 V (charge-neutral) with a frequency of 3 Hz. **c**, Obtained $\mathrm{Im}(\epsilon_{WSe_2})$ from the measurements shown in **b** by using the thin-film inversion model described in section 2.2.2. **d**, Same data as in **c**, with the Drude contribution to $\mathrm{Im}(\epsilon_{WSe_2})$ subtracted. We have also assumed $\mathrm{Im}(\epsilon_{WSe_2}) = 0$ for $N = 8$ and subtracted its value for all other layer numbers N to compensate for systematic errors arising during the measurements for different E_{ph}.

correspond to a sheet carrier density n_{2D} = 1.2 ± 0.4 x 10^{12} cm^{-2} and a mobility μ = 5.2 ± 3.6 cm^2/Vs, which are in good agreement with the measurements on the HfO_2 substrate (Table 3.1). We can now expand the Drude fit to all other layer numbers N by using the relationship $n_{3D} = n_{2D}/Nd_0$ without introducing any new fitting parameters.

As we have done for the measurements on the HfO_2 substrate, we now isolate the additional absorption due to intersubband transitions by subtracting the Drude response from the measured $\mathrm{Im}(\epsilon_{WSe_2})$. For each E_{ph} we furthermore assume $\mathrm{Im}(\epsilon_{WSe_2}) = 0$ for $N = 8$ and we subtract the corresponding value from all other N. This compensates for systematic errors arising in measurements with different E_{ph}. The resulting $\mathrm{Im}(\epsilon_{WSe_2})$ is shown in Figure 3.8d. As we could already see previously, we observe enhanced absorption at E_{ph} = 117 meV for N = 5. In addition, we can observe the beginning of a resonance for N = 4 at $E_{ph} \approx$ 165 meV. It is qualitatively and quantitatively similar to the observed resonance on the HfO_2 substrate, validating our previous interpretation. However, the resonance cannot be directly identified in the raw data showing $\Delta\varphi_3$ and a lot of data processing is necessary for it to be clearly seen,

where each step introduces uncertainties. It is therefore much more advantageous to use a substrate with an almost constant permittivity for the whole range of E_{ph}, as is the case for HfO_2.

3.3 Doping dependence and ambipolar absorption

We now study the doping dependence of intersubband transitions. According to Equation 1.19, the sheet absorption α depends linearly on the sheet carrier density n_{2D}. In order to experimentally study this dependence, we vary n_{2D} by changing the modulation amplitude of the backgate voltage $V_{\mathrm{BG,max}}$ at constant $E_{\mathrm{ph}} = 165$ meV, which corresponds to the center energy of the $N = 4$ intersubband resonance. The measured and Drude-corrected $\mathrm{Im}(\epsilon_{WSe_2})$ as a function of n_{2D} is shown in Figure 3.9. It displays a monotonic increase of the absorption with n_{2D}, which is consistent with the idealized square well model. We note, however, that the exact dependence of the absorption on doping can be influenced by possible contributions from many-body effects and non-parabolic bands. In our experiments, we can calculate the absorption α from the measured $\mathrm{Im}(\epsilon_{WSe_2})$ as described in section 2.2.2 and find a maximum value of $\alpha = 0.017 \pm 0.002$ % for the highest hole density $n_{2D} = 9 \times 10^{11}$ cm^{-2}, which we extracted from capacitance measurements on a separate device. This is in reasonable agreement with the idealized theoretical model yielding $\alpha = 0.026\%$ for a WSe_2 crystal with $N = 4$ and taking into account the measured linewidth $\Gamma = 33$ meV. We note that we achieve an extremely high sensitivity by using the s-SNOM. Assuming that we probe an effective area of the WSe_2 flake of $\pi a^2 \approx 300$ nm^2, where $a \approx 10$ nm is the AFM tip radius, this corresponds to a single charge carrier under the AFM tip for $n_{2D} \approx 3 \times 10^{11}$ cm^{-2}, a charge carrier density for which we can still observe intersubband transitions.

Finally, we demonstrate the versatility of 2D materials by ambipolar electrical control of intersubband transitions in the valence and conduction bands. We tuned n_{2D} from the p-doped to the n-doped regime and observed intersubband transitions in both cases. In order to

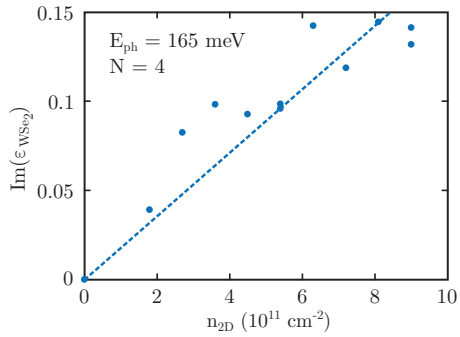

Figure 3.9: **Doping dependence of intersubband transitions.** Experimentally obtained $\mathrm{Im}(\epsilon_{WSe_2})$ for intersubband transitions at different charge carrier densities n_{2D}. n_{2D} was controlled by varying the modulation amplitude of V_{BG}. The measurements were obtained on the same device as in Figure 3.6 at $E_{\mathrm{ph}} = 165$ meV, which corresponds to the maximum of the $N = 4$ intersubband resonance.

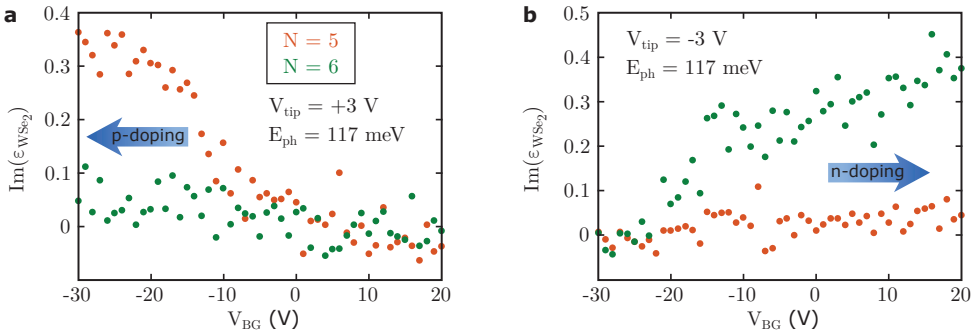

Figure 3.10: **Ambipolar intersubband absorption. a**, **b**, Observation of hole ($N = 5$) (**a**) and electron ($N = 6$) (**b**) intersubband transitions within the same WSe_2 flake at $E_{ph} = 117$ meV. Shown is the Drude corrected $\mathrm{Im}(\epsilon_{WSe_2})$. The DC V_{BG} was increased stepwise from -30 to +20 V. The measurement was performed on a WSe_2 flake on top of a Si/SiO_2 substrate. To reach higher doping levels, an additional DC voltage V_{tip} was applied between the WSe_2 flake and the AFM tip, which locally induced holes for $V_{tip} = +3$ V (**a**) or electrons for $V_{tip} =$ -3 V (**b**) due to capacitive interactions with the metalized, grounded AFM tip.

reach n- and p-doping without leakage through the underlying oxide we used the AFM tip to additionally dope the flake, as is described in section 2.2.5. In Figure 3.10a, we applied $V_{tip} = +3$ V, which locally p-doped the WSe_2 flake. By using a DC V_{BG} we could then increase or compensate for this p-doping. At $E_{ph} = 117$ meV in the $N = 5$ area of the flake, we observed an increase in hole intersubband absorption with increasing p-doping, a similar result as the previous doping dependence taken at $E_{ph} = 165$ meV with an AC V_{BG}. In the next measurement on the same flake and at the same E_{ph}, we applied $V_{tip} =$ -3 V (locally inducing electrons) and observed linearly increasing absorption with increasing n-doping in the area of the flake with $N = 6$ (Figure 3.10b). We attribute this behavior to electron intersubband transitions, which is in good agreement with our theoretical ab initio DFT calculations, where the electron transitions for a given E_{ph} occur in a thicker part of the flake than the hole transitions (Figure 1.9).

3.4 Conclusions

We used the s-SNOM to excite intersubband transitions and quantitatively evaluated their absorption. First, we performed spatial absorption measurements with a resolution of ~20 nm for fixed illumination photon energies E_{ph} and observed absorption resonances for specific layer numbers N, depending on E_{ph}. We repeated these measurements on several different flakes, using different TMD materials (WSe_2 and MoS_2), different substrates (SiO_2 and HfO_2) as well as DC and AC V_{BG} to dope the TMD flakes. Next, we performed spectrally resolved measurements on a WSe_2 flake on a HfO_2 substrate, which we chose due to its absence of phonons in the investigated range of E_{ph}. We observed an in-plane Drude response that we could fit well with a standard Drude model and we observed out-of-plane intersubband resonances centered at $E_{ph} = 168$ meV for $N = 4$ and $E_{ph} \approx 105$ meV for $N = 5$. These center energies are higher than the predictions obtained by DFT calculations and are likely

influenced by many-body effects, which we expect to be strong in TMDs due to the reduced dielectric screening. The observed linewidth is $\Gamma = 33$ meV, which is much larger than the theoretically calculated linewidth. We found that a large contribution to the linewidth stems from non-vertical transitions due to a momentum transfer from the AFM tip. However, we cannot disentangle different contributions to the linewidth and are therefore unable to quantify possible contributions from substrate- or defect-induced disorder. The intrinsic linewidth of intersubband transitions in TMDs has therefore still to be determined experimentally. Finally, we investigated the doping dependence of intersubband transitions. We found a linear increase of absorption with doping, which is in good agreement with an idealized infinite square well model. We also demonstrated ambipolar behavior of WSe_2 showing hole intersubband transitions for areas of the flake with layer number $N = 5$ and electron transitions for areas with $N = 6$, for the same illumination energy $E_{\text{ph}} = 117$ meV.

4 Interactions between intersubband transitions and 2D polaritons

In this chapter, we investigate the interactions between intersubband transitions in TMDs and graphene plasmons or hBN hyperbolic phonon polaritons. The work presented here was carried out together with Nicola Melchioni as part of his master's thesis[178] and together with Md Masudur Rahman as part of an internship project.[179] We first review the most important properties of graphene plasmons and hBN hyperbolic phonon polaritons with particular emphasis on their excitation and detection by using the s-SNOM. We then simulate the interaction between these polaritons and intersubband transitions by performing transfer matrix method and finite difference time domain simulations for various device geometries. Finally, we proceed with the experimental measurements, where we first characterize graphene plasmons and hBN phonon polaritons before investigating their interactions with intersubband transitions in WSe_2.

4.1 Introduction

The interactions between electromagnetic waves of a light field and electric (or magnetic) dipole excitations in matter are of great interest for both fundamental science as well as technological applications.[180] In this chapter, we consider the interaction between graphene plasmons and intersubband transitions in TMDs. This is a very promising material system since the electric field in graphene plasmons shows confinement to deep subwavelength volumes, which leads to a strongly enhanced field density compared to free space light.[181–183] The plasmons furthermore show an out-of-plane component of the electric field, which allows for the interaction with the out-of-plane dipole moment of intersubband transitions. We can combine TMDs and graphene into van der Waals heterostructures, separated by a spacer layer of hexagonal boron nitride (hBN). This hBN can be arbitrarily thin – up to the limit of a single atomic layer – leading to a strong overlap of the plasmonic fields with the intersubband transitions. Experimentally, both TMD intersubband transitions and graphene plasmons can be excited and detected by using the s-SNOM,[184,185] which allows us to directly investigate their interaction. A similar polaritonic mode as graphene plasmons also exists in hBN – the hyperbolic phonon polaritons. For simplicity, we limit ourselves to the theoretical description of the interaction between intersubband transitions and graphene plasmons, but the same theory can also be extended to hBN hyperbolic phonon polaritons.

4.1.1 Purcell enhancement

An important concept to enhance light-matter interaction relies on the so-called Purcell effect.[186] When a dipole emitter is placed inside a resonant cavity, it's spontaneous emission rate is enhanced by the Purcell factor

$$P = \frac{3}{4\pi^2}\left(\frac{\lambda_0}{n}\right)^3 \frac{Q}{V}, \tag{4.1}$$

where λ_0 is the emitter's free space wavelength, n is the refractive index of the cavity, Q is its quality factor and V its mode volume. There are two main approaches to reach high Purcell factors. Either by increasing the quality factor of the cavity or by decreasing its mode volume. The mode volume of a cavity can typically not be smaller than λ_0^3 and for mid-infrared frequencies it is difficult to increase Q due to the lack of high quality cavities. Therefore, the observed Purcell factors from intersubband transitions are typically rather small.[187,188] Here, the coupling of TMD intersubband transitions to graphene plasmons holds enormous opportunities to achieve large Purcell factors due to the large confinement of the electric field within the plasmons and the correspondingly small mode volume V. We can estimate the Purcell enhancement by first calculating the photon emission rate Γ_0 of intersubband transitions (assumed to be an out-of-plane dipole) into free space by using Fermi's Golden Rule

$$\Gamma_0 = \frac{\omega^3 |\mu_{12}|^2}{3\pi\epsilon_0 \hbar c^3}, \tag{4.2}$$

with the angular frequency of the free space light ω and dipole matrix element of the transition μ_{12}. Using typical values for a TMD quantum well ($\frac{\omega}{c} = \frac{2\pi}{10.6\ \mu m}$ and $|d_{12}| = \frac{16}{9\pi^2} ed$, with the electron charge e and TMD quantum well thickness $d = 3.5$ nm), we obtain a radiative free space decay rate $\Gamma_0 \approx 241$ kHz. When placing this out-of-plane dipole in close proximity to a doped graphene sheet that can sustain plasmons, this decay rate is modified due to the additional decay channel of intersubband transitions to graphene plasmons. The emission rate to graphene plasmons Γ_{pl} for small distances z between the quantum well and graphene is given as[182]

$$\Gamma_{\text{pl}} = \frac{2(2\pi)^4 |\mu_{12}|^2}{4\pi\epsilon_0 \hbar \left(\epsilon_{\text{top}} + \epsilon_{\text{bottom}}\right)} \frac{\mathrm{e}^{-4\pi z/\lambda_{\text{pl}}}}{\lambda_{\text{pl}}^3}, \tag{4.3}$$

where ϵ_{top} and ϵ_{bottom} are the real parts of the relative permittivities of the surrounding media and λ_{pl} is the graphene plasmon wavelength. Assuming graphene encapsulated in hBN with $\epsilon_{\text{top}} = \epsilon_{\text{bottom}} \approx 2$, $\lambda_{\text{pl}} = 50$ nm and $z = 2$ nm, we obtain $\Gamma_{\text{pl}} \approx 3.3\text{x}10^{12}$ Hz. This corresponds to a Purcell factor $P = \frac{\Gamma_{\text{pl}}}{\Gamma_0} \approx 1.4\text{x}10^7$. The radiative decay rate of intersubband transitions (to graphene plasmons) now becomes comparable to the non-radiative decay rate due to optical phonons ($\gamma_{\text{isb}} \approx 3.8\text{x}10^{12}$ Hz at room temperature, see section 1.4.4). This would allow for the fabrication of efficient electroluminescent devices, where photons can be outcoupled via graphene plasmons. Similar device geometries could also be used to efficiently launch graphene plasmons via intersubband transitions driven by an electric current across the TMD quantum well.

4.1.2 Strong coupling

Another regime of light-matter interaction is the strong coupling regime. The strong coupling regime is characterized by the energy exchange rate g_0 between the matter and light part of the interaction[189]

$$g_0 = E_{\text{vac}} \mu_{12} \sqrt{N_{\text{e}}}, \tag{4.4}$$

where μ_{12} is the dipole matrix element of the transition and N_{e} is the number of dipoles taking part in the interaction. The electric field due to vacuum fluctuations is given as

$$E_{\text{vac}} = \left(\frac{\hbar\omega}{2\epsilon_0 V}\right)^{1/2}, \tag{4.5}$$

with the light angular frequency ω and mode volume V of the electric field. This leads to

$$g_0 = \left(\frac{\omega \mu_{12}^2 N_{\text{e}}}{2\hbar\epsilon_0 V}\right)^{1/2}. \tag{4.6}$$

The strong coupling regime is reached when g_0 exceeds both the dissipation rates of light and matter fields. This leads to the formation of two polariton branches, which are the new

eigenstates of the system. The so-called Rabi splitting between these two branches is given by $2\hbar g_0$. Intersubband transitions are ideally suited to reach the strong coupling regime due to their enormous dipole moments μ_{12} and intersubband polaritons have been observed in a wide range of geometries, where the electromagnetic field was tailored and amplified by various cavity designs,[190–193] metallic gratings,[194–197] metamaterial resonances,[198,199] or electronic inductance-capacitance microcavity resonators.[200,201] Coupling intersubband transitions to graphene plasmons has the additional benefit of the small mode volumes that can be reached due to the strong electric field confinement associated with graphene plasmons. We estimate $g_0 \approx 2.8\text{x}10^{12}$ Hz x $\sqrt{N_e}$, by assuming a plasmon mode volume $V \approx \lambda_{\text{pl}}^3 = (50 \text{ nm})^3$ for a free space wavelength $\lambda_0 = 10.6$ µm (117 meV). The decay time of graphene plasmons at room temperatures can be as long as 1 ps, which corresponds to a decay rate $\gamma_{\text{pl}} = 10^{12}$ Hz. The non-radiative decay rate of intersubband transitions due to optical phonons at room temperature is given as $\gamma_{\text{isb}} \approx 3.8\text{x}10^{12}$ Hz (see section 1.4.4). By these estimations, we see that we can almost reach the strong coupling regime between intersubband transitions and graphene plasmons, depending on the number of charge carriers N_e that effectively take part in the interaction. This in turn depends on the doping of the quantum well, as well as on the exact device structures that we use.

In the following sections, we first introduce the general concepts of graphene plasmons and hBN hyperbolic phonon polaritons. We then present theoretical calculations on the coupling between the graphene plasmons and intersubband transitions in TMDs, obtained by using the transfer matrix method and finite difference time domain simulations. In the subsequent experimental part, we performed s-SNOM measurements on various van der Waals heterostructures on which we observed graphene plasmons and hBN hyperbolic phonon polaritons and investigated their interaction with intersubband transitions.

4.2 Theoretical description

4.2.1 Graphene plasmons

Graphene was the first 2D material isolated by Novoselov and Geim in 2004[22] and was explicitly mentioned when the Nobel Prize in 2010 was awarded for 'groundbreaking experiments regarding the two-dimensional material graphene'.[27,28] In the following we will review graphene's most important properties for the propagation and detection of mid-infrared plasmons.

General introduction to graphene

Graphene consists of a single layer of carbon atoms, which are arranged in a honeycomb lattice (Figure 4.1a). Its planar structure and strong intralayer bonds stem from the sp^2-hybridized σ-bonds in the in-plane direction. In the out-of-plane direction, π-bonds lead to weak interlayer interaction and allow for easy mechanical exfoliation. As in TMDs, the hexagonal lattice in real space also leads to a hexagonal lattice in reciprocal space. The bandstructure of graphene can be calculated by using a tight-binding model, taking into account each atom's nearest- and next-nearest-neighbor hopping terms.[202,203] Of particular interest are the K and K' point of

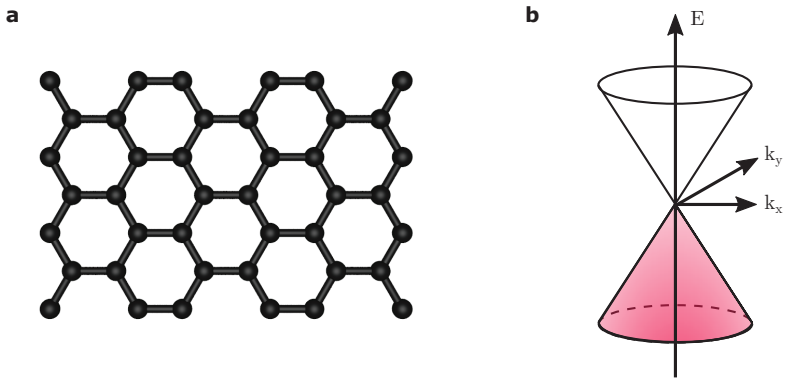

Figure 4.1: **Real space lattice and bandstructure of graphene. a**, Illustration of graphene's hexagonal real space lattice. **b**, Electron dispersion of graphene, showing the typical Dirac cones. The purple color indicates that the valence band is filled up to the Dirac point and graphene is therefore undoped. Adapted from ref. 204.

the Brillouin zone. At these points, the valence and conduction bands touch with a vanishing density of states. Graphene is hence a semimetal. The bandstructure around the Dirac points can be approximated as

$$E_{\pm}(\boldsymbol{k}) = \pm\hbar v_{\mathsf{F}}\boldsymbol{k}, \tag{4.7}$$

where $\boldsymbol{k}$ is the two-dimensional momentum vector and $v_{\mathsf{F}} \approx c/300$ is the graphene Fermi velocity and c the speed of light. It becomes evident that graphene has a light-like dispersion relation around the Dirac points (Figure 4.1b) and charge carriers within graphene are therefore often referred to as massless Dirac fermions.[23,24] Another important property of graphene is the linear scaling of the density of states with energy with respect to the Dirac point, $\rho(E) \propto |E|$. As a consequence, graphene's Fermi energy E_{F} is tunable by electrostatically inducing a sheet carrier density n_{2D}

$$E_{\mathsf{F}} = \hbar v_{\mathsf{F}} k_{\mathsf{F}} = \hbar v_{\mathsf{F}}\sqrt{\pi n_{\mathsf{2D}}}, \tag{4.8}$$

where k_{F} is the Fermi wavevector.

Plasmon polaritons in graphene

For sufficiently large doping, graphene can sustain plasmon polaritons, which are electromagnetic modes that propagate along the graphene sheet as is illustrated in Figure 4.2a. These collective charge oscillations can only occur for a negative real part of the permittivity.[169] In graphene, the negative permittivity stems from a Drude response of the free charge carriers, which typically happens at mid-infrared and THz frequencies (Figure 4.2b). The Drude response for graphene is given as[182]

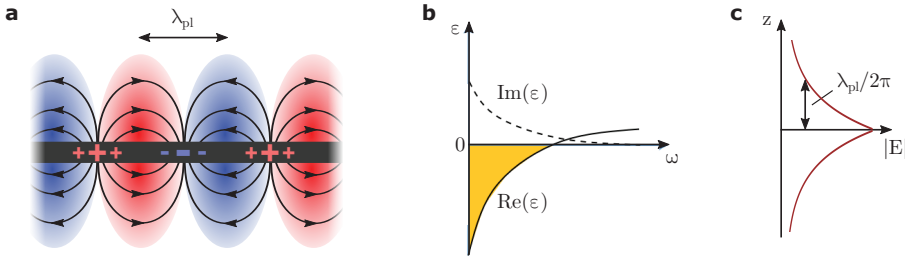

Figure 4.2: **Graphene plasmon polaritons. a**, Illustration of the collective charge oscillation of graphene plasmons. Electric field lines are represented by the arrows and the plasmon wavelength λ_{pl} is given. Adapted from ref. 204. **b**, Real and imaginary part of the permittivity of a typical Drude material. A necessary condition for the existence of graphene plasmons is $\mathrm{Re}(\epsilon) < 0$, which is fulfilled in the region that is marked in yellow. Adapted from ref. 169. **c**, Decay of the electric field of graphene plasmons in the out-of-plane direction. The electric field amplitude $|E|$ decays to $1/e$ over a distance of $\lambda_{\mathrm{pl}}/2\pi$.

$$\sigma(\omega,\tau) = \frac{e^2 E_{\mathrm{F}}}{\pi\hbar^2}\frac{i}{\omega + i\tau^{-1}}, \tag{4.9}$$

where τ is the carrier scattering time of graphene. For sufficiently high E_{F}, the dispersion relation of graphene plasmon polaritons can be described as

$$q_{\mathrm{pl}}(\omega,\tau) \approx \omega\epsilon_0(\epsilon_1+\epsilon_2)\frac{i}{\sigma(\omega,\tau)}, \tag{4.10}$$

where ϵ_1 and ϵ_2 are the real parts of the permittivities of the materials surrounding graphene. Upon insertion of the Drude conductivity (Equation 4.9), we obtain

$$\begin{aligned} q_{\mathrm{pl}} &= \frac{\pi\hbar^2}{e^2 E_{\mathrm{F}}}\epsilon_0(\epsilon_1+\epsilon_2)\omega(\omega+i\tau^{-1}) \\ &= k_{\mathrm{pl}} + i\,\mathrm{Im}(q_{\mathrm{pl}}). \end{aligned} \tag{4.11}$$

Here, $k_{\mathrm{pl}} = \frac{2\pi}{\lambda_{\mathrm{pl}}}$ is the plasmon wave vector in the direction of propagation with a plasmon wavelength λ_{pl}. The plasmon losses are given by the term $\mathrm{Im}(q_{\mathrm{pl}})$. We can readily see the square-root dispersion relation of graphene plasmons, $\omega \propto \sqrt{k_{\mathrm{pl}}}$. We also see that the plasmon wavelength is proportional to the Fermi energy, $\lambda_{\mathrm{pl}} \propto E_{\mathrm{F}}$. This leads to one of the unique properties of graphene plasmons, namely its in situ tunability of λ_{pl} by varying E_{F} through electrostatic doping. There are two commonly used figures of merit defined for plasmon polaritons. First, $\gamma^{-1} = k_{\mathrm{pl}}/\mathrm{Im}(q_{\mathrm{pl}})$, where $\gamma^{-1}/2\pi$ gives the number of cycles a plasmon can travel before decaying by $1/e$. The quality of graphene is therefore of great importance, as high quality graphene leads to a long scattering time τ and therefore to a large decay length. In highest quality hBN-encapsulated graphene values as high as $\gamma^{-1} > 25$ have been reported at room temperature.[49] This is a larger propagation length than previous studies on a SiO_2 substrate ($\gamma^{-1} \sim 5$), where losses are dominated by ionized substrate impurities.[184,185] At cryogenic temperatures $\gamma^{-1} \sim 130$ has been reported.[205] The second

figure of merit is the light confinement factor $\beta = \frac{\lambda_0}{\lambda_{pl}}$, where λ_0 is the free space wavelength. From Equation 4.11 we can derive β as

$$\beta = \frac{\lambda_0}{\lambda_{pl}} = \frac{1}{\alpha}\frac{\epsilon_1 + \epsilon_2}{4}\frac{E_{ph}}{E_F}, \tag{4.12}$$

where we introduced the fine structure constant $\alpha = \frac{1}{4\pi\epsilon_0}\frac{e^2}{\hbar c} \approx \frac{1}{137}$. For mid-infrared frequencies, we typically find $\frac{\epsilon_1+\epsilon_2}{4}\frac{E_{ph}}{E_F} \sim 1$, meaning that a confinement $\beta \approx 1/\alpha > 100$ can be achieved.[49] Furthermore, the out-of-plane decay length of the electromagnetic field is of particular importance for our experiments. For free standing graphene, this decay length is given as $1/k_{pl} = \lambda_{pl}/2\pi$ (Figure 4.2c).

Finally, it is evident from Equation 4.10 that the plasmon dispersion relation depends on the conductivity of graphene. There are different models to calculate the graphene conductivity. The Drude model discussed above is a good approximation for $E_{ph} \ll E_F$, where optical interband transitions do not influence the graphene conductivity. The local random phase approximation (RPA) additionally includes these interband transitions and is therefore more accurate for larger E_{ph}.[182,206,207] In the non-local RPA, the graphene conductivity also depends on the charge carrier momentum, $\sigma(\omega, q)$. These corrections become important for plasmons with a large momentum. More details on the non-local RPA can be found in refs. 206, 207.

Excitation and detection of plasmon polaritons in graphene by using the s-SNOM

Due to the large confinement factors $\beta > 100$, there is a huge momentum mismatch between free-space photons and graphene plasmons. This poses a large challenge to efficiently couple far-field light to graphene plasmons. The first observation of graphene plasmons were therefore based on electron spectroscopy.[208–210] Another possibility is to nano-pattern graphene to ribbons with a width on the order of the plasmon wavelength. Graphene plasmons can then be resonantly excited with far-field light.[211–217] This approach is challenging, however, since the ribbon width needs to be constant over the whole device area in order to avoid inhomogenous broadening of the observed resonance. In our experiments we use a different approach:[184,185] We illuminate the AFM tip of the s-SNOM, whose sharp tip apex provides the necessary momentum[174] to couple far-field light to graphene plasmons. The AFM tip then launches radial graphene plasmons, which propagate towards the graphene edges, where they are reflected. The reflected plasmons travel back to the tip again, interfering with the counterpropagating plasmons to form standing waves with a fringe spacing of $\lambda_{pl}/2$. By scanning the AFM tip over the graphene sheet, we can detect this standing wave pattern as fringes that are parallel to the graphene edge, as is schematically depicted in Figure 4.3.

Another contribution to the detected optical signal are plasmon polaritons that are launched at the graphene edge. These plasmon polaritons only travel the distance from the graphene edge to the AFM tip and therefore half the distance as the tip-launched plasmons. Taking into account these two contributions to the measured plasmon signal, we can derive the following equation that describes well the observed optical signal[49,204]

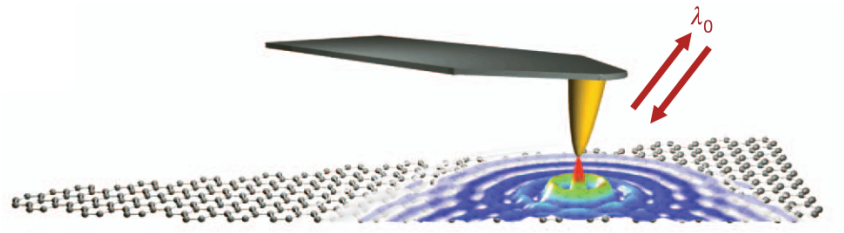

Figure 4.3: **Illustration of the launching and detection of graphene plasmons.** The metallized AFM tip of the s-SNOM is illuminated by far-field light with a wavelength λ_0. The sharp tip apex provides the necessary momentum to couple the far-field light to graphene plasmons, which are radially launched from the tip. They get reflected at the graphene edges, forming a standing wave pattern with a fringe spacing of $\lambda_{\mathrm{pl}}/2$, which is detected in the optical signal ξ_{opt} of the s-SNOM. A spatial map of this standing wave pattern can be obtained by scanning the AFM tip over the graphene sheet. Adapted from ref. 184.

$$\xi_{\mathrm{opt}}(x) = \xi_{\mathrm{bulk}}(x) + \underbrace{A\frac{\mathrm{e}^{i2q_{\mathrm{pl}}x}}{\sqrt{x}}}_{\text{tip-launched}} + \underbrace{B\frac{\mathrm{e}^{iq_{\mathrm{pl}}x}}{x^a}}_{\text{edge-launched}} , \tag{4.13}$$

where A, B, and q_{pl} are complex fitting parameters and a is a real fitting parameter. $\xi_{\mathrm{bulk}}(x)$ is the detected background signal, which can vary with the position of the tip ($x = 0$ denotes the graphene edge). The additional decay $\propto \sqrt{x}$ for the tip-launched plasmons (that travel a distance of $2x$) is a geometrical decay due to the radially propagating graphene plasmons away from the tip apex. For the edge-launched plasmons (that travel a distance of x) there are several factors that can contribute to the function for the geometrical decay and it is not known a priori. We therefore allow it to be a free fitting parameter, with a typical value $a \sim 1$.

4.2.2 hBN hyperbolic phonon polaritons

Hexagonal boron nitride (hBN) is the closest relative to graphene in terms of its lattice structure. As graphene, it consists of a hexagonal lattice, with the difference that the carbon atoms are alternatingly replaced by boron and nitrogen atoms. hBN is an electrical insulator, with a bandgap of $\sim$6 eV[218] and interband transitions are therefore forbidden at the photon energies used in our experiments. hBN provides an atomically flat substrate to other 2D materials with very little defects. It is therefore an excellent material for encapsulating graphene and other 2D materials, revealing appealing electrical properties, such as intrinsic phonon-limited mobilities of 140,000 $\frac{\mathrm{cm}^2}{\mathrm{Vs}}$ at room temperature in graphene,[17,219,220] mobilities >30,000 $\frac{\mathrm{cm}^2}{\mathrm{Vs}}$ in MoS_2[42] and the quantum hall effect in WSe_2[66] and InSe.[221]

Like most 2D materials, hBN is a birefringent material, meaning that it has different relative permittivities in the in-plane and out-of-plane directions due to its layered nature. In particular, hBN shows hyperbolicity in the so-called reststrahlen bands, which is an extreme case of birefregence. In these spectral regions not only the values of the relative permittivities are

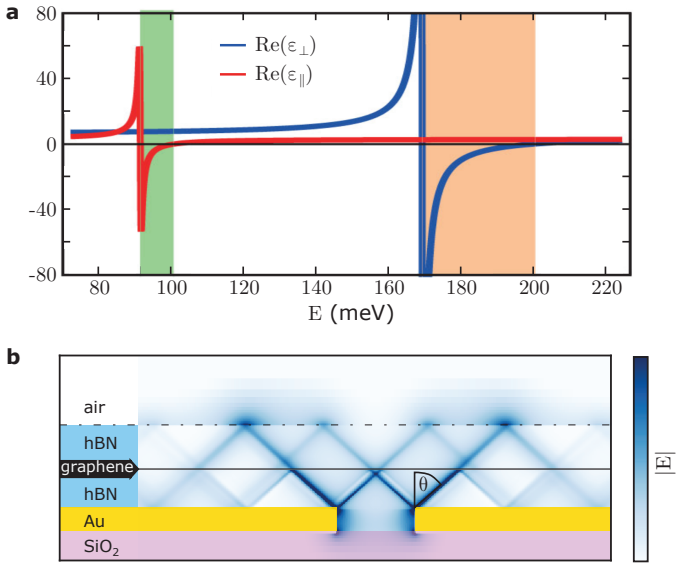

Figure 4.4: **Hyperbolic phonon polaritons in hBN. a**, Real part of the in-plane ($\epsilon_\perp$) and out-of-plane permittivity ($\epsilon_\parallel$) of hBN. Spectral regions with different signs of $\epsilon_\perp$ and $\epsilon_\parallel$ support the propagation of hyperbolic phonon polaritons. These regions are called the reststrahlen bands and are highlighted in green and orange for the lower and higher reststrahlen band, respectively. Adapted from ref. 222. **b**, Finite difference time domain simulations of propagating hyperbolic phonon polaritons in hBN. In these simulations, the phonon polaritons are launched at the Au edges, which provide the necessary momentum. They are then partially absorbed when crossing the graphene. The angle of propagation θ is given by Equation 4.16. Adapted from ref. 223.

different but also their signs (Figure 4.4a). The negative sign of the real part of the permittivity in one direction is caused by optical phonon resonances. Isofrequency surfaces – defined by $\omega(\boldsymbol{k}) = \text{constant}$ – are given as[224]

$$\frac{k_\parallel}{\epsilon_\perp(\omega)} + \frac{k_\perp}{\epsilon_\parallel(\omega)} = \frac{\omega}{c}, \tag{4.14}$$

where $\parallel$ and $\perp$ stand for the out-of-plane and in-plane component of the wavevector $\boldsymbol{k}$ and hBN relative permittivity ϵ. Due to the different signs of $\epsilon_\perp(\omega)$ and $\epsilon_\parallel(\omega)$, k can be much larger than $\frac{2\pi}{\lambda_0}$. In these spectral regions, hBN therefore supports the propagation of hyperbolic phonon polaritons, which result from the coupling of photons to optical phonons. Phonon polaritons propagate as directional rays, as is illustrated in Figure 4.4b. For small polariton wavelengths $\lambda_{\text{ph}} \ll \lambda_0$ their dispersion relation is given as[225]

$$\begin{aligned} q_{\text{ph}} &= \frac{i}{d}\sqrt{\frac{\epsilon_\parallel}{\epsilon_\perp}}\left[\arctan\left(\frac{\epsilon_{\text{top}}}{\sqrt{\epsilon_\perp\epsilon_\parallel}}\right) + \arctan\left(\frac{\epsilon_{\text{bottom}}}{\sqrt{\epsilon_\perp\epsilon_\parallel}}\right)\right] \\ &= k_{\text{ph}} + i\,\text{Im}(q_{\text{ph}}) \end{aligned} \tag{4.15}$$

where $\epsilon_{\text{top}}(\omega)$ and $\epsilon_{\text{bottom}}(\omega)$ are the relative permittivities of the top and bottom substrate, d is the hBN thickness and $k_{\text{ph}} = \frac{2\pi}{\lambda_{\text{ph}}}$, with the phonon polariton wavelength λ_{ph}. The propagation angle $\theta(\omega)$ of the phonon polaritons with respect to the out-of-plane axis can directly be calculated from Equation 4.14 and is given as

$$\theta(\omega) = \arctan\left(-i\sqrt{\frac{\epsilon_{\parallel}(\omega)}{\epsilon_{\perp}(\omega)}}\right). \tag{4.16}$$

There are two spectral regions in which hBN supports the propagation of hyperbolic phonon polaritons: The lower reststrahlen band from ∼94–102 meV (∼13.2–12.1 µm) and the upper reststrahlen band from ∼169–201 meV (∼7.4–6.2 µm). In the upper reststrahlen band, several studies reported the observation of hyperbolic phonon polaritons by using the s-SNOM.[223,225–230] Similar as for graphene plasmons, the sharp AFM tip apex provides the necessary momentum to launch the hyperbolic phonon polaritons in hBN, which are then detected in the optical signal as fringes with a spacing of $\lambda_{\text{ph}}/2$. A similar study proves to be more difficult for the lower reststrahlen band due to the lack of coherent light sources, but progress has been made towards photon-free detection without the need for coherent excitation.[231] For our study we limit ourselves to the upper reststrahlen band due to the laser sources available. The typical reported confinement values of up to $\beta \sim 25$ are smaller than in graphene plasmons but still constitute a significant confinement of the electric field. The propagation lengths at room temperature $\gamma^{-1} \sim$ 20–35 can be higher than in graphene plasmons since phonon polaritons do not suffer from electronic losses.[169]

4.2.3 Interactions between intersubband transitions and 2D polaritons

Recently, the interaction between graphene plasmons and intersubband transitions in III-V semiconductors has been described theoretically (Figure 4.5a).[232] The most striking effect of this interaction is the emergence of a non-locality: The intersubband transition energies and line shape show a pronounced dependence on the graphene plasmon momentum. Due to the tunability of the plasmon momentum by electrostatic doping, both the intersubband linewidth and transition energy can be tuned in situ. In this section, we review this theoretical description and discuss possible effects that we expect to find in our experiments using intersubband transitions in TMD quantum wells.

Emergence of parity-forbidden transitions

In the most common description of optical transitions, the photon is assumed to carry negligible momentum $q = \frac{2\pi}{\lambda_0}$ and we can use the dipole approximation $e^{i\mathbf{qr}} \approx 1$. This is justified for free space photons with wavelength λ_0. However, due to their large confinement, polaritonic excitations can carry significant momentum, leading to the breakdown of the dipole approximation. The transition energy from the first to the second subband then becomes dependent on the plasmon momentum $E_{12}(k_{\text{pl}})$. The transition rate derived from Fermi's Golden Rule (see also Equation 1.10) can then be approximated as

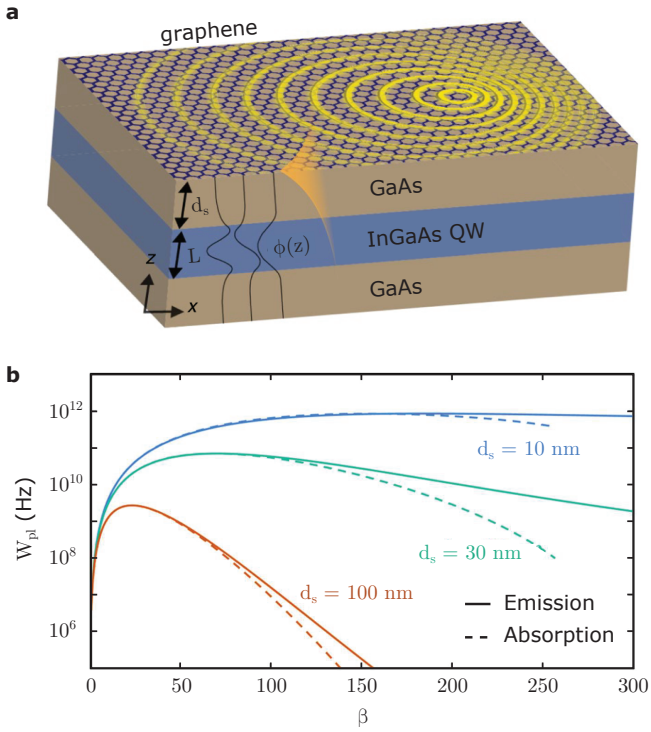

Figure 4.5: **Interaction of intersubband transitions and polaritons in 2D materials. a**, Schematics of the coupling between graphene plasmons and intersubband transitions in InGaAs quantum wells with wave functions $\Phi(z)$. The decaying out-of-plane electric field of the plasmon is depicted in orange. The quantum wells and graphene plasmons are separated by a spacing layer with thickness d_s. **b**, Calculated transition rates for plasmon-mediated intersubband transitions with different spacer thicknesses d_s. Adapted from ref. 232.

$$W_{\mathrm{pl}} \propto |\langle \phi_f | \, \mathrm{e}^{-k_{\mathrm{pl}} z} \partial_z \, | \phi_i \rangle|^2 \, \langle \boldsymbol{k}_{\perp,n_f} | \, \mathrm{e}^{\pm i \boldsymbol{k}_{\mathrm{pl}} \boldsymbol{r}_\perp} \, | \boldsymbol{k}_{\perp,n_i} \rangle \, . \tag{4.17}$$

The first term represents the interaction between the evanescent tail of the plasmon electric field and the intersubband transition inside the quantum well (the derivative stems from the momentum operator in z direction). The second term ensures in-plane momentum conservation. For the case of loss-less plasmons, this reduces to a delta function. Considering plasmon losses as well, this term becomes a Lorentzian function and leads to a broadening of the observed intersubband linewidth.

The modified transition matrix elements has a further consequence: The parity selection rule does not apply any more, and transitions that cannot be excited by free space photons can be excited when mediated by a plasmon. In fact, the plasmon-mediated transition $1 \rightarrow 3$ is stronger than the transition $1 \rightarrow 2$ for a large range of plasmon confinement factors β.

Blueshift and broadening

The extra momentum carried by graphene plasmons leads to a blueshift in the absorption energies of intersubband transitions. We now estimate this non-local blueshift for TMD quantum wells. For absorption from the bottom of the first subband to higher-momentum states of the second subband, we can calculate the blueshift from the parabolic dispersion relation of the second subband as $E_{\text{non-local}} = \frac{\hbar^2 k_{\text{pl}}^2}{2m_2}$, where m_2 is the effective mass of the second subband. For holes in a few-layer WSe_2 crystal we have $m_2 \approx m_0$ and we find $E_{\text{non-local}} \approx 0.13$ meV, where we assumed a plasmon confinement factor $\beta = 100$ for $\lambda_0 = 10.6$ µm. This shift is therefore negligible in our experiments. We note, however, that it can become important for experiments in III-V semiconductors due to the charge carriers' lower effective masses.

At finite temperatures there is an additional contribution to the broadening of intersubband transitions, apart from the previously discussed broadening due to the losses within the graphene plasmons: By absorbing a plasmon, thermally excited carriers in the first subband can be excited non-vertically to the bottom of the second subband, leading to smaller transition energies than one would obtain for vertical transitions. In the same way, thermally excited carriers can be excited to higher energy states in the second subband, leading to a tail towards higher energies. This is another manifestation of the non-locality induced by the plasmon-mediated transitions, leading to a broadening of the observed intersubband resonances. We have observed a similar effect when exciting intersubband transitions with the s-SNOM, where the sharp AFM tip provided the necessary momentum to allow for non-vertical transitions (Figure 3.7).

Dependence on the spacer thickness d_s

It is evident that the interaction between intersubband transitions and graphene plasmons depends strongly on their separation d_s. The electric field of the plasmons is decaying exponentially in the out-of-plane direction with a decay length of $1/k_{\text{pl}}$. This dependence also becomes evident from Equation 4.17 with the term $\mathrm{e}^{-k_{\text{pl}}z}$ in the transition matrix element. Figure 4.5b illustrates the impact of d_s on the transition rate of intersubband transitions. It is clearly desirable to reduce d_s as much as possible. Here, 2D materials hold a great potential, as dielectric spacer layers can be designed arbitrarily thin, up to the limit of a single atomic layer. In the following section, we investigate the dependence of the coupling on d_s in more detail. A suitable and readily available dielectric spacer is hBN, which we will use in our experiments. It is even possible to completely neglect the spacer layer, however it remains to be seen how the close proximity of graphene to the quantum well modifies its energy states.

4.2.4 The transfer matrix method

In order to calculate the dispersion relation of polaritons in 2D materials we use the transfer matrix method (TMM). The code for the TMM was implemented by Mark Lundeberg at ICFO.[233] The TMM is ideally suited to calculate the propagation of light through media with varying but piecewise constant refractive indices in the out-of-plane direction, as is the case

for layered van der Waals heterostructures.[234] We allow each layer within the heterostructure to be birefringent but assume it to be isotropic in the two in-plane dimensions. This is the case for most 2D materials with a few exceptions like for example black phosphorous.[98,235,236] In our implementation of the TMM we assume the boundary conditions at the bottom of the heterostructure to be given as an out-of-plane decaying evanescent wave. This implies that all incoming light is completely absorbed or reflected within the heterostructure and there is no transmission. Starting from this evanescently decaying electric field at the bottom of the heterostructure, the electric field at the top of the same layer can be calculated by a single matrix multiplication. This process can be continued until reaching the incoming electric field at the top of the heterostructure. Plasmon or phonon polariton resonances can be identified by a vanishing electric field at the top of the heterostructure. This indicates the existence of a self-sustained propagating mode within the heterostructure. By performing parameter sweeps over the light frequency and in-plane momenta, we obtain the complete dispersion relation of these plasmon or phonon polaritons. The necessary permittivity values for hBN were extracted by fitting the experimental data in ref. 226 and the conductivity of graphene is calculated by using the non-local random phase approximation.

We now use the TMM to simulate the coupling between intersubband transitions in TMDs and graphene plasmons. For this we consider the van der Waals heterostructure as illustrated in Figure 4.6a. It consists of hBN-encapsulated graphene, placed on top of a $N = 5$ TMD crystal, which is placed on a Si/SiO_2 substrate. The top hBN needs to be thin enough to allow for plasmon excitation by the AFM tip of the s-SNOM. Typical experimental values are around 5 nm, which we used for our simulations. The bottom hBN acts as a spacer layer between the TMD intersubband transitions and graphene plasmons. It needs to be as thin as possible in order to allow for a strong coupling while at the same time hindering the charge carriers from tunneling out of the quantum well. We chose $d_s = 2$ nm for these simulations, however detailed calculations are needed how the close proximity of graphene affects the quantum well energy states. We also note that such a thin spacer layer poses huge challenges in fabrication, both for finding suitable flakes as well as during the transfer process. For the TMD permittivity, we took the mid-infrared values given in ref. 237, which we assume to be representative for most TMDs. We chose $N = 5$ since we observed intersubband absorption at this thickness at $E_{\text{ph}} = 117$ meV, the photon energy of our CO_2 laser. The entire van der Waals heterostructure is placed on top of Si/SiO_2 substrate, which we can use to dope the TMD. Additionally, we can apply a voltage between the TMD and graphene doping both materials.

We first simulated the graphene plasmon dispersion relation in the absence of intersubband transitions. The obtained result for a graphene charge carrier density $n_{\text{gr}} = 5\text{x}10^{12}$ cm^{-2} and a scattering time $\tau = 1$ ps is shown in Figure 4.6b. We can observe a single plasmon branch with a plasmon wavelength $\lambda_{\text{pl}} \approx 86$ nm at $E_{\text{ph}} = 117$ meV. We do not observe the typical square root dispersion relation since we are looking at the upper polariton branch of an anticrossing of the graphene plasmon with the hBN phonon in the lower reststrahlen band. We now simulated the effect of an intersubband transition on this dispersion relation. In order to account for the intersubband transition, we added a complex Lorentzian function to the out-of-plane part of the TMD permittivity, centered at $E_{\text{ph}} = 117$ meV. For the strength of the intersubband transition we used the experimentally measured permittivity values. However, we

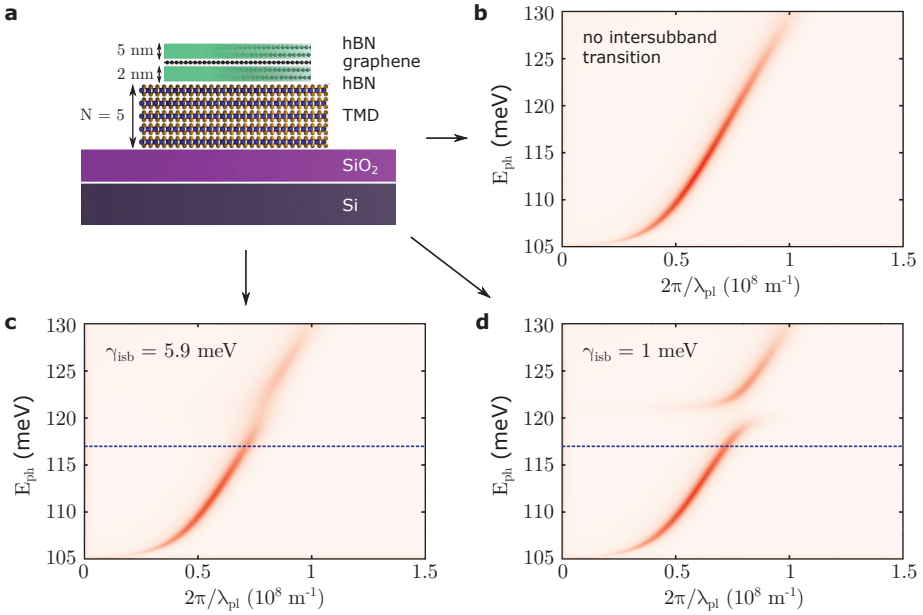

Figure 4.6: **Graphene plasmon dispersion relation on a SiO_2 substrate.** **a**, Schematic illustration of the van der Waals heterostructure used for the TMM simulations in **b** – **d**. **b**, Simulated graphene plasmon dispersion relation without the incorporation of intersubband transitions in the TMD. The used parameters for graphene are a scattering time $\tau = 1$ ps and sheet carrier density $n_{2D} = 5\text{x}10^{12}$ cm^{-2}. **c**, Same simulation as in **b** with an additional complex Lorentzian resonance in the out-of-plane permittivity of the TMD that accounts for the intersubband transition. We centered the resonance at $E_{ph} = 117$ meV (blue dashed line) and used the permittivity values that we expect from the measured values in Chapter 3. However, we assumed a linewidth of $\gamma_{isb} = 5.9$ meV and a quantum well carrier density $n_{2D} = 10^{13}$ cm^{-2}. **d** Same simulation as in **c** with $\gamma_{isb} = 1$ meV.

assumed the linewidth not to be broadened by the AFM tip but took it to be the theoretically calculated value $\gamma_{isb} = 5.9$ meV at room temperature. Finally, we also assumed a sheet carrier density $n_{2D} = 1\text{x}10^{13}$ cm^{-2}, which can experimentally be obtained by using a backgate and topgate doping with high quality dielectric materials. The resulting graphene plasmon dispersion relation is shown in Figure 4.6c. We observe a weaker plasmon branch above $E_{ph} = 117$ meV, which corresponds to larger plasmonic losses due to the additional decay channel into intersubband transitions. However, we are not yet in the strong coupling regime and no clear signature of an anticrossing can be observed.

We now investigated the effect of γ_{isb} on the coupling between intersubband transitions and graphene plasmons. For this, we performed the same TMM simulations with a smaller linewidth $\gamma_{isb} = 1$ meV. In an experiment, this can be achieved at low temperatures, as the calculated phonon-limited linewidth at $T \approx 0$ K is $\gamma_{isb} = 0.66$ meV (see section 1.4.4). The resulting plasmon dispersion relation is shown in Figure 4.6d. We observe a clear anti-crossing behavior, indicating that we are now in the strong coupling regime. The anticrossing occurs at around 120 meV, which is slightly higher than the intersubband resonance at 117 meV. We confirmed this peculiar behavior by two independent TMM simulations, implemented

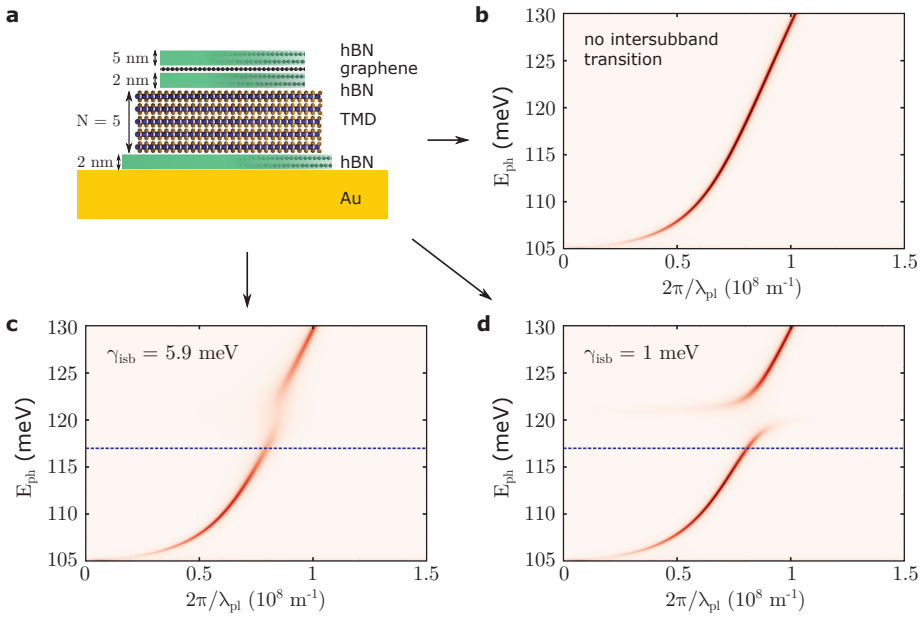

Figure 4.7: **Graphene plasmon dispersion relation on an Au substrate.** **a**, Schematic illustration of the van der Waals heterostructure used for the TMM simulations in **b** – **d**. In order to preserve the quantum well property of the TMD we inserted an additional hBN spacer layer in between the TMD and Au. **b**, **c**, **d** Simulated graphene plasmon dispersion relations with the same paramters as in Figure 4.6 but with Au instead of SiO_2 as the substrate material.

in both Python and Matlab. The origin of this blue-shift of the anticrossing is still under investigation.

In the next simulations, we replaced the Si/SiO_2 substrate by Au. This leads to the formation of acoustic plasmons where the electric field is almost entirely confined between the graphene and Au substrate.[238] In order to preserve the quantum well properties of the TMD, we added an additional hBN spacer layer between the TMD and Au, as is illustrated in Figure 4.7a. When we simulate the graphene plasmon dispersion relation without the incorporation of intersubband transitions (Figure 4.7b), we notice that the Au substrate leads to a sharper plasmon branch. This acoustic plasmon mode also carries a larger momentum than graphene plasmons, with a wavelength $\lambda_{pl} \approx 78$ nm at $E_{ph} = 117$ meV. In a next step, we included the intersubband transition into the TMM simulations. We first assumed $\gamma_{isb} = 5.9$ meV (Figure 4.7c). Similar as for the simulations on the SiO_2 substrate, this leads to a damping of the graphene plasmons at slightly larger energies than the center of the intersubband transition, which remained unchanged at $E_{ph} = 117$ meV. In comparison to the SiO_2 substrate, however, this damping is now stronger pronounced. After reducing the intersubband linewidth to $\gamma_{isb} = 1$ meV (Figure 4.7d) we again enter into the strong coupling regime, with a clear formation of an upper and lower polariton branch. This anticrossing is more distinctively developed than on the SiO_2 substrate.

In order to investigate the role of the substrate in more detail, we compared the Rabi splitting

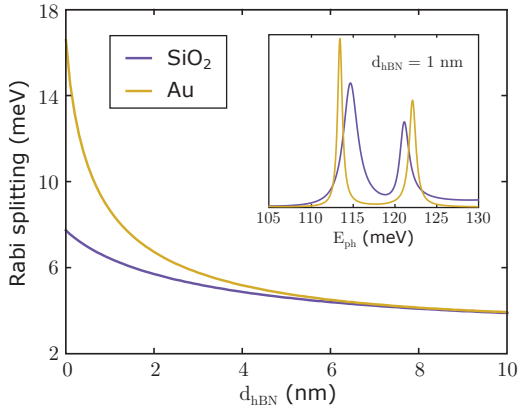

Figure 4.8: **Simulated Rabi splitting for different thicknesses of the hBN spacer layers.** Extracted Rabi splitting for varying d_{hBN} on Au and SiO_2 substrates. In the case of the Au substrate we vary both hBN spacer layers simultaneously. The inset shows the two polariton branches at fixed momentum $2\pi/\lambda_{\mathrm{pl}}$.

on an Au substrate with the one a Si/SiO_2 substrate for varying hBN thicknesses d_{hBN}. We chose $\gamma_{\mathrm{isb}} = 1$ meV in order to observe a clear anticrossing for all simulated hBN thicknesses. In the case of the Au substrate, there are two hBN layers that are important: The spacer between the quantum well and the overlying graphene, as well as the spacer to the underlying Au substrate. In Figure 4.8, we varied both of these spacer layers simultaneously. We observe that we obtain a much larger Rabi splitting on the Au substrate for thin spacer layers. We can explain this large increase of the Rabi splitting by the huge field confinement associated with the formation of acoustic plasmons. According to Equation 4.6, the Rabi splitting $2\hbar g_0$ is proportional to $V^{-1/2}$. For the case of the Au substrate, the mode volume V is given as $V \approx \lambda_{\mathrm{pl}}^2 L$, where L is the distance between graphene and Au. In order to calculate V, we simulated λ_{pl} at $E_{\mathrm{ph}} = 117$ meV without the incorporation of intersubband transitions.

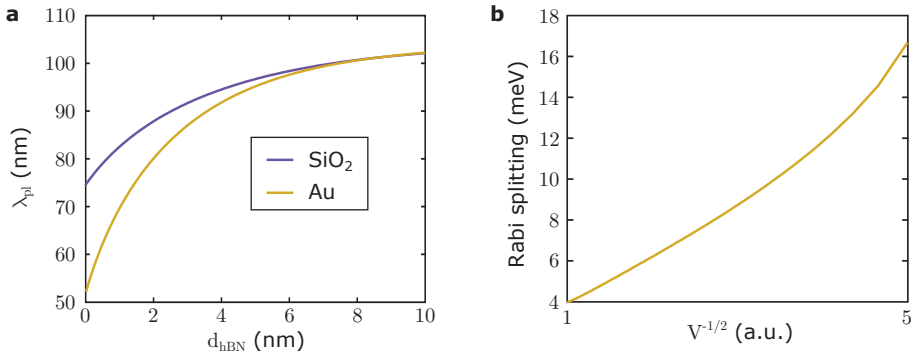

Figure 4.9: **Dependence of the Rabi splitting on the mode volume.** **a**, Simulated λ_{pl} as a function of d_{hBN} for $E_{\mathrm{ph}} = 117$ meV on Au and SiO_2 substrates. **b**, The extracted Rabi splitting on the Au substrate as a function of the mode volume $V \approx \lambda_{\mathrm{pl}}^2 L$, where L is the distance between graphene and Au.

These simulations are shown in Figure 4.9a. We observe that λ_{pl} significantly decreases for thin spacer layers. For comparison, we also show λ_{pl} on the Si/SiO_2 substrate and confirm that the acoustic plasmons carry a considerably larger momentum, especially for thin spacer layers. We can now express the observed Rabi splitting as a function of the mode volume V of the acoustic plasmons (Figure 4.9b). We observe a linear increase of the Rabi splitting with $V^{-1/2}$ over a large range of V, which is expected from Equation 4.6. The deviation from the linear dependence for small V might be due to the blue-shift of the anticrossing with respect to the intersubband resonance energy and is still under investigation.

4.2.5 FDTD simulations

Acoustic plasmons give rise to a wide variety of device geometries that can be exploited for an efficient coupling of the plasmons to intersubband transitions. To study these possibilities, we performed finite difference time domain (FDTD) simulations using the commercially available software Lumerical. In a first simulation, a plane wave ($E_{\mathrm{ph}} = 115$ meV) is incident on a hBN/graphene/hBN heterostructure, placed on top of an Au grating. The width of each Au rod is chosen to be 140 nm and the spacing between the rods is 60 nm. Both hBN layers have a thickness of 1 nm. Figure 4.10 shows the simulation results, in which the color map illustrates the magnitude of the out-of-plane electric field E_y. We observe that almost the entire electric field is confined in the distance of 1 nm between the graphene and Au, forming acoustic plasmons associated with a large enhancement of the electric field. This is therefore a powerful way to couple far-field light to the out-of-plane intersubband transitions and can be exploited for far-field measurements of intersubband absorption or strong coupling experiments between plasmons and intersubband transitions.

In a second simulation, we considered a single Au rod and placed a broadband, out-of-plane dipole emitter in the middle of a 2 nm vacuum gap between the Au rod and an infinitely large graphene sheet. A schematic of the simulated structure is shown in Figure 4.11a. In this simulation, the dipole emitter could represent an intersubband transition and we simulated the out-of-plane electric field profile after the emission from the dipole (Figure 4.11b). We can observe the formation of cavity-like field modes in the area between the Au rod and the graphene sheet. The out-of-plane dipole excites acoustic plasmons between graphene and Au,

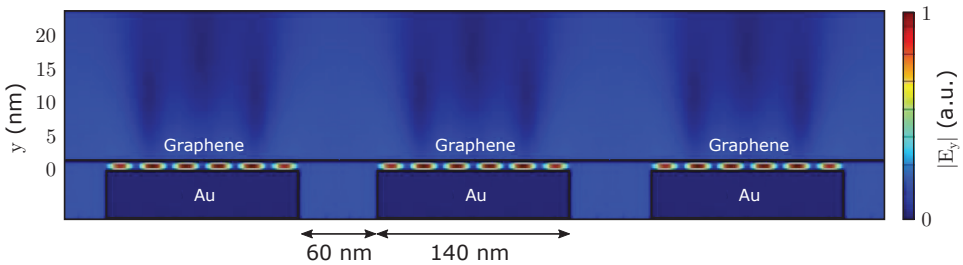

Figure 4.10: **Acoustic plasmons excited by a plane wave.** FDTD simulations of a plane wave with $E_{\mathrm{ph}} = 115$ meV incoming from the top onto an Au grating. A continuous graphene sheet is placed above the grating, separated by a 1 nm thick hBN spacer layer. The color plot illustrates the magnitude of the out-of-plane electric field E_y.

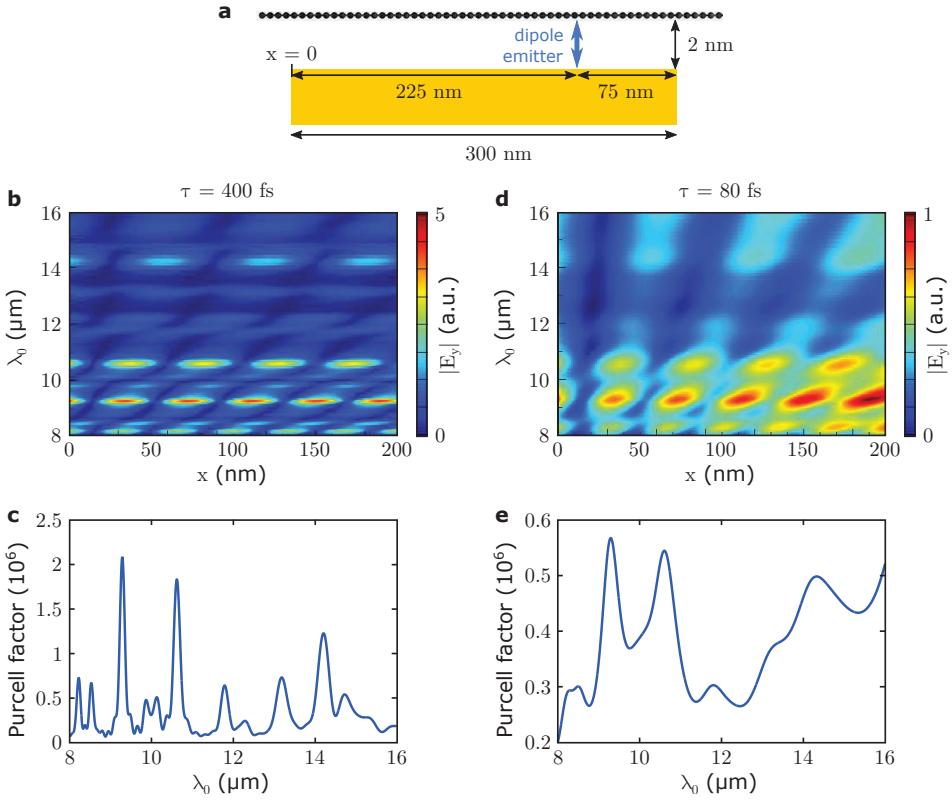

Figure 4.11: **Acoustic plasmons excited by a broadband dipole emitter.** **a**, Schematic of the simulated device structure. A broadband out-of-plane dipole emitter is placed in the middle of a 2 nm vacuum gap between an Au rod and an infinitely large graphene sheet. The Au rod has a width of 300 nm and the dipole is placed at 75 nm from its right edge. **b**, **c**, Simulated absolute value of the out-of-plane electric field E_y after the emission of the dipole (**b**) and the corresponding Purcell factors of the dipole (**c**). The scattering time τ of graphene was set to 400 fs. **d**, **e**, Same simulations as in **b** and **c** but with $\tau = 80$ fs.

which travel towards the edge of the Au rod. Beyond the edge of the Au rod only regular graphene plasmons are supported. However, there is a large momentum mismatch between acoustic plasmons and graphene plasmons (see Figure 4.9a), which has the consequence that acoustic plasmons are reflected at the Au edge, leading to the formation of a standing wave. The emission into acoustic plasmons leads to huge Purcell factors $>10^6$ whose wavelength dependence follows the cavity resonance conditions (Figure 4.11c). We note that the quality of graphene is very important for the formation of distinctive cavity modes. In Figure 4.11d we performed the same simulation with a graphene scattering time $\tau = 80$ fs (instead of $\tau = 400$ fs for the previous simulation), which leads to smeared out cavity modes and correspondingly lower Purcell factors. In a recent study[239] a similar device geometry has been analyzed analytically and even higher Purcell factors were predicted. These numbers are very promising for the efficient out-coupling of photons emitted from intersubband transitions or for the efficient launching of graphene plasmons via intersubband transitions by driving an electrical current through the quantum well.

4.3 Experimental results

4.3.1 Graphene plasmons and intersubband transitions

We now turn towards the experimental observation of an interaction between graphene plasmons and intersubband transitions in 2D materials. In these experiments, we excite and measure plasmons in graphene using the s-SNOM. As described in section 4.2.1, the s-SNOM allows us to spatially observe graphene plasmons and measure their wavelength and decay length. According to Figure 4.6, we expect the interaction between the plasmons and the intersubband transitions to manifest itself in either a change in the plasmon wavelength λ_{pl} or as an additional damping channel for the plasmons, leading to a shorter decay length.

We first measured several devices as schematically shown in Figure 4.12. They consist of a terraced WSe_2 flake that we placed on top of hBN-encapsulated graphene by using the dry-transfer technique as described in section 2.1.2. In this device geometry, the upper hBN acts as the spacer layer between the WSe_2 quantum well and the graphene layer. For our devices we typically have $d_s \approx$ 4–7 nm. An optical microscope image of a typical device is shown in Figure 4.13a. We fabricated and measured three devices similar to the one shown, all of which yielded qualitatively similar results.

We first performed a spatial scan over our device at $E_{\mathrm{ph}} = 117$ meV while applying $V_{\mathrm{BG}} =$ -40 V (Figure 4.13b). Different thicknesses of WSe_2 can be distinguished in the magnitude of the optical signal $|s_3|$. Additionally, graphene shows a strong optical contrast and can be clearly distinguished in the scan, even when it is probed through the overlying WSe_2 and hBN layers. This is due to the finite extension of the near-field around the AFM tip, extending a few 10s of nm into the underlying materials.[156] The strong optical contrast of graphene stems from the free charge carriers induced by the applied $V_{\mathrm{BG}} =$ -40 V and can be tuned by varying V_{BG}.

Next, we characterized graphene plasmons in a region of the device that only contains hBN-encapsulated graphene, without any WSe_2 on top. This leads to a better signal since the tip is in closer proximity to graphene and can therefore more efficiently launch and detect

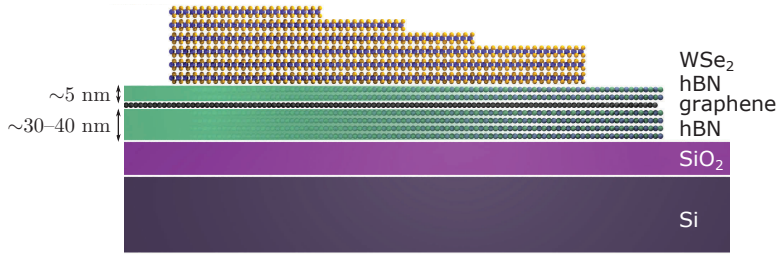

Figure 4.12: **Schematic of the first device geometry used to study the interaction between graphene plasmons and intersubband transitions.** In a first design, we placed a WSe_2 staircase flake on top of hBN-encapsulated graphene. Plasmons are excited through the WSe_2 by the illuminated AFM tip.

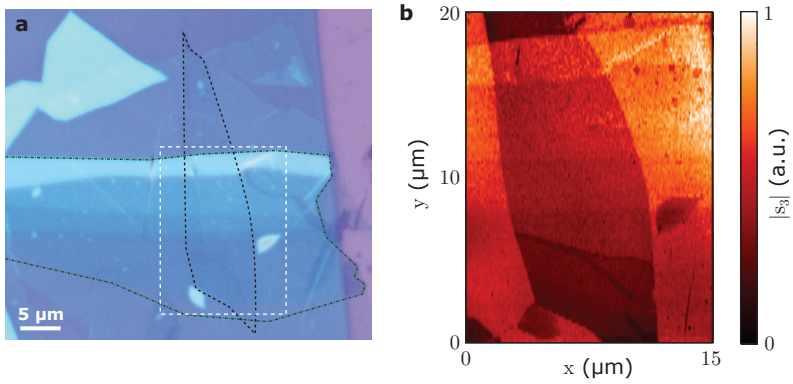

Figure 4.13: **Optical microscope and s-SNOM images of WSe_2 on hBN-encapsulated graphene.** **a**, Optical microscope image of a van der Waals heterostructure consisting of a terraced WSe_2 flake transferred on top of hBN-encapsulated graphene. Graphene is outlined in black dashed lines. It is not visible through the hBN. The WSe_2 is outlined in green dash-dotted lines. **b**, s-SNOM scan in the area indicated by the white dashed lines in **a**. Different thicknesses of the WSe_2 crystal can be distinguished by different optical contrasts. The underlying graphene can be identified by its low optical signal, which is due to the presence of charge carriers induced by the applied V_{BG} = -40 V. The illumination photon energy was E_{ph} = 117 meV.

the graphene plasmons. The optical signal $\mathrm{Re}(s_3)$ of a line scan at E_{ph} = 117 meV and V_{BG} = 80 V close to the graphene edge is shown in Figure 4.14a. We can clearly observe several oscillations in the scan, which we attribute to the graphene plasmons launched by the AFM tip and the graphene edge. The oscillations due to graphene plasmons become even more evident when plotting $\mathrm{Re}(s_3)\sqrt{x}$, as we demonstrate in Figure 4.14b. We fit the observed signal by using the equation $\xi_{opt}(x) = \xi_{bulk}(x) + A\frac{e^{i2q_{pl}x}}{\sqrt{x}} + B\frac{e^{iq_{pl}x}}{x}$, as described in Equation 4.13. We observe a decay length $\gamma^{-1} = \frac{\mathrm{Re}(q_{pl})}{\mathrm{Im}(q_{pl})} = 22$, which is comparable to some of the highest quality graphene plasmons reported at room temperature.[49] We note, however, that the extracted γ^{-1} is extremely sensitive to the subtracted background $\xi_{bulk}(x)$ and the $x = 0$ position that represents the position of the graphene edge. Regardless of the exact value of γ^{-1}, however, this measurement confirms that we fabricated high quality graphene devices where plasmons show a long propagation length. The extracted plasmon wavelength λ_{pl} = 116 nm corresponds to a confinement factor $\beta \approx 90$. We can tune λ_{pl} by varying V_{BG} – and therefore E_F in graphene – according to Equation 4.8. This tunability is demonstrated in Figure 4.14c. Here, we repeatedly scanned the same line, varying V_{BG} in steps of 2.5 V for each line. From the line scans, we can deduce that the charge neutrality point of graphene is located at around V_{BG} = 45 V, which indicates a strong intrinsic hole doping. We observe λ_{pl} to decrease when approaching the charge neutrality point, which is in agreement with the dispersion relation derived from the Drude model (Equation 4.11).

As a next step towards the observation of interactions between plasmons and intersubband transitions, we excite graphene plasmons through the overlying WSe_2. This is not trivial, as the tip-graphene distance is increased significantly, lowering the observed optical signal of the graphene. Figure 4.15a shows the excitation of graphene plasmons through WSe_2 with

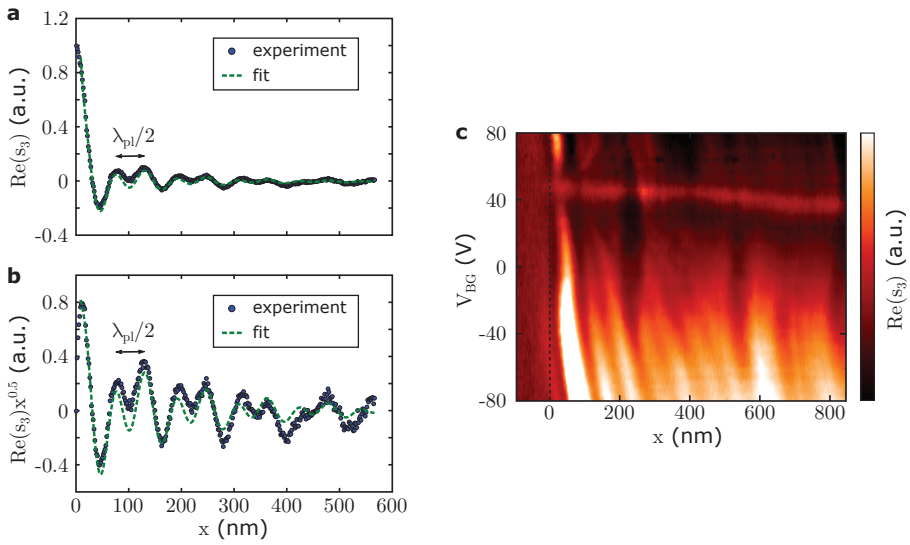

Figure 4.14: **Characterization of graphene plasmons.** **a**, **b**, Real part of the measured optical signal $\mathrm{Re}(s_3)$ at E_{ph} = 117 meV and V_{BG} = 80 V along a graphene edge, showing graphene plasmons. Both **a** and **b** show the same experimental data, where in **b** the data was multiplied by $\sqrt{x}$ in order to emphasize the plasmons oscillations. The distance between two fringes is $\lambda_{pl}/2$ due to the interference between plasmons propagating away and towards the AFM tip apex. The green dashed line is the fit with Equation 4.13, which also takes into account plasmons that are launched at the graphene edge. We observe λ_{pl} = 116 nm, $\beta \approx 90$ and $\gamma^{-1} \approx 22$. **c**, Graphene plasmons observed in $\mathrm{Re}(s_3)$ for various V_{BG}. We can observe the tunability of graphene plasmons by changing V_{BG}. The black dashed line indicates the position of the graphene edge. On this device, the charge neutrality point of graphene is located at around V_{BG} = 45 V, which indicates a strong intrinsic hole doping.

different layer numbers up to $N = 8$. We can see that we still observe plasmon oscillations, even though the detected optical signal is not as good as when we directly excited the plasmons without the overlying WSe_2.

Finally, in order to observe any interaction of the graphene plasmons with the intersubband transitions, we need to p-dope the WSe_2 flake. To do so, we applied an additional voltage between graphene and WSe_2 that we call V_{gr}. Here, $V_{gr} < 0$ induces p-doping within WSe_2 and $V_{gr} > 0$ induces electrons in WSe_2, while opposite charges are induced in graphene. Figures 4.15a and b show the observed plasmons at E_{ph} = 117 meV for V_{gr} = 0 V and V_{gr} = -1.5 V, respectively. This corresponds to charge-neutral (V_{gr} = 0 V) and p-doped WSe_2 (V_{gr} = -1.5 V). Additionally, we applied a global V_{BG} that strongly electron doped the graphene in order to observe plasmons. We performed a spatial scan over an area of the WSe_2 flake with N = 1, 4, 5, 8. In none of these thicknesses we could observe any significant differences in the plasmon wavelength or decay length between when the WSe_2 is charge neutral and p-doped. We could hence not observe any interaction between graphene plasmons and intersubband transitions in WSe_2. This is also true when we modulated V_{gr}, either by applying a different voltage for each adjacent line or by varying the voltage every few pixels, as we described in section 2.2.4.

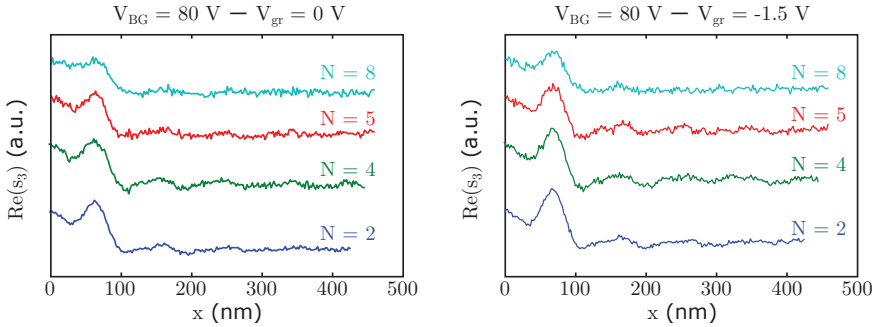

Figure 4.15: **Excitation of graphene plasmons through WSe_2.** **a**, Graphene plasmons oscillations detected in the optical signal $\mathrm{Re}(s_3)$. The scan was performed at $E_{\mathrm{ph}} = 117$ meV over an area of the WSe_2 flake with varying layer numbers N. The applied $V_{\mathrm{BG}} = 80$ V strongly n-doped graphene. **b**, Same scan as in **a** with an additional voltage $V_{\mathrm{gr}} =$ -1.5 V applied, which hole dopes WSe_2 and thus allows for the occurrence of intersubband transitions. **a** and **b** were taken during a single scan, where we varied V_{gr} between each adjacent line.

There are several possible reasons that might be the cause why we did not observe any interaction between the graphene plasmons and intersubband transitions. First, it is difficult to excite plasmons through WSe_2, leading to a weaker signal and effectively a shorter observable decay length. Therefore, a small change in the decay length due to an interaction between the plasmons and intersubband transitions might not be observable in the measurements. It is also possible that the employed photon energy $E_{\mathrm{ph}} = 117$ meV is too far from the intersubband resonance expected at 105 meV, so that all possible changes in the plasmon wavelength and decay length become too small for us to observe. Also, we cannot confirm the presence of intersubband transitions inside the WSe_2 crystal at any time during the measurements. Before the fabrication of the heterostructure, we cannot measure the absorption due to intersubband transitions since this requires electrical contacts to dope the WSe_2 crystal. However, the definition of electrical contacts prevents the subsequent pick-up of the WSe_2 flake and therefore the fabrication of the heterostructure. Once the WSe_2 flake is placed on the encapsulated graphene layer, the observation of intersubband transitions proves to be difficult since the optical signal is dominated by the strong contrast of free carriers in graphene and an eventual absorption due to intersubband transitions remains hidden in the measurements. We have therefore no possibility to confirm the presence of intersubband transitions within the WSe_2 flake. Instead, we had to choose the flakes due to their optical contrast, identifying suitable flakes by their color. This method, however, becomes unreliable for $N > 4$ and it might be possible that we did not identify the resonant $N = 5$ area of the flake correctly for all devices. Furthermore, it is possible that the resonance energies shift due to the different dielectric environment experienced by the quantum wells due the hBN substrate and in particular the graphene layer underneath.

In order to overcome some of these challenges, we explored a second design geometry to investigate the interaction between graphene plasmons and intersubband transitions. In this second design geometry (Figure 4.16), we placed hBN-encapsulated graphene on top of the terraced WSe_2 flake. This has the advantage that before the transfer of graphene we can first measure the absorption due to intersubband transitions thereby confirming that the WSe_2 flake

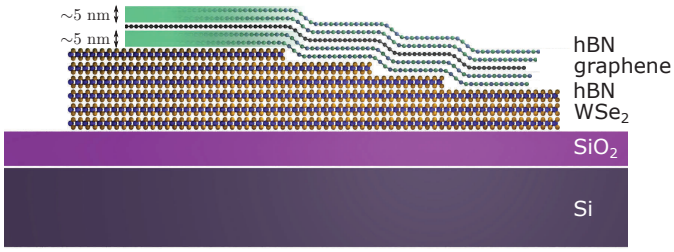

Figure 4.16: **Schematic of the second device geometry used to study the interaction between graphene plasmons and intersubband transitions.** In this design, we placed hBN-encapsulated graphene on top of a terraced WSe_2 flake. This has the advantage that we can first measure intersubband transitions in WSe_2 before proceeding with the transfer. The disadvantage of this geometry lies in its challenging fabrication and the contamination of the WSe_2/hBN interface due to the intermediate fabrication step needed to define electrical contacts to WSe_2.

contains an area with a thickness that is resonant with $E_{\text{ph}} = 117$ meV. An optical microscope image of a WSe_2 flake and the corresponding measurement of intersubband transitions is shown in Figures 4.17a and b. Only after the measurement of intersubband transitions we proceeded with the transfer of the hBN-encapsulated graphene flake using the same dry-transfer technique. The main disadvantage of this design geometry lies in the fact that we need to electrically contact WSe_2 in order to measure intersubband transitions, which involves an exposure to various chemicals and solvents. This in turn makes it harder to preserve the atomically smooth interfaces between WSe_2 and the bottom hBN, leading to the formation of several bubbles of contamination within the van der Waals heterostructure.

Also, it has to be noted that the fabrication of this design geometry is much more challenging than the previously discussed geometry. First, both hBN layers at the top and bottom need to be very thin – in our case both of them had a thickness of ~5 nm. The top hBN needs to be thin in order to efficiently excite plasmons by using the s-SNOM, while the bottom hBN now acts as the spacer layer between graphene and the WSe_2 quantum wells. As a result, the complete van der Waals heterostructure deposited on WSe_2 only has a thickness of ~10 nm and is therefore very brittle, easily introducing cracks in the hBN when depositing it. Furthermore, the complete stack has to be positioned with a precision of a few µm on top of the WSe_2 flake, ideally with the graphene edge extending over several areas of the WSe_2 flake with different N. This is challenging since thin hBN cannot be seen on a transparent substrate under the optical microscope, while single-layer graphene shows only a very faint contrast due to its low absorption of ~2.3%[18] in the visible spectral region.

Figure 4.17c shows an optical microscope image of a complete device, where we placed hBN-encapsulated graphene on top of a WSe_2 flake with areas of different layer numbers N. We fabricated three similar devices, where one of the broke during the final step of electrically contacting graphene, so that we could only take data from two devices. Figure 4.17d shows a spatial s-SNOM scan with dimensions 20x15 µm^2 over the area of the device where graphene was placed on top of WSe_2. The most prominent feature is the enhanced contrast of graphene only in the area where it overlaps the WSe_2. This might indicate that charge carriers are

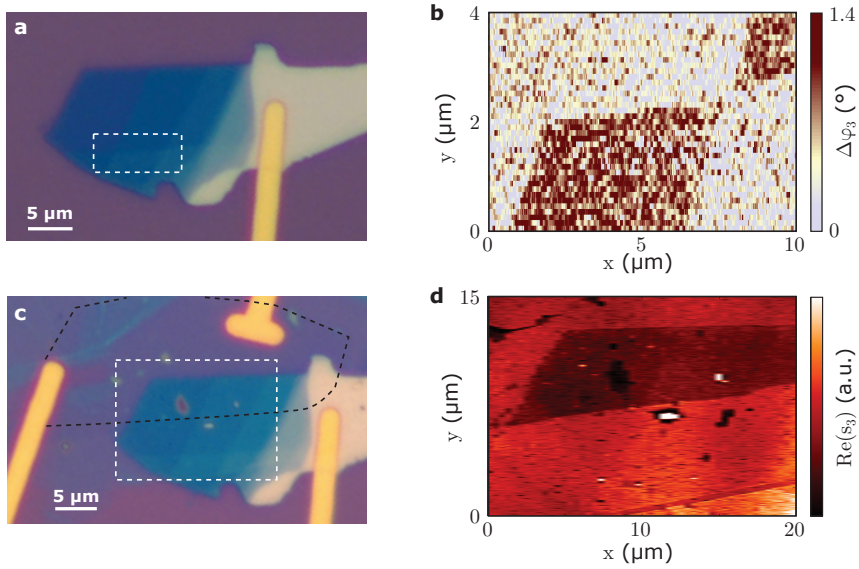

Figure 4.17: **Optical microscope and s-SNOM images of hBN-encapsulated graphene on top of WSe_2.** **a**, Optical microscope image of a contacted WSe_2 flake on a Si/SiO_2 substrate before transferring the hBN-encapsulated graphene. Different layer numbers N can be distinguished by their optical contrast. **b**, Spatial measurement of $\Delta\varphi_3$ at $E_{ph} = 117$ meV over the area indicated by the dashed lines in **a**. Enhanced absorption can be observed in areas with $N = 5$, which is due to intersubband transitions. V_{BG} was modulated between 0 and -50 V as described in section 2.2.4. **c**, Optical microscope image of a complete device, where we transferred hBN-encapsulated graphene on the WSe_2 flake shown in **a** and contacted it with two one-dimensional contacts made out of Ti/Au. Graphene is outlined by the black dashed lines. Each of the hBN layers has a thickness of ∼5 nm and can only be weakly seen in the microscope image. **d**, Spatial s-SNOM scan over the area indicated by the dashed lines in **c**. Graphene that is overlapping the WSe_2 flake shows a strong optical contrast, indicating a charge transfer between WSe_2 and graphene.

transferred between graphene and WSe_2, even though they are separated by a hBN spacer layer. We also observe that the different thicknesses of WSe_2 cannot be distinguished using the s-SNOM since they are buried underneath ∼10 nm of hBN. Additionally, we now cannot detect anymore the absorption due to intersubband transitions. This is no surprise since there is a relatively large distance between the AFM tip and the WSe_2 flake. However, this also does not let us confirm that intersubband transitions are still present even in the changed dielectric environment of hBN.

We now proceed with the measurement of graphene plasmons. In order to dope graphene, we apply a voltage V_{gr} between WSe_2 and the overlying graphene sheet. We characterized the effect of V_{gr} by taking a line scan along the edge of graphene and varying V_{gr} (Figure 4.18a). We observed the emergence of plasmons for both positive and negative V_{gr}, indicating that we can efficiently dope graphene. This also demonstrates that we are able to overcome the quantum capacitance of WSe_2 associated to its bandgap. We found graphene's charge neutrality point to be located at $V_{gr} \approx 0.4$ V, indicating a moderate intrinsic p-doping of

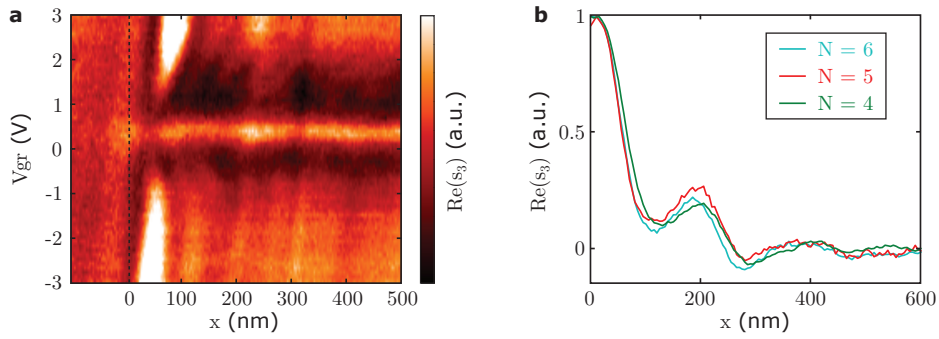

Figure 4.18: **Plasmons in hBN-encapsulated graphene on top of a staircase WSe_2 flake.** **a**, Emergence of plasmons in the optical signal $\mathrm{Re}(s_3)$ for positive and negative voltages V_{gr}, applied between WSe_2 and graphene. The graphene edge is located at $x = 0$ and we find the charge neutrality point to be located at $V_{gr} \approx 0.4$ V, indicating a moderate intrinsic p-doping. **b**, Measured plasmon oscillations for different layer numbers N. We doped the graphene sheet by applying $V_{gr} = 7$ V, which at the same time p-doped the underlying WSe_2 flake, allowing for the occurrence of intersubband transitions.

graphene. The propagation length of the plasmons, however, is not as long as observed previously, which might be due to a combination of the contamination at the WSe_2/hBN interface and the thin bottom hBN, which might not be sufficiently thick to screen these detrimental effects.

Next, we compared the propagation of plasmons in different layer numbers N. For all devices we had previously confirmed the existence of intersubband transitions in layer numbers $N = 5$. We can therefore be sure to compare the propagation of plasmons in proximity of an intersubband transition with the propagation of plasmons without a resonant quantum well nearby. Figure 4.18b shows this graphene plasmon propagation on different areas of the WSe_2 flake with layer numbers $N = 4$, 5, 6. We applied $V_{gr} = 7$ V (the highest voltage we could reach before the breakdown of the hBN spacer layer), which induces electrons within graphene and at the same time strongly p-doped WSe_2. We observed several plasmon fringes in all measured N. However, we could not measure a significant difference between different layer numbers, indicating that we did not observe any interaction between the graphene plasmons and WSe_2 quantum wells.

Similar as for the first device geometry, there are two main possible explanations why we could not observe any interaction between graphene plasmons and WSe_2 quantum wells. First, it is possible that the change in plasmon wavelength or the reduction in propagation length that we expect to appear due to the interaction between graphene plasmons and WSe_2 quantum wells is not large enough to be observed in our experiments. In this particular device geometry we have the additional difficulty that the intrinsic plasmon losses in graphene are already large due to the additional fabrication steps needed to measure intersubband transitions, which includes the use of chemicals and liquid solvents. Here, the use of 'AFM brooming'[240] might be a promising approach, where an AFM tip in contact-mode operation is used to remove any contaminating residues from 2D materials. This additional fabrication step can be employed after the measurement of the intersubband transitions in WSe_2 in order to restore

its atomically flat surface, which might lead to a larger graphene plasmons propagation length. An alternative explanation why we cannot observe any kind of interaction might be that the intersubband transition energies are modified by the dielectric environment of hBN and the close proximity of graphene. This might lead to a situation where none of the probed N is resonant with the utilized E_{ph}.

4.3.2 hBN hyperbolic phonon polaritons and intersubband transitions

In the following experiment, we aim to observe interactions between intersubband transitions in WSe_2 and hyperbolic phonon polaritons in the upper reststrahlen band of hBN. This is a very similar system as the previously considered coupling between graphene plasmons and intersubband transitions. Therefore, the experimental signatures of a coupling are the same, namely a reduced propagation length of the phonon polaritons or a change of their wavelength λ_{ph}. In order to experimentally observe the coupling, we placed a thick hBN flake directly on top of a WSe_2 flake with different layer numbers N (Figure 4.19). The hBN flake is therefore in direct contact with WSe_2, leading to a vanishing thickness of the spacing layer ($d_s \to 0$). The fabrication of these devices is easy compared to the previously discussed geometries since only one transfer step of the hBN flake is needed. Furthermore, this hBN flake is rather thick (∼40–200 nm), facilitating the transfer even more. We fabricated three devices of this geometry, two of them on a SiO_2 substrate and one of them on HfO_2. All of the devices showed qualitatively similar results. An optical microscope image of a complete device is shown in Figure 4.20a.

For the experiments, we exploited the intersubband transition in the $N = 4$ area of the WSe_2 flake, which is centered at ∼168 meV (measured on a HfO_2 substrate – see Chapter 3). This is slightly below the upper reststrahlen band of hBN, which is located at ∼169–201 meV. However, the finite width of the intersubband transitions should lead to an overlap of the tail of the transition with the upper reststrahlen band. The blueshift in the intersubband absorption when the transition is mediated by phonon polaritons can be neglected in our experiments, due to the large effective in-plane masses in WSe_2 and the small phonon polariton confinement compared to graphene plasmons. Similar as in the previous measurements, we first confirmed the presence of the intersubband transitions on all measured devices by s-

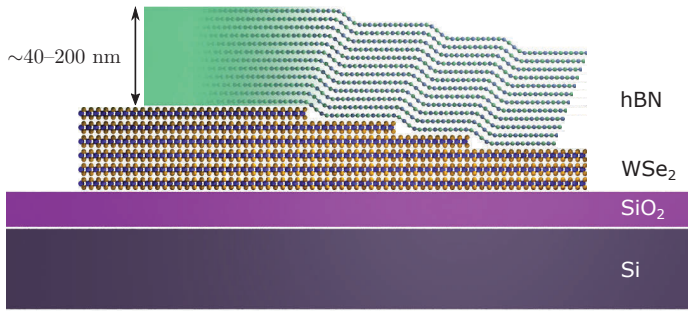

Figure 4.19: **Schematic of the device geometry used to study the interaction between hBN hyperbolic phonon polaritons and intersubband transitions.**

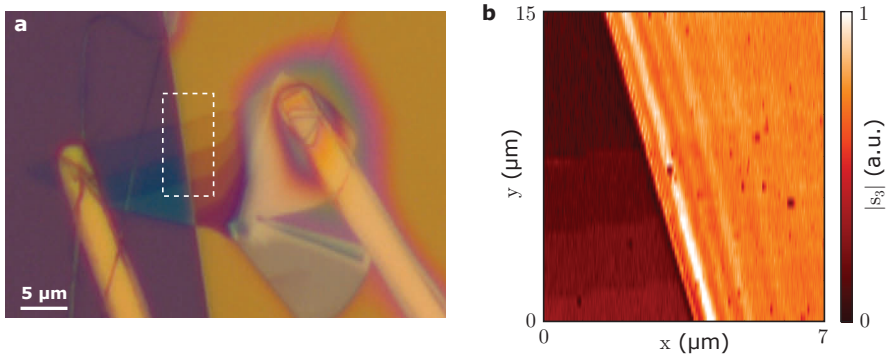

Figure 4.20: **Optical microscope and s-SNOM image of hBN on top of a terraced WSe_2 flake. a**, Optical microscope image of a terraced WSe_2 flake on top of a SiO_2 substrate. The yellow part on the right is the overlying hBN flake with a thickness $d = 95$ nm. **b**, Spatial s-SNOM scan in the area indicated by white dashed lines in **a**. Different thicknesses of WSe_2 in the left half of the scan and phonon polaritons along the hBN edge are readily visible in the optical signal $\mathrm{Re}(s_3)$. The scan was taken for $E_{\mathrm{ph}} = 186$ meV.

SNOM measurements, before we transferred the hBN flake on top by using the dry-transfer technique.

First, we characterized the hyperbolic phonon polaritons in hBN. The hyperbolic phonon polaritons are readily visible in the optical signal of the s-SNOM along the edge of the hBN flake when E_{ph} lies within the upper reststrahlen band (Figure 4.20b). The phonon polaritons are excited and detected by the sharp AFM tip, which provides the necessary momentum to couple to free space light. Furthermore, phonon polaritons can be excited at the hBN edge, similar as in the case of graphene plasmons. We can therefore model the observed fringe pattern in the same way as we did for graphene plasmons by using Equation 4.13. A typical

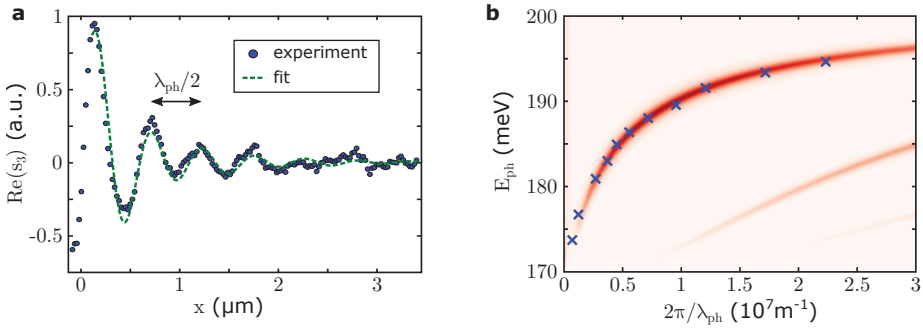

Figure 4.21: **Measured dispersion relation of hBN phonon polaritons. a**, s-SNOM line scan along the edge of a hBN flake with thickness $d = 95$ nm at $E_{\mathrm{ph}} = 186.4$ meV. Phonon polaritons are visible in $\mathrm{Re}(s_3)$ and the observed fringe pattern is fit by using Equation 4.13. **b**, Experimentally obtained dispersion relation (blue crosses) by repeating measurements as the one in **a** for different E_{ph}. The color plot represents the calculated dispersion relation by using the transfer matrix method as described in section 4.2.4.

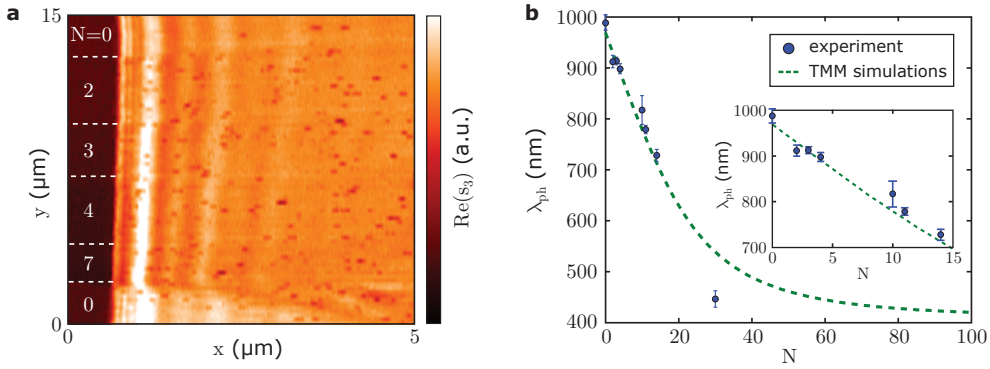

Figure 4.22: **Phonon polariton dependence on dielectric environment. a**, s-SNOM scan taken at $E_{\text{ph}} = 187.8$ meV along the edge of a hBN flake transferred on top of a WSe_2 flake with different thicknesses. The WSe_2 layer numbers N are marked in the figure. We observe a change in the phonon polariton wavelength for different N. **b**, Experimentally obtained phonon polariton wavelengths λ_{ph} for different N of the underlying WSe_2. The error bars represent the 95% confidence intervals to the fits. The scans were taken at $E_{\text{ph}} = 183.7$ meV on a WSe_2 flake with $d = 65$ nm. The green dashed line represents the simulated results using the transfer matrix method. The inset shows the same data over a smaller range of N.

line profile measured at $E_{\text{ph}} = 186.4$ meV is shown in Figure 4.21a. We see that we can accurately model the fringes observed in the optical signal. For this line profile, we obtained a polariton wavelength $\lambda_{\text{ph}} = 926$ nm, which corresponds to a confinement factor $\beta \approx 7$. According to Equation 4.15, β increases with decreasing hBN thickness, but at the same time it becomes experimentally more difficult to observe the polariton fringes.

Next, we measured the dispersion relation of hBN hyperpolic phonon polaritons. For this, we varied E_{ph} within the upper reststrahlen band. According to Equation 4.15 this leads to a change in the polariton wavelength due to the change in hBN permittivity. The experimentally obtained dispersion relation measured on a hBN crystal with thickness $d = 95$ nm is shown in Figure 4.21b. We theoretically modeled this dispersion relation by using the transfer matrix method as described in section 4.2.4 and find an excellent agreement between theory and experiment. This confirms both the validity of the transfer matrix method as well as the fit to the experimental data in order to extract λ_{ph}.

We noticed during our measurements that λ_{ph} is strongly influenced by the thickness of the underlying WSe_2 flake. This effect can readily be seen in the spatial s-SNOM scan shown in Figure 4.22a. In the upper area of this scan hBN is in direct contact with the underlying SiO_2, while in the middle area of the scan it is separated from SiO_2 by an increasing number of WSe_2 layers. It is in direct contact with SiO_2 again in the lower area of the scan. We observe that λ_{ph} continuously decreases with increasing N of the underlying WSe_2. This effect can be explained by the equation for the phonon polariton dispersion relation (Equation 4.15). λ_{ph} does not only depend on the permittivity of hBN but also on the permittivities of the surrounding materials. A varying thickness of the underlying WSe_2 leads to a change in the effective permittivity ϵ_{bottom} underneath the hBN and thus a change in λ_{ph}. This effect is more pronounced on the devices placed on SiO_2 substrates rather than on HfO_2 substrates

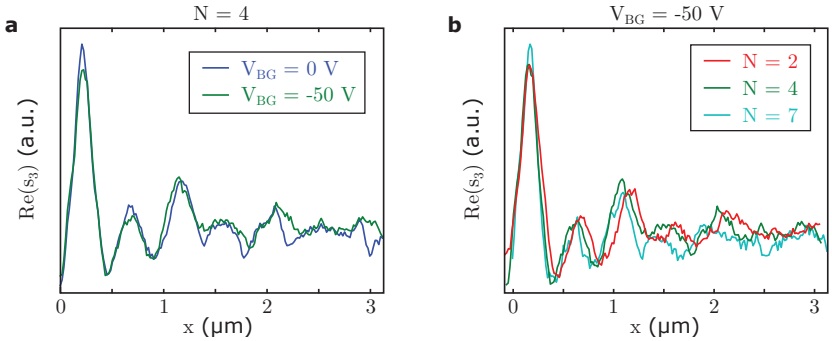

Figure 4.23: **Interaction of phonon polaritons with intersubband transitions. a**, Observed phonon polariton fringe pattern on the WSe_2 area with $N = 4$, where the intersubband resonance energy is closest to the employed $E_{ph} = 187.8$ meV. The line scans were taken for intrinsic WSe_2 ($V_{BG} = 0$ V) and p-doped WSe_2 ($V_{BG} = -50$ V). Both fringe patterns were obtained during a single measurement, in which we changed V_{BG} between each line. The hBN thickness was $d = 95$ nm. **b**, Observed phonon polariton fringe patterns for p-doped WSe_2 and different layer numbers N. The measurement was obtained on the same flake and the same conditions as in **a**.

since the permittivity of HfO_2 is closer to the one of WSe_2 in the wavelength region of the upper reststrahlen band. We can simulate the decrease of λ_{ph} with increasing WSe_2 thickness by using the transfer matrix method. The obtained result together with the measured values for various WSe_2 thicknesses are shown in Figure 4.22b. The simulation captures well the general trend of the decrease of λ_{ph}, as well as its order of magnitude. Only the last measured point for a WSe_2 thickness $N = 30$ nm deviates from the simulation. Further measurements are needed in order to explain this deviation.

Finally, we studied the interaction between intersubband transitions and the hyperbolic phonon polaritons. There are two principal ways how we can study the influence of intersubband transitions on the phonon polaritons. First, we can vary V_{BG} while scanning the resonant $N = 4$ area of WSe_2, thereby populating the first subband of the valence band and allowing for intersubband transitions to occur. This measurement is shown in Figure 4.23a. It shows two line scans, taken at $V_{BG} = 0$ V (charge-neutral WSe_2) and $V_{BG} = -50$ V (p-doped WSe_2) at $E_{ph} = 187.8$ meV. We can observe that the two line profiles overlap very well, thus not revealing any interaction between the phonon polaritons and intersubband transitions. We repeated these measurements for several wavelengths spanning the complete upper reststrahlen band, without observing a significant effect. In a second measurement, we constantly p-doped WSe_2 by applying $V_{BG} = -50$ V and excite phonon polaritons in different layer numbers N. If an interaction occurs, we should observe a shorter decay length or a different phonon polariton wavelength λ_{ph} only for the layer number that is resonant with E_{ph} ($N = 4$). This measurement is shown in Figure 4.23b. However, we did not observe a significant difference between different layer numbers N for all measured wavelengths within the upper reststrahlen band. We performed both of these measurements on all of the fabricated devices without observing a significant effect.

A possible reason that we did not observe any interaction between intersubband transitions

and hBN phonon polaritons could be that the center energy of the intersubband transition lies just below the upper reststrahlen band. If the intrinsic linewidth of intersubband transitions is small, the overlap might not be sufficient for an effective coupling. Furthermore, we are lacking detailed theoretical calculations that quantify the expected reduction in decay length or change of λ_{ph} due to their interaction with intersubband transitions. Similar as for graphene plasmons, it might is possible that an interaction remains concealed in our measurements due to the fast intrinsic decay of the phonon polaritons.

4.4 Conclusions

We performed TMM calculations, in which we simulated the interaction between intersubband transitions in TMD quantum wells and graphene plasmons, separated by a thin spacer layer of hBN. We observed that the nature of the interaction is very sensitive to the assumed linewidth of the intersubband transitions. When we assumed a thermally broadened linewidth of 5.9 meV we observed that the interaction mainly manifests itself in a reduced propagation length of the graphene plasmons. For smaller linewidths (that can for example be achieved at low temperatures) we entered the strong coupling regime and observed a pronounced anticrossing. It is therefore crucial to experimentally determine the intrinsic linewidth of intersubband transitions in TMDs. We also observed that an Au substrate enhances the interaction between graphene plasmons and intersubband transitions due to the formation of acoustic plasmons and the associated high confinement of the electric field between Au and graphene. Here, the spacer layers play an important role, as thin spacer layers lead to smaller plasmon mode volumes and a correspondingly stronger interaction.

We also performed FDTD simulations and found large Purcell factors $>10^6$ of out-of-plane dipole emitters that we placed in between a graphene sheet and an Au rod. The reason for these large Purcell factors is the efficient excitation of acoustic plasmons and their reflection at the Au edge, forming a standing wave electric field pattern. This is a promising approach to efficiently outcouple photons from intersubband transitions for light emitting devices or to excite graphene plasmons by driving an electrical current through the TMD quantum well.

In the experimental part, we fabricated various van der Waals heterostructures on which we could observe graphene plasmons and hBN hyperbolic phonon polaritons. For the fabrication we used the dry-transfer technique as described in section 2.1.2. We excited and detected these surface polaritons by using the s-SNOM. The propagation length of both, graphene plasmons and hBN phonon polaritons were similar to the highest values reported at room temperature so far, indicating the high quality of our devices. We could in situ tune the graphene plasmon wavelength by electrostatically doping graphene. For hBN phonon polaritons, the polariton wavelength strongly depends on the excitation energy and hBN thickness and we could accurately model our measured values by using TMM simulations.

We furthermore observed that the hBN phonon polaritons are strongly influenced by their surrounding materials. The hBN phonon polariton wavelength depends strongly on the thickness of the underlying WSe_2, which modifies its dielectric environment. This effect demonstrates that 2D polaritons are very sensitive to their dielectric environment.

However, we could not observe any interaction between the graphene plasmons or hBN phonon polaritons and the intersubband transitions in WSe_2. We populated the first subband of the valence band of WSe_2 in order to allow intersubband absorption but could not observe a difference in the polariton propagation lengths or wavelengths in comparison to when the WSe_2 was charge neutral. There are several possible reasons why we could not observe any interaction. First, it might be that the intrinsic losses within the polaritons are too high and any interaction with the intersubband transitions remains hidden in our measurements. In order to exclude this we need detailed calculations that quantitatively predict the effects that we expect to observe in our experiments. It is also possible that the intrinsic linewidth of the intersubband transitions is larger than we expect (for example due to disorder), hence leading to a weaker interaction that is not observable in our experiments. Therefore, it is crucial to experimentally determine the intrinsic linewidth of intersubband transitions in TMDs. Another possible reason could be that our excitation photon energy E_{ph} did not overlap with the center of the intersubband transition. In order to overcome this uncertainty, we would need to perform spectrally resolved measurements, preferably in the far-field. Finally, it might be that that the proximity of hBN and in particular graphene modifies the quantum well potential and therefore shifts the intersubband transition energies. A crucial parameter for this effect is the thickness of the spacer layer d_s between the TMD quantum well and graphene. For smaller d_s the experimental signature of an interaction between graphene and intersubband transitions increases strongly, however this also leads to a larger modification of the quantum well energy levels. Therefore, we need detailed theoretical calculations on the quantum well energy states taking into account the complete device geometry, as well as the expected effect that an interaction between intersubband transitions and 2D polaritons would have on the polariton dispersion relation. These calculations will allow us to design the appropriate design geometries for future measurements.

Conclusions and Outlook

In this thesis, we explored intersubband transitions in transition metal dichalcogenides (TMDs). Since intersubband transitions had previously not been studied in 2D materials, we first laid their theoretical framework (Chapter 1). By using ab initio DFT calculations, we calculated the charge carriers' out-of-plane wave functions and found that charge carriers at the conduction band minimum and valence band maximum couple well between adjacent layers, leading to the formation of subbands. This is not the case at other points in the Brillouin zone, where charge carriers are confined within their respective layers and subbands are degenerate. We therefore found that the existence of intersubband transitions in TMDs is not trivial but rather results from the fact that there is a strong interlayer coupling of charge carriers precisely at the conduction band minimum and valence band maximum.

The experimental observation of intersubband transitions in TMDs holds several challenges. First, exfoliated TMD flakes with a constant thickness come in typical sizes of a few μm^2 and are therefore smaller than the diffraction limited spot size of mid-infrared laser sources. Second, in order to excite intersubband transitions, an out-of-plane polarization of the electric field is needed. Finally, the expected absorption of a single quantum well is small and therefore a very sensitive measurement technique is required. In order to overcome these challenges, we used scattering scanning near-field optical microscopy (Chapter 2). This technique allowed us to measure the complex permittivity of our sample with a spatial resolution of $\sim$10 nm, regardless of the employed excitation energy. Furthermore, the near-field around the AFM tip apex provided the necessary out-of-plain polarization component of the electric field in order to excite intersubband transitions. Finally, in order to increase the signal to noise ratio of our measurements, we modulated the doping of the TMD quantum wells by applying an external gate voltage. This modulation technique provided the necessary sensitivity to probe the intersubband absorption of a single quantum well.

In the experimental data (Chapter 3), we could spatially and spectrally resolve intersubband transitions. Within the wavelength ranges of our lasers, we could observe two clear resonances for different layer numbers N within a single flake. The observed resonance energies are in good agreement with the theoretical calculations performed in Chapter 1 and show indications of many-body effects, which is interesting to explore in future studies. The observed linewidth of the transitions was larger than the theoretical calculations, which we attributed to non-vertical transitions, where momentum was provided by the sharp AFM tip apex. We could in situ tune the doping – and therefore the absorption – of intersubband transitions and observed absorption in both the conduction and valence band.

Finally, we studied the interactions between TMD intersubband transitions and graphene plasmons or hBN hyperbolic phonon polaritons (Chapter 4). We performed TMM and FDTD simulations and found Purcell factors $>10^6$ with the possibility of reaching the strong cou-

pling regime. Important parameters for the strength of the interaction are the intersubband linewidth and the separation between the quantum well and the 2D polariton. The high Purcell factors can be reached by using an Au substrate, which leads to the formation of acoustic plasmons and a correspondingly higher confinement of the electric field.[238] In order to experimentally study the interaction between intersubband transitions and 2D polaritons, we placed graphene or hBN in close proximity of a TMD quantum well that shows an intersubband transition at the employed excitation photon energy. We first characterized the graphene plasmons and hBN phonon polaritons and found decay lengths and confinement factors similar to values reported in literature. We also found that hBN phonon polaritons are strongly influenced by their dielectric environment and we could observe a strong decrease of the polariton wavelength for increasing TMD thicknesses. However, we could not observe any interaction between the intersubband transitions and the 2D polaritons. Here, we need more detailed theoretical calculations that would allow us to improve our device geometry.

In conclusion, we reported the first study of intersubband transitions in 2D materials. To our knowledge, this is also the first time in any material that intersubband transitions were resolved with a nanometer scale spatial resolution. One advantage of intersubband transitions in TMDs are the atomically flat interfaces that should lead to a reduced broadening of the linewidth due to reduced interface roughness scattering. In our study, however, we could not determine the intrinsic linewidth due to the additional broadening induced by the sharp AFM tip. We therefore cannot exclude any additional broadening mechanisms due to disorder. A promising way to explore these limits are FTIR measurements.[12,149] These experiments have become possible recently due to the advances in growth of large area few-layer TMD flakes and should provide clarity on the intrinsic linewidth. FTIR measurements would also enable a temperature dependent study. This is interesting since we expect the linewidth at room temperature to be dominated by the different in-plane masses of the first two subbands. At lower temperatures this broadening becomes smaller and we should be able to directly probe the phonon-limited broadening.

Another advantage of intersubband transitions in 2D materials is their potential for integration with Si integrated circuits, cavities and waveguides, as well as van der Waals heterostructures, in which they can be combined with any material of the large family of 2D materials. We have already simulated the interactions between TMD quantum wells and graphene plasmons and have fabricated van der Waals heterostructures in which we placed TMD quantum wells in direct proximity of both graphene and hBN. However, more exotic coupling mechanisms might also be possible: One could for example imagine to couple intersubband transitions to Cooper pairs[241] in 2D superconductors.[34–39] The tunability of the intersubband transition energy via the TMD thickness, as well as the possibility to place a TMD quantum well in direct proximity of a 2D superconductor provide the necessary prerequisites for such a coupling. However, only detailed theoretical calculations can confirm if this coupling will indeed be possible. Overall, the research on intersubband transitions in 2D materials is only at its beginning – both theoretically and experimentally – and in this thesis we have only scratched on the surface of the plethora of possibilities that this field has to offer.

A Appendices

A.1 DFT simulations for WSe_2 and MoS_2

Here, we compare the semiconducting 2D materials MoS_2 and WSe_2 by presenting further DFT calculations, obtained by using the same DFT code as in section 1.4.1 of the main text.

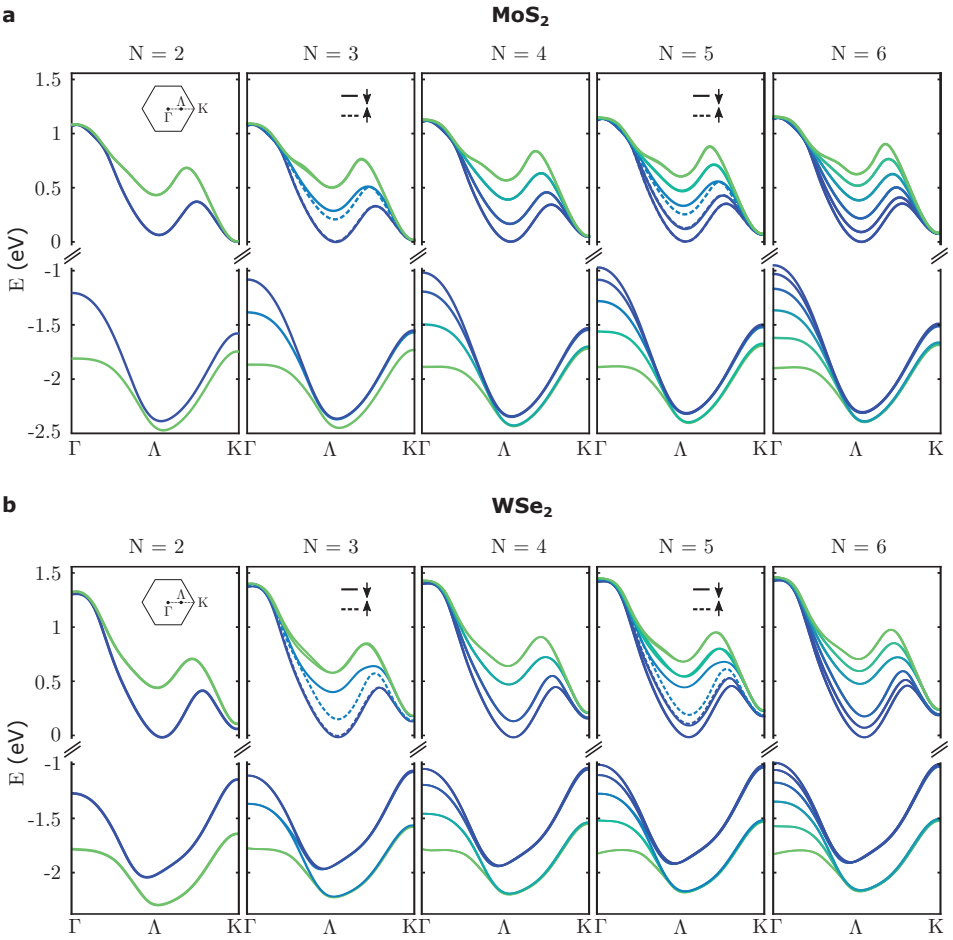

Figure A.1: Bandstructure calculations obtained by DFT simulations for MoS_2 (**a**) and WSe_2 (**b**). The data in **b** are also presented in Figure 1.5 of the main text.

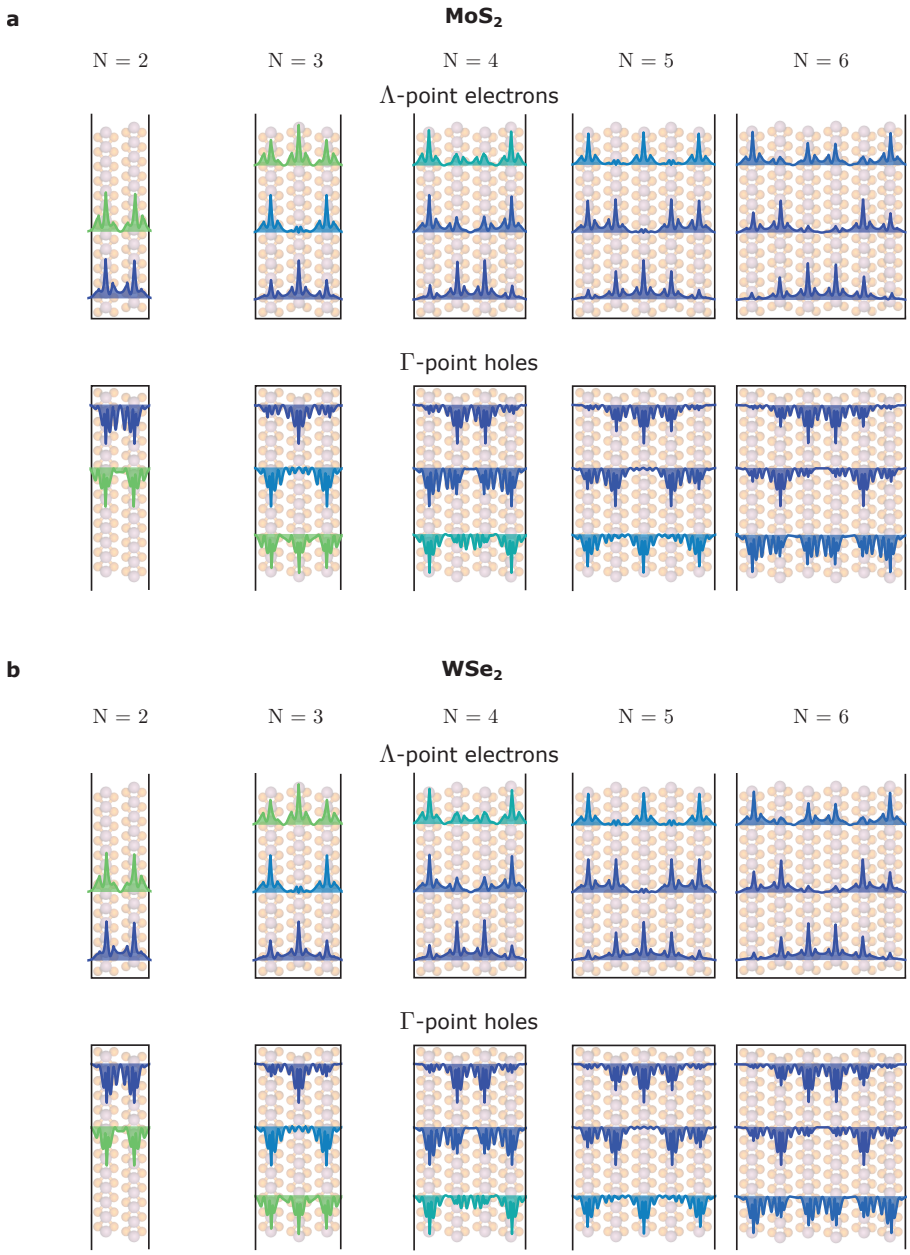

Figure A.2: Out-of-plane wave functions for electrons at the Λ-point and holes at the Γ-point of the Brillouin zone for different layer numbers N in MoS_2 (**a**) and WSe_2 (**b**). The data in **b** are also presented in Figure 1.5 of the main text.

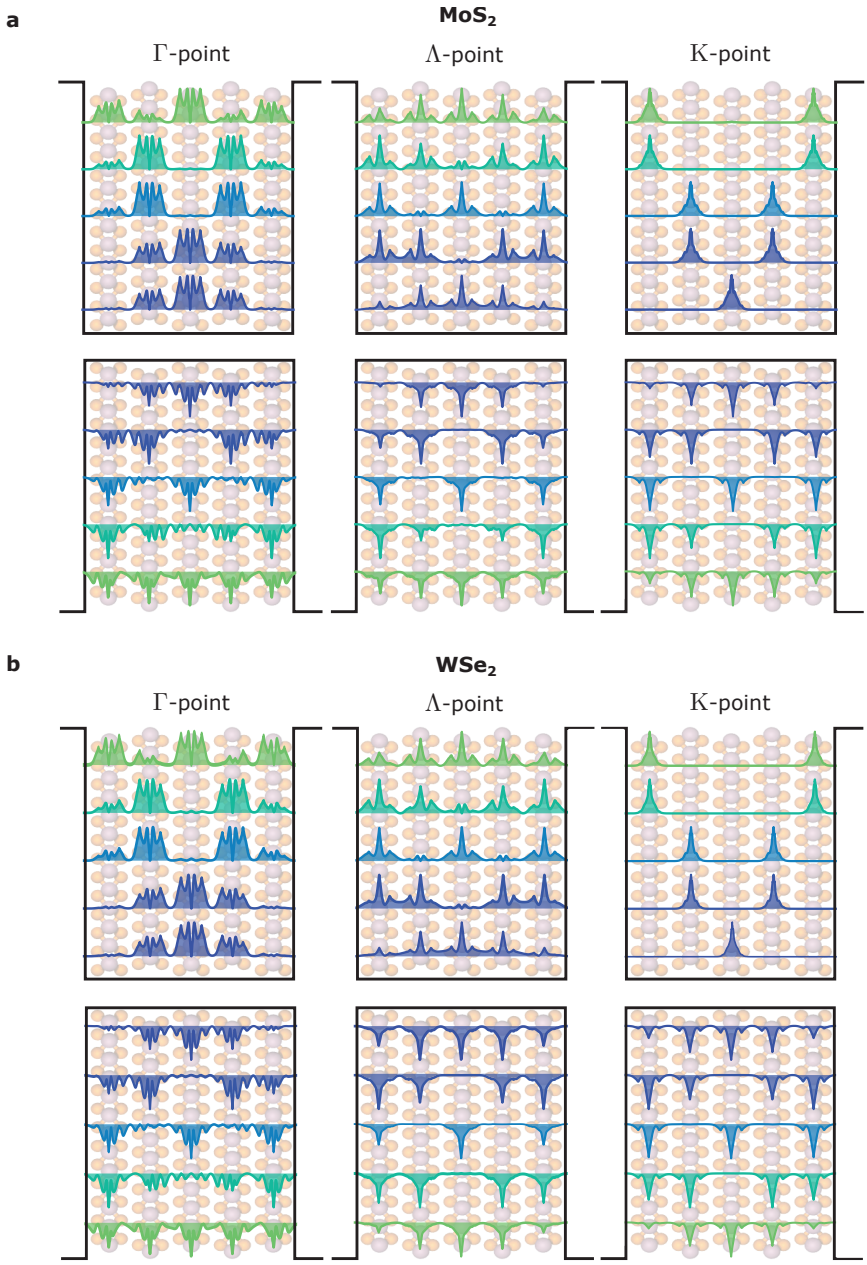

Figure A.3: Out-of-plane wave functions for electrons and holes at different points of the Brillouin zone in an $N = 5$ crystal of MoS_2 (**a**) and WSe_2 (**b**). The data in **b** are also presented in Figure 1.6 of the main text.

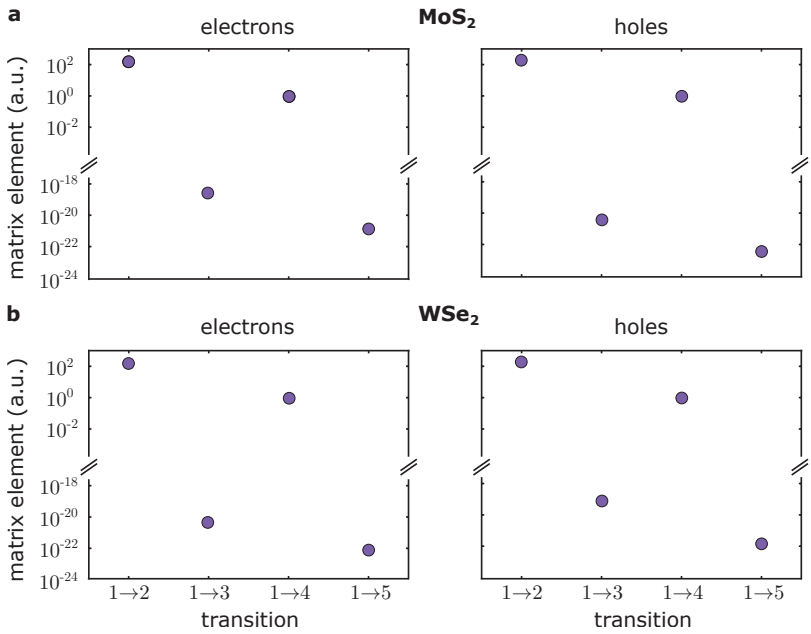

Figure A.4: Calculated transition matrix elements for electrons at the Λ-point and holes at the Γ-point in an $N = 5$ crystal of MoS_2 (**a**) and WSe_2 (**b**) for transitions from the first to the second subband. The data in **b** are also presented in Figure 1.8 of the main text.

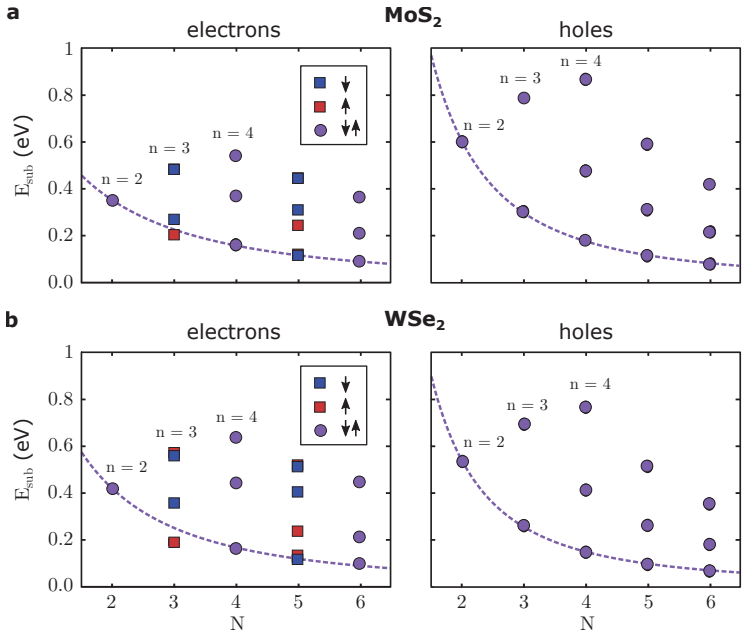

Figure A.5: Intersubband transition energies from the first subband to the next few subbands $n = 2$, 3, 4 for different layer numbers N in MoS_2 (**a**) and WSe_2 (**b**). The dashed line is a fit to the modified infinite square well model (Equation 1.14 of the main text).

A.2 Fabrication recipes

Here, we describe in detail the steps for preparing the transfer pad, which is used to assemble van der Waals heterostructures.

1. Start from a 5% solution of PC (Poly(Bisphenol A carbonate)) in chloroform.
2. Put a few drops of the PC solution on a standard microscope glass slide. Bring this glass slide in contact with a second microscope slide and separate them by sliding one off the other. This gives a continuous thin film of PC on both glass slides. Let it dry for a few minutes.
3. Prepare another microscope glass slide by placing it into a low-power oxygen plasma for $\sim$1 minute. This helps to provide a good adhesion for the PDMS that is placed on top later on.
4. Cut a small hole ($\sim$5 x 5 mm^2) into a double-sided tape and place the tape close to the short edge of the microscope slide that has previously been placed in the oxygen plasma.
5. Place a small piece of home-grown PDMS (see below for the growth recipe) inside the hole of the tape. The PDMS should attach well to the microscope slide.
6. Place the microscope slide again into a low-power oxygen plasma for $\sim$1 minute in order to provide good adhesion for the PC that is placed on top of the PDMS later on.
7. Cut a circular hole into a new tape. This hole should be larger than the previous rectangular one. Place the tape with the hole on top of the glass slide covered by the PC film and gently peel off the tape. The PC gets removed and remains suspended over the hole of the tape.
8. Place the suspended PC over the PDMS piece placed on top of the microscope slide. The PC should form a smooth surface over the PDMS and can be used for transfer.
9. If necessary place the entire glass slide on top of a hot plate at $\sim$70 °C. This removes any wrinkles from the PC that might have occurred during the preparation process. A photo of a prepared transfer pad is shown in Figure A.6a.

Recipe for the PDMS preparation:

1. Mix a $\sim$10:1 solution of Sylgard 184 Silicone elastomer and curing agent inside a petri dish. In a 14.5 cm diameter petri dish mixing 12g:1g will result in $\sim$1 mm thick film, which is ideal.
2. Stir vigorously using a plastic rod ($\sim$3 minutes) and then spread out the mixture evenly within the petri dish. At this stage it will be very bubbly.
3. Place the petri dish on top of a sonicator for a few minutes. This will remove most of the bubbles. Remove the remaining bubbles using a plastic rod.
4. Cover the petri dish and cure overnight at room temperature on a flat surface.

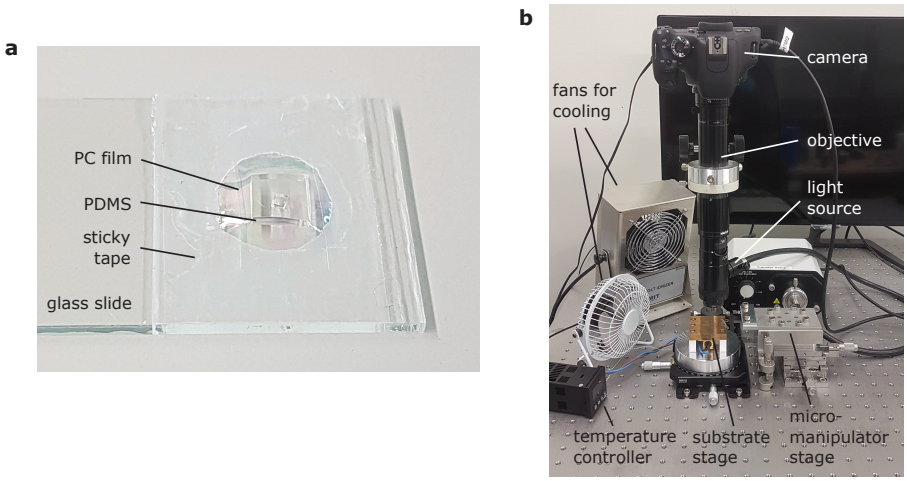

Figure A.6: **Photos of the transfer setup. a**, Photo of a prepared transfer pad as described in the text. **b**, Photo of the transfer setup. The microscope glass slide can be placed into the micromanipulator stage, where it can be aligned with the substrate stage. The substrate stage can be rotated to adjust the angle between adjacent flakes. Its temperature is controlled by a resistive heater.

A.3 Parameters of the finite-dipole model

The effective polarizability of the coupled tip-sample system (described in the main text in section 2.2.2) is given as

$$\alpha_{\text{eff}} = C\left(2 + \frac{f_0(H)\,\beta}{1 - f(H)\,\beta}\right), \tag{A.1}$$

where C, $f_0(H)$, $f(H)$ are defined by the tip properties as follows:[155,158]

$$C = R_\text{t}^2 L_\text{t} \frac{\frac{2L_\text{t}}{R_\text{t}} + \ln\frac{R_\text{t}}{4L_\text{t}}}{\ln\frac{4L_\text{t}}{R_\text{t}} - 2\frac{\epsilon_\text{t} - \frac{L_\text{t}}{R_\text{t}}}{\epsilon_\text{t}-1}}, \tag{A.2}$$

where $L_\text{t} \approx$ 600 nm is the effective tip length, $R_\text{t} \approx$ 15 nm is the tip radius and $\epsilon_\text{t} \approx$ -10^3 is the tip permittivity.

$$f_0(H) = \left(g - \frac{2H + W_0 + R_\text{t}}{2L_\text{t}}\right) \frac{\ln\frac{4L_\text{t}}{4H+2W_0+R_\text{t}}}{\ln\frac{4L_\text{t}}{R_\text{t}}}, \tag{A.3}$$

where $W_0 \approx 1.31\frac{R_\text{t}L_\text{t}}{L_\text{t}+2R_\text{t}}$ is the vertical position inside the tip where the polarization charge induced in the absence of a sample has to be placed to yield the correct field lines and $g \approx 0.7\exp(0.06\text{i})$ is the fraction of this charge that participates in the near-field coupling.

$$f(H) = \left(g - \frac{2H + W_i + R_\mathrm{t}}{2L_\mathrm{t}} \right) \frac{\ln \frac{4L_\mathrm{t}}{4H+2R_\mathrm{t}}}{\ln \frac{4L_\mathrm{t}}{R_\mathrm{t}}}, \tag{A.4}$$

where $W_i \approx \frac{W_t}{2}$ is the location of the charge induced due to the near-field interaction.

Publications

The results presented in this thesis have led to the following publication:

P. Schmidt, F. Vialla, S. Latini, M. Massicotte, K.-J. Tielrooij, S. Mastel, G. Navickaite, M. Danovich, D. A. Ruiz-Tijerina, C. Yelgel, V. Fal'ko, K. S. Thygesen, R. Hillenbrand and F. H. L. Koppens
Nano-imaging of intersubband transitions in van der Waals quantum wells. *Nature Nanotechnology* **13**, 1035–1041 (2018)

Cover image: Fabien Vialla

Other publications by the author:

- M. Massicotte, P. Schmidt, F. Vialla, K. G. Schädler, A. Reserbat-Plantey, K. Watanabe, T. Taniguchi, K.-J. Tielrooij and F. H. L. Koppens
  Picosecond photoresponse in van der Waals heterostructures. *Nature Nanotechnology* **11**, 42–46 (2016)
  In this work, we demonstrated photocurrent with response times as short as a few picoseconds in van der Waals heterostructures consisting of graphene/WSe_2/graphene.
- M. Massicotte, P. Schmidt, F. Vialla, K. Watanabe, T. Taniguchi, K.-J. Tielrooij and F. H. L. Koppens
  Photo-thermionic effect in vertical graphene heterostructures. *Nature Communications* **7**, 12174 (2016)
  In this work, we reported on a new photocurrent generation mechanism where hot charge carriers in graphene are extracted via the Schottky barrier formed at a graphene/WSe_2 interface.
- M. Massicotte, F. Vialla, P. Schmidt, M. B. Lundeberg, S. Latini, S. Haastrup, M. Danovich, D. Davydovskaya, K. Watanabe, T. Taniguchi, V. Fal'ko, K. S. Thygesen, T. G. Pedersen and F. H. L. Koppens
  Dissociation of two-dimensional excitons in monolayer WSe_2. *Nature Communications* **9**, 1633 (2018)
  In this work, we identified the main dissociation mechanism of the strongly bound excitons in monolayer WSe_2 under the influence of an electric field.

- F. Vialla, M. Danovich, D. A. Ruiz-Tijerina, M. Massicotte, P. Schmidt, T. Taniguchi, K. Watanabe, R. J. Hunt, M. Szyniszewski, N. D. Drummond, T. G. Pedersen, V. Fal'ko and F. H. L. Koppens
  Tuning of impurity-bound interlayer complexes in a van der Waals heterobilayer. *Under review*
  In this work, we theoretically and experimentally investigated interlayer excitons in a $MoSe_2/WSe_2$ van der Waals heterostructure and identified them as impurity-bound complexes.
- K.-J. Tielrooij, N. C. H. Hesp, A. Principi, M. B. Lundeberg, E. A. A. Pogna, L. Banszerus, Z. Mics, M. Massicotte, P. Schmidt, D. Davydovskaya, D. G. Purdie, I. Goykhman, G. Soavi, A. Lombardo, K. Watanabe, T. Taniguchi, M. Bonn, D. Turchinovich, C. Stampfer, A. C. Ferrari, G. Cerullo, M. Polini and F. H. L. Koppens
  Out-of-plane heat transfer in van der Waals stacks through electron–hyperbolic phonon coupling. *Nature Nanotechnology* **13**, 41–46 (2018)
- B. Buades, D. Moonshiram, T. P. H. Sidiropoulos, I. León, P. Schmidt, I. Pi, N. Di Palo, S. L. Cousin, A. Picón, F. H. L. Koppens and J. Biegert
  Dispersive soft X-ray absorption fine-structure spectroscopy in graphite with an attosecond pulse. *Optica* **5**, 502–506 (2018)

During the course of my PhD thesis I also supervised the following works:

- Nicola Melchioni, Coupling of intersubband transitions with surface polaritons in van der Waals heterostructures. *Master's thesis* (2018)
- Md Masudur Rahman, Intersubband transition in TMD quantum well. *Internship report* (2018)
- Nicolas Perez, Fabrication and photocurrent measurements of heterostructures made by stacking graphene and other graphene-like 2D materials. *Internship report* (2015)

Bibliography

1. Kroemer, H. Quasi-electric fields and band offset: Teaching electrons new tricks. *Nobel Lecture* (2000).

2. Alferov, Z. I. The double heterostructure concept and its applications in physics, electronics, and technology. *Nobel Lecture* (2000).

3. Hayashi, I., Panish, M. B., Foy, P. W. & Sumski, S. Junction lasers which operate continuously at room temperature. *Applied Physics Letters* **17**, 109–111 (1970).

4. Day, D. J. *et al.* Double quantum well resonant tunnel diodes. *Applied Physics Letters* **57**, 1260–1261 (1990).

5. Dingle, R., Stoermer, H. L., Gossard, A. C. & Wiegmann, W. Electron mobilities in modulation-doped semiconductor heterojunction superlattices. *Applied Physics Letters* **33**, 665–667 (1978).

6. Mimura, T., Hiyamizu, S., Fujii, T. & Nanbu, K. A new field-effect transistor with selectively doped GaAs/n-$Al_xGa_{1-x}As$ heterojunctions. *Japanese Journal of Applied Physics* **19**, L225–L227 (1980).

7. Delagebeaudeuf, D. *et al.* Two-dimensional electron gas m.e.s.f.e.t. structure. *Electronics Letters* **16**, 667–668 (1980).

8. Tsui, D. C., Stormer, H. L. & Gossard, A. C. Two-dimensional magnetotransport in the extreme quantum limit. *Physical Review Letters* **48**, 1559–1562 (1982).

9. Nakamura, S., Mukai, T. & Senoh, M. Candela-class high-brightness InGaN/AlGaN double-heterostructure blue-light-emitting diodes. *Applied Physics Letters* **64**, 1687–1689 (1994).

10. Kamgar, A., Kneschaurek, P., Dorda, G. & Koch, J. F. Resonance spectroscopy of electronic levels in a surface accumulation layer. *Physical Review Letters* **32**, 1251–1254 (1974).

11. Joyce, B. Molecular beam epitaxy. *Reports on Progress in Physics* **48**, 1637–1697 (1985).

12. West, L. C. & Eglash, S. J. First observation of an extremely large-dipole infrared transition within the conduction band of a GaAs quantum well. *Applied Physics Letters* **46**, 1156–1158 (1985).

13. Esaki, L. & Tsu, R. Superlattice and negative differential conductivity in semiconductors. *IBM Journal of Research and Development* **14**, 61–65 (1970).

14. Rogalski, A. Quantum well photoconductors in infrared detector technology. *Journal of Applied Physics* **93**, 4355–4391 (2003).

15. Faist, J. *et al.* Quantum cascade laser. *Science* **264**, 553–556 (1994).

16. Bonaccorso, F., Sun, Z., Hasan, T. & Ferrari, A. C. Graphene photonics and optoelectronics. *Nature Photonics* **4**, 611–622 (2010).

17. Wang, L. *et al.* One-dimensional electrical contact to a two-dimensional material. *Science* **342**, 614–617 (2013).

18. Nair, R. R. *et al.* Fine structure constant defines visual transperency of graphene. *Science* **320**, 1308 (2008).

19. Balandin, A. A., Ghosh, S. & Bao, W. Superior thermal conductivity of single-layer graphene. *Nano Letters* **8**, 902–907 (2008).

20. Lee, C., Wei, X., Kysar, J. W. & Hone, J. Measurement of the elastic properties and intrinsic strength of monolayer graphene. *Science* **321**, 385–388 (2008).

21. Boehm, H. P., Clauss, A., Fischer, G. O. & Hofmann, U. Das Adsorptionsverhalten sehr dünner Kohlenstoff-Folien. *Journal of Inorganic and General Chemistry* **316**, 119–127 (1962).

22. Novoselov, K. S. *et al.* Electric field effect in atomically thin carbon films. *Science* **306**, 666–669 (2004).

23. Novoselov, K. S. *et al.* Two-dimensional gas of massless Dirac fermions in graphene. *Nature* **438**, 197–200 (2005).

24. Zhang, Y., Tan, Y. W., Stormer, H. L. & Kim, P. Experimental observation of the quantum Hall effect and Berry's phase in graphene. *Nature* **438**, 201–204 (2005).

25. Bolotin, K. I., Ghahari, F., Shulman, M. D., Stormer, H. L. & Kim, P. Observation of the fractional quantum Hall effect in graphene. *Nature* **462**, 196–199 (2009).

26. Novoselov, K. S. *et al.* Room-temperature quantum Hall effect in graphene. *Science* **315**, 1379 (2007).

27. Novoselov, K. S. Graphene: Materials in the flatland. *Nobel Lecture* (2010).

28. Geim, A. K. Random walk to graphene. *Nobel Lecture* (2010).

29. Novoselov, K. S. *et al.* Two-dimensional atomic crystals. *PNAS* **102**, 10451–10453 (2005).

30. Gong, C. *et al.* Discovery of intrinsic ferromagnetism in two-dimensional van der Waals crystals. *Nature* **546**, 265–269 (2017).

31. Huang, B. *et al.* Layer-dependent ferromagnetism in a van der Waals crystal down to the monolayer limit. *Nature* **546**, 270–273 (2017).

32. Fei, Z. *et al.* Edge conduction in monolayer WTe_2. *Nature Physics* **13**, 677–682 (2017).

33. Wu, S. *et al.* Observation of the quantum spin Hall effect up to 100 Kelvin in a monolayer crystal. *Science* **359**, 76–79 (2018).

34. Frindt, R. F. Superconductivity in ultrathin $NbSe_2$ layers. *Physical Review Letters* **28**, 299–301 (1972).

35. Staley, N. E. *et al.* Electric field effect on superconductivity in atomically thin flakes of $NbSe_2$. *Physical Review B* **80**, 184505 (2009).

36. Xi, X. *et al.* Ising pairing in superconducting $NbSe_2$ atomic layers. *Nature Physics* **12**, 139–143 (2016).

37. Ugeda, M. M. *et al.* Characterization of collective ground states in single-layer $NbSe_2$. *Nature Physics* **12**, 92–97 (2016).

38. Peng, R. *et al.* Measurement of an enhanced superconducting phase and a pronounced anisotropy of the energy gap of a strained FeSe single layer in $FeSe/Nb:SrTiO_3/KTaO_3$ heterostructures using photoemission spectroscopy. *Physical Review Letters* **112**, 107001 (2014).

39. Ge, J. F. *et al.* Superconductivity above 100 K in single-layer FeSe films on doped $SrTiO_3$. *Nature Materials* **14**, 285–289 (2015).

40. Geim, A. K. & Grigorieva, I. V. Van der Waals heterostructures. *Nature* **499**, 419–425 (2013).

41. Novoselov, K. S., Mishchenko, A., Carvalho, A. & Castro Neto, A. H. 2D materials and van der Waals heterostructures. *Science* **353**, 461 (2016).

42. Cui, X. *et al.* Multi-terminal transport measurements of MoS_2 using a van der Waals heterostructure device platform. *Nature Nanotechnology* **10**, 534–540 (2015).

43. Britnell, L. *et al.* Field-effect tunneling transistor based on vertical graphene heterostructures. *Science* **335**, 947–950 (2012).

44. Georgiou, T. *et al.* Vertical field-effect transistor based on graphene-WS_2 heterostructures for flexible and transparent electronics. *Nature Nanotechnology* **8**, 100–103 (2013).

45. Mishchenko, A. *et al.* Twist-controlled resonant tunnelling in graphene/boron nitride/graphene heterostructures. *Nature Nanotechnology* **9**, 808–813 (2014).

46. Yang, H. *et al.* Graphene barristor, a triode device with a gate-controlled Schottky barrier. *Science* **336**, 1140–1143 (2012).

47. Britnell, L. *et al.* Strong light-matter interactions in heterostructures of atomically thin films. *Science* **340**, 1311–1314 (2013).

48. Withers, F. *et al.* Light-emitting diodes by band-structure engineering in van der Waals heterostructures. *Nature Materials* **14**, 301–306 (2015).

49. Woessner, A. *et al.* Highly confined low-loss plasmons in graphene–boron nitride heterostructures. *Nature Materials* **14**, 421–425 (2015).

50. Cheng, R. *et al.* Electroluminescence and photocurrent generation from atomically sharp WSe_2/MoS_2 heterojunction p-n diodes. *Nano Letters* **14**, 5590–5597 (2014).

51. Woessner, A. *et al.* Propagating plasmons in a charge-neutral quantum tunneling transistor. *ACS Photonics* **4**, 3012–3017 (2017).

52. Gong, C. *et al.* Band alignment of two-dimensional transition metal dichalcogenides: Application in tunnel field effect transistors. *Applied Physics Letters* **103**, 053513 (2013).

53. Kim, K. *et al.* Van der Waals heterostructures with high accuracy rotational alignment. *Nano Letters* **16**, 1989–1995 (2016).

54. Li, G. *et al.* Observation of Van Hove singularities in twisted graphene layers. *Nature Physics* **6**, 109–113 (2010).

55. Xue, J. *et al.* Scanning tunnelling microscopy and spectroscopy of ultra-flat graphene on hexagonal boron nitride. *Nature Materials* **10**, 282–285 (2011).

56. Kim, K. *et al.* Tunable moiré bands and strong correlations in small-twist-angle bilayer graphene. *PNAS* **114**, 3364–3369 (2017).

57. Dean, C. R. *et al.* Hofstadter's butterfly and the fractal quantum Hall effect in moiré superlattices. *Nature* **497**, 598–602 (2013).

58. Gorbachev, R. V. *et al.* Detecting topological currents in graphene superlattices. *Science* **346**, 448–451 (2014).

59. Cao, Y. *et al.* Correlated insulator behaviour at half-filling in magic-angle graphene superlattices. *Nature* **556**, 80–84 (2018).

60. Cao, Y. *et al.* Unconventional superconductivity in magic-angle graphene superlattices. *Nature* **556**, 43–50 (2018).

61. Radisavljevic, B., Radenovic, A., Brivio, J., Giacometti, V. & Kis, A. Single-layer MoS_2 transistors. *Nature Nanotechnology* **6**, 147–150 (2011).

62. Li, Y., Duerloo, K. A. N., Wauson, K. & Reed, E. J. Structural semiconductor-to-semimetal phase transition in two-dimensional materials induced by electrostatic gating. *Nature Communications* **7**, 10671 (2016).

63. Wilson, J. & Yoffe, A. The transition metal dichalcogenides discussion and interpretation of the observed optical, electrical and structural properties. *Advances in Physics* **18**, 193–335 (1969).

64. Wang, H. *et al.* Integrated circuits based on bilayer MoS_2 transistors. *Nano Letters* **12**, 4674–4680 (2012).

65. Sarkar, D. *et al.* A subthermionic tunnel field-effect transistor with an atomically thin channel. *Nature* **526**, 91–95 (2015).

66. Xu, S. *et al.* Odd-Integer quantum Hall states and giant spin susceptibility in p-type few-layer WSe_2. *Physical Review Letters* **118**, 067702 (2017).

67. Mak, K. F. *et al.* Tightly bound trions in monolayer MoS_2. *Nature Materials* **12**, 207–211 (2013).

68. Mak, K. F., Lee, C., Hone, J., Shan, J. & Heinz, T. F. Atomically thin MoS_2: A new direct-gap semiconductor. *Physical Review Letters* **105**, 136805 (2010).

69. Splendiani, A. *et al.* Emerging photoluminescence in monolayer MoS_2. *Nano Letters* **10**, 1271–1275 (2010).

70. Zhang, Y. *et al.* Direct observation of the transition from indirect to direct bandgap in atomically thin epitaxial $MoSe_2$. *Nature Nanotechnology* **9**, 111–115 (2014).

71. Mak, K. F. & Shan, J. Photonics and optoelectronics of 2D semiconductor transition metal dichalcogenides. *Nature Photonics* **10**, 216–226 (2016).

72. Ramasubramaniam, A. Large excitonic effects in monolayers of molybdenum and tungsten dichalcogenides. *Physical Review B* **86**, 115409 (2012).

73. He, K. *et al.* Tightly bound excitons in monolayer WSe_2. *Physical Review Letters* **113**, 026803 (2014).

74. Wang, G. *et al.* Colloquium: Excitons in atomically thin transition metal dichalcogenides. *Reviews of Modern Physics* **90**, 21001 (2018).

75. Chernikov, A. *et al.* Exciton binding energy and nonhydrogenic Rydberg series in monolayer WS_2. *Physical Review Letters* **113**, 076802 (2014).

76. Massicotte, M. *et al.* Dissociation of two-dimensional excitons in monolayer WSe_2. *Nature Communications* **9**, 1633 (2018).

77. Scuri, G. *et al.* Large excitonic reflectivity of monolayer $MoSe_2$ encapsulated in hexagonal boron nitride. *Physical Review Letters* **120**, 037402 (2018).

78. Back, P., Zeytinoglu, S., Ijaz, A., Kroner, M. & Imamoglu, A. Realization of an electrically tunable narrow-bandwidth atomically thin mirror using monolayer $MoSe_2$. *Physical Review Letters* **120**, 037401 (2018).

79. Cadiz, F. *et al.* Excitonic linewidth approaching the homogeneous limit in MoS_2-based van der Waals heterostructures. *Physical Review X* **7**, 021026 (2017).

80. Ajayi, O. A. *et al.* Approaching the intrinsic photoluminescence linewidth in transition metal dichalcogenide monolayers. *2D Materials* **4**, 031011 (2017).

81. Wang, Q. H., Kalantar-Zadeh, K., Kis, A., Coleman, J. N. & Strano, M. S. Electronics and optoelectronics of two-dimensional transition metal dichalcogenides. *Nature Nanotechnology* **7**, 699–712 (2012).

82. Koppens, F. H. L. *et al.* Photodetectors based on graphene, other two-dimensional materials and hybrid systems. *Nature Nanotechnology* **9**, 780–793 (2014).

83. Lopez-Sanchez, O., Lembke, D., Kayci, M., Radenovic, A. & Kis, A. Ultrasensitive photodetectors based on monolayer MoS_2. *Nature Nanotechnology* **8**, 497–501 (2013).

84. Massicotte, M. *et al.* Picosecond photoresponse in van der Waals heterostructures. *Nature Nanotechnology* **11**, 42–46 (2016).

85. Palacios-Berraquero, C. *et al.* Atomically thin quantum light-emitting diodes. *Nature Communications* **7**, 12978 (2016).

86. Wu, S. *et al.* Monolayer semiconductor nanocavity lasers with ultralow thresholds. *Nature* **520**, 69–72 (2015).

87. Ye, Y. *et al.* Monolayer excitonic laser. *Nature Photonics* **9**, 733–737 (2015).

88. Salehzadeh, O., Djavid, M., Tran, N. H., Shih, I. & Mi, Z. Optically pumped two-dimensional MoS_2 lasers operating at room-temperature. *Nano Letters* **15**, 5302–5306 (2015).

89. Li, Y. *et al.* Room-temperature continuous-wave lasing from monolayer molybdenum ditelluride integrated with a silicon nanobeam cavity. *Nature Nanotechnology* **12**, 987–992 (2017).

90. Mak, K. F., McGill, K. L., Park, J. & McEuen, P. L. The valley Hall effect in MoS_2 transistors. *Science* **344**, 1489–1492 (2014).

91. Schaibley, J. R. *et al.* Valleytronics in 2D materials. *Nature Reviews Materials* **1**, 16055 (2016).

92. Faist, J. *Quantum Cascade Lasers* (Oxford University Press, 2013).

93. Liu, H. C. & Capasso, F. *Intersubband Transitions in Quantum Wells: Physics and Device Applications II* (Academic Press, 1999).

94. Paiella, R. *Intersubband Transitions in Quantum Structures* (McGraw-Hill Companies, 2006).

95. Fang, H. *et al.* Quantum of optical absorption in two-dimensional semiconductors. *PNAS* **110**, 11688–11691 (2013).

96. Lin, C., Grassi, R., Low, T. & Helmy, A. S. Multilayer black phosphorus as a versatile mid-infrared electro-optic material. *Nano Letters* **16**, 1683–1689 (2016).

97. Ouyang, L. *et al.* Microstructural characterization of thick ZnTe epilayers grown on GaSb, InAs, InP and GaAs (1 0 0) substrates. *Journal of Crystal Growth* **330**, 30–34 (2011).

98. Li, L. *et al.* Black phosphorus field-effect transistors. *Nature Nanotechnology* **9**, 372–377 (2014).

99. Sun, Z., Martinez, A. & Wang, F. Optical modulators with 2D layered materials. *Nature Photonics* **10**, 227–238 (2016).

100. Pospischil, A. *et al.* CMOS-compatible graphene photodetector covering all optical communication bands. *Nature Photonics* **7**, 892–896 (2013).

101. Vurgaftman, I., Meyer, J. R. & Ram-Mohan, L. R. Band parameters for III-V compound semiconductors and their alloys. *Journal of Applied Physics* **89**, 5815–5875 (2001).

102. Smith, D. J. *et al.* Atomic-scale characterization of (mostly zincblende) compound semiconductor heterostructures. *Journal of Physics: Conference Series* **471**, 012005 (2013).

103. Terazzi, R. *et al.* Bloch gain in quantum cascade lasers. *Nature Physics* **3**, 329–333 (2007).

104. Tsujino, S. *et al.* Interface-roughness-induced broadening of intersubband electroluminescence in p-SiGe and n-GaInAs/AlInAs quantum-cascade structures. *Applied Physics Letters* **86**, 062113 (2005).

105. Unuma, T., Yoshita, M., Noda, T., Sakaki, H. & Akiyama, H. Intersubband absorption linewidth in GaAs quantum wells due to scattering by interface roughness, phonons, alloy disorder, and impurities. *Journal of Applied Physics* **93**, 1586–1597 (2003).

106. Unuma, T. *et al.* Effects of interface roughness and phonon scattering on intersubband absorption linewidth in a GaAs quantum well. *Applied Physics Letters* **78**, 3448–3450 (2001).

107. Balkan, N. *et al.* Well-width dependence of interface roughness scattering in $GaAs/Ga_{1-x}Al_xAs$ quantum wells. *Superlattices and Microstructures* **22**, 263–271 (1997).

108. Warwick, C. A., Jan, W. Y., Ourmazd, A. & Harris, T. D. Does luminescence show semiconductor interfaces to be atomically smooth? *Applied Physics Letters* **56**, 2666–2668 (1990).

109. Kim, H. *et al.* Atomic resolution mapping of interfacial intermixing and segregation in InAs/GaSb superlattices: A correlative study. *Journal of Applied Physics* **113**, 103511 (2013).

110. Kaun, S. W. *et al.* GaN-based high-electron-mobility transistor structures with homogeneous lattice-matched InAlN barriers grown by plasma-assisted molecular beam epitaxy. *Semiconductor Science and Technology* **29**, 045011 (2014).

111. Masubuchi, S. *et al.* Autonomous robotic searching and assembly of two-dimensional crystals to build van der Waals superlattices. *Nature Communications* **9**, 1413 (2018).

112. Revolinsky, E. & Beerntsen, D. Electrical properties of the $MoTe_2$-WTe_2 and $MoSe_2$-WSe_2 systems. *Journal of Applied Physics* **35**, 2086–2089 (1964).

113. Schneemeyer, L. F. & Sienko, M. J. Crystal data for mixed-anion molybdenum dichalcogenides. *Inorganic Chemistry* **19**, 789–791 (1980).

114. Srivastava, S., Mandal, T. & Samantaray, B. Studies on layer disorder, microstructural parameters and other properties of tungsten-substituted molybdenum disulfide, $Mo_{1-x}W_xS_2$ ($0 \leq x \leq 1$). *Synthetic Metals* **90**, 135–142 (1997).

115. Ajalkar, B. D., Mane, R. K., Sarwade, B. D. & Bhosale, P. N. Optical and electrical studies on molybdenum sulphoselenide $[Mo(S_{1-x}Se_x)_2]$ thin films prepared by arrested precipitation technique (APT). *Solar Energy Materials and Solar Cells* **81**, 101–112 (2004).

116. Tongay, S. *et al.* Two-dimensional semiconductor alloys: Monolayer $Mo_{1-x}W_xSe_2$. *Applied Physics Letters* **104**, 012101 (2014).

117. Yang, L. *et al.* Large-area synthesis of monolayered $MoS_{2(1-x)}Se_{2x}$ with a tunable band gap and its enhanced electrochemical catalytic activity. *Nanoscale* **7**, 10490–10497 (2015).

118. Duan, X. *et al.* Synthesis of $WS_{2x}Se_{2-2x}$ alloy nanosheets with composition-tunable electronic properties. *Nano Letters* **16**, 264–269 (2016).

119. Rigosi, A. F., Hill, H. M., Rim, K. T., Flynn, G. W. & Heinz, T. F. Electronic band gaps and exciton binding energies in monolayer $Mo_xW_{1-x}S_2$ transition metal dichalcogenide

alloys probed by scanning tunneling and optical spectroscopy. *Physical Review B* **94**, 075440 (2016).

120. Schmidt, P. *et al.* Nano-imaging of intersubband transitions in van der Waals quantum wells. *Nature Nanotechnology* (2018).

121. Ruiz-Tijerina, D. A., Danovich, M., Yelgel, C., Zólyomi, V. & Fal'Ko, V. I. Hybrid k·p tight-binding model for subbands and infrared intersubband optics in few-layer films of transition-metal dichalcogenides: MoS_2, $MoSe_2$, WS_2, and WSe_2. *Physical Review B* **98**, 035411 (2018).

122. Nakwaski, W. Effective masses of electrons and heavy holes in GaAs, InAs, AlAs and their ternary compounds. *Physica B: Physics of Condensed Matter* **210**, 1–25 (1995).

123. Enkovaara, J. *et al.* Electronic structure calculations with GPAW: A real-space implementation of the projector augmented-wave method. *Journal of Physics: Condensed Matter* **22**, 253202 (2010).

124. Giannozzi, P. *et al.* QUANTUM ESPRESSO: A modular and open-source software project for quantum simulations of materials. *Journal of Physics: Condensed Matter* **21**, 395502 (2009).

125. Hicks, W. T. Semiconducting behavior of substituted tungsten diselenide and its analogues. *Journal of the Electrochemical Society* **111**, 1058–1065 (1964).

126. Sahin, H. *et al.* Anomalous Raman spectra and thickness-dependent electronic properties of WSe_2. *Physical Review B* **87**, 165409 (2013).

127. Huang, W., Luo, X., Gan, C. K., Quek, S. Y. & Liang, G. Theoretical study of thermoelectric properties of few-layer MoS_2 and WSe_2. *Physical Chemistry Chemical Physics* **16**, 10866 (2014).

128. Zhao, W., Ribeiro, R., Toh, M. & Carvalho, A. Origin of indirect optical transitions in few-layer MoS_2, WS_2, and WSe_2. *Nano Letters* **13**, 5627–5634 (2013).

129. Yun, W. S., Han, S. W., Hong, S. C., Kim, I. G. & Lee, J. D. Thickness and strain effects on electronic structures of transition metal dichalcogenides: 2H-MX_2 semiconductors (M = Mo, W; X = S, Se, Te). *Physical Review B* **85**, 033305 (2012).

130. Yeh, P. C. *et al.* Direct measurement of the tunable electronic structure of bilayer MoS_2 by interlayer twist. *Nano Letters* **16**, 953–959 (2016).

131. Kang, J., Zhang, L. & Wei, S.-H. A unified understanding of the thickness-dependent bandgap transition in hexagonal two-dimensional semiconductors. *The Journal of Physical Chemistry Letters* **7**, 597–602 (2016).

132. Danovich, M., Aleiner, I. L., Drummond, N. D. & Falko, V. I. Fast relaxation of photoexcited carriers in 2-D transition metal dichalcogenides. *IEEE Journal on Selected Topics in Quantum Electronics* **23**, 6000105 (2017).

133. Jin, Z., Li, X., Mullen, J. T. & Kim, K. W. Intrinsic transport properties of electrons and holes in monolayer transition-metal dichalcogenides. *Physical Review B* **90**, 045422 (2014).

134. Sohier, T., Calandra, M. & Mauri, F. Two-dimensional Fröhlich interaction in transition-metal dichalcogenide monolayers: Theoretical modeling and first-principles calculations. *Physical Review B* **94**, 085415 (2016).

135. Coleman, J. N. *et al.* Two-dimensional nano-sheets produced by liquid exfoliation of layered materials. *Science* **331**, 568–571 (2011).

136. Lee, Y.-H. *et al.* Synthesis of large-area MoS_2 atomic layers with chemical vapor deposition. *Advanced Materials* **24**, 2320–2325 (2012).

137. Wang, X. *et al.* Chemical vapor deposition growth of crystalline monolayer $MoSe_2$. *ACS Nano* **8**, 5125–5131 (2014).

138. Ubaldini, A., Jacimovic, J., Ubrig, N. & Giannini, E. Chloride-driven chemical vapor transport method for crystal growth of transition metal dichalcogenides. *Crystal Growth and Design* **13**, 4453–4459 (2013).

139. Shi, Y. *et al.* Van der Waals epitaxy of MoS_2 layers using graphene as growth templates. *Nano Letters* **12**, 2784–2791 (2012).

140. Edelberg, D. *et al.* Hundredfold enhancement of light emission via defect control in monolayer transition-metal dichalcogenides. *arXiv:1805.00127* (2018).

141. Blake, P. *et al.* Making graphene visible. *Applied Physics Letters* **91**, 063124 (2007).

142. Bright, T., Watjen, J., Zhang, Z., Muratore, C. & Voevodin, A. Optical properties of HfO_2 thin films deposited by magnetron sputtering: From the visible to the far-infrared. *Thin Solid Films* **520**, 6793–6802 (2012).

143. Lee, C. *et al.* Anomalous lattice vibrations of single-and few-layer MoS_2. *ACS Nano* **4**, 2695–2700 (2010).

144. Buscema, M., Steele, G. A., van der Zant, H. S. J. & Castellanos-Gomez, A. The effect of the substrate on the Raman and photoluminescence emission of single-layer MoS_2. *Nano Research* **7**, 561–571 (2014).

145. Li, X. L. *et al.* Determining layer number of two-dimensional flakes of transition-metal dichalcogenides by the Raman intensity from substrates. *Nanotechnology* **27**, 145704 (2016).

146. Ferrari, A. C. *et al.* Raman spectrum of graphene and graphene layers. *Physical Review Letters* **97**, 187401 (2006).

147. Ferrari, A. C. & Basko, D. M. Raman spectroscopy as a versatile tool for studying the properties of graphene. *Nature Nanotechnology* **8**, 235–246 (2013).

148. Pizzocchero, F. *et al.* The hot pick-up technique for batch assembly of van der Waals heterostructures. *Nature Communications* **7**, 11894 (2016).

149. Kane, M. J., Emeny, M. T., Apsley, N., Whitehouse, C. R. & Lee, D. Inter-sub-band absorption in GaAs/AlGaAs single quantum wells. *Semiconductor Science and Technology* **3**, 722–725 (1988).

150. Goossen, K. W. & Lyon, S. A. Grating enhanced quantum well detector. *Applied Physics Letters* **47**, 1257–1259 (1985).

151. Helm, M., Colas, E., England, P., DeRosa, F. & Allen, S. J. Observation of grating-induced intersubband emission from GaAs/AlGaAs superlattices. *Applied Physics Letters* **53**, 1714–1716 (1988).

152. Ocelic, N., Huber, A. & Hillenbrand, R. Pseudoheterodyne detection for background-free near-field spectroscopy. *Applied Physics Letters* **89**, 101124 (2006).

153. Taubner, T., Hillenbrand, R. & Keilmann, F. Nanoscale polymer recognition by spectral signature in scattering infrared near-field microscopy. *Applied Physics Letters* **85**, 5064–5066 (2004).

154. Huth, F. *et al.* Nano-FTIR absorption spectroscopy of molecular fingerprints at 20 nm spatial resolution. *Nano Letters* **12**, 3973–3978 (2012).

155. Govyadinov, A. A., Amenabar, I., Huth, F., Carney, P. S. & Hillenbrand, R. Quantitative measurement of local infrared absorption and dielectric function with tip-enhanced near-field microscopy. *The Journal of Physical Chemistry Letters* **4**, 1526–1531 (2013).

156. Keilmann, F. & Hillenbrand, R. Near-field microscopy by elastic light scattering from a tip. *Philosophical Transactions of the Royal Society A* **362**, 787–805 (2004).

157. Cvitkovic, A., Ocelic, N. & Hillenbrand, R. Analytical model for quantitative prediction of material contrasts in scattering-type near-field optical microscopy. *Optics Express* **15**, 8550–8565 (2007).

158. Govyadinov, A. A. *et al.* Recovery of permittivity and depth from near-field data as a step toward infrared nanotomography. *ACS Nano* **8**, 6911–6921 (2014).

159. Beal, A. & Liang, W. Excitons in 2H-WSe_2 and 3R-WS_2. *Journal of Physics C: Solid State Physics* **9**, 2459–2466 (1976).

160. Cardilli, M. C., Dabbicco, M., Mezzapesa, F. P. & Scamarcio, G. Linewidth measurement of mid infrared quantum cascade laser by optical feedback interferometry. *Applied Physics Letters* **108**, 031105 (2016).

161. Dazzi, A., Prazeres, R., Glotin, F. & Ortega, J. M. Local infrared microspectroscopy with subwavelength spatial resolution with an atomic force microscope tip used as a photothermal sensor. *Optics Letters* **30**, 2388–2390 (2005).

162. Topinka, M. A. *et al.* Imaging coherent electron flow from a quantum point contact. *Science* **289**, 2323–2326 (2000).

163. Topinka, M. A. *et al.* Coherent branched flow in a two-dimensional electron gas. *Nature* **410**, 183–186 (2001).

164. Drude, P. Zur Elektronentheorie der Metalle; I. Teil. *Annalen der Physik* **306**, 566–613 (1900).

165. Drude, P. Zur Elektronentheorie der Metalle; II. Teil. *Annalen der Physik* **308**, 369–402 (1900).

166. Sommerfeld, A. Zur Elektronentheorie der Metalle auf Grund der Fermischen Statistik - I. Teil: Allgemeines, Strömungs- und Austrittsvorgänge. *Zeitschrift für Physik* **47**, 1–32 (1928).

167. Sylvia, S. S. & Lake, R. K. Experimentally measured field effect mobilities for few layer van der Waals materials. *arXiv:1810.07734v1* (2018).

168. Ugeda, M. M. *et al.* Giant bandgap renormalization and excitonic effects in a monolayer transition metal dichalcogenide semiconductor. *Nature Materials* **13**, 1091–1095 (2014).

169. Low, T. *et al.* Polaritons in layered two-dimensional materials. *Nature Materials* **16**, 182–194 (2017).

170. Manasreh, M. *et al.* Origin of the blueshift in the intersubband infrared absorption in $GaAs/Al_{0.3}Ga_{0.7}As$ multiple quantum wells. *Physical Review B* **43**, 9996–9999 (1991).

171. Tsujino, S. *et al.* Peak position of the intersubband absorption spectrum of quantum wells with controlled electron concentrations. *Physical Review B* **62**, 1560–1563 (2000).

172. Shtrichman, I. *et al.* Depolarization shift of the intersubband resonance in a quantum well with an electron-hole plasma. *Physical Review B* **65**, 035310 (2001).

173. Allen, S., Tsui, D. & Vinter, B. On the absorption of infrared radiation by electrons in semiconductor inversion layers. *Solid State Communications* **88**, 939–942 (1993).

174. Fei, Z. *et al.* Infrared nanoscopy of Dirac plasmons at the graphene-SiO_2 interface. *Nano Letters* **11**, 4701–4705 (2011).

175. Ando, T. Self-consistent results for a $GaAs/Al_xGa_{1-x}$ As heterojunction. II. Low temperature mobility. *Journal of the Physical Society of Japan* **51**, 3900–3907 (1982).

176. Ando, T. Line width of inter-subband absorption in inversion layers scattering from charged ions. *Journal of the Physical Society of Japan* **54**, 2671–2675 (1985).

177. Kischkat, J. *et al.* Mid-infrared optical properties of thin films of aluminum oxide, titanium dioxide, silicon dioxide, aluminum nitride, and silicon nitride. *Applied Optics* **51**, 6789–6798 (2012).

178. Melchioni, N. Coupling of intersubband transitions with surface polaritons in van der Waals heterostructures. *Master's thesis* (2018).

179. Rahman, M. M. Intersubband transitions in TMD quantum wells. *Internship report* (2018).

180. Forn-Díaz, P., Lamata, L., Rico, E., Kono, J. & Solano, E. Ultrastrong coupling regimes of light-matter interaction. *arXiv:1804.09275v2* (2018).

181. Jablan, M., Buljan, H. & Soljačić, M. Plasmonics in graphene at infrared frequencies. *Physical Review B* **80**, 245435 (2009).

182. Koppens, F. H., Chang, D. E. & García De Abajo, F. J. Graphene plasmonics: A platform for strong light-matter interactions. *Nano Letters* **11**, 3370–3377 (2011).

183. Low, T. & Avouris, P. Graphene plasmonics for terahertz to mid-infrared applications. *ACS Nano* **8**, 1086–1101 (2014).

184. Chen, J. *et al.* Optical nano-imaging of gate-tunable graphene plasmons. *Nature* **487**, 77–81 (2012).

185. Fei, Z. *et al.* Gate-tuning of graphene plasmons revealed by infrared nano-imaging. *Nature* **487**, 82–85 (2012).

186. Purcell, E. M., Torrey, H. C. & Pound, R. V. Resonance absorption by nuclear magnetic moments in a solid. *Physical Review* **69**, 37–38 (1946).

187. Todorov, Y., Sagnes, I., Abram, I. & Minot, C. Purcell enhancement of spontaneous emission from quantum cascades inside mirror-grating metal cavities at THz frequencies. *Physical Review Letters* **99**, 223603 (2007).

188. Gérard, J. M. & Gayral, B. Strong Purcell effect for InAs quantum boxes in three-dimensional solid-state microcavities. *Journal of Lightwave Technology* **17**, 2089–2095 (1999).

189. Fox, M. *Quantum Optics – An Introduction* (Oxford University Press, 2006).

190. Dini, D., Köhler, R., Tredicucci, A., Biasiol, G. & Sorba, L. Microcavity polariton splitting of intersubband transitions. *Physical Review Letters* **90**, 116401 (2003).

191. Anappara, A. A. *et al.* Signatures of the ultrastrong light-matter coupling regime. *Physical Review B* **79**, 201303 (2009).

192. Günter, G. *et al.* Sub-cycle switch-on of ultrastrong light-matter interaction. *Nature* **458**, 178–181 (2009).

193. Todorov, Y. *et al.* Strong light-matter coupling in subwavelength metal-dielectric microcavities at terahertz frequencies. *Physical Review Letters* **102**, 186402 (2009).

194. Zanotto, S., Biasiol, G., Degl'Innocenti, R., Sorba, L. & Tredicucci, A. Intersubband polaritons in a one-dimensional surface plasmon photonic crystal. *Applied Physics Letters* **97**, 231123 (2010).

195. Degl'Innocenti, R., Zanotto, S., Tredicucci, A., Biasiol, G. & Sorba, L. One-dimensional surface-plasmon gratings for the excitation of intersubband polaritons in suspended membranes. *Solid State Communications* **151**, 1725–1727 (2011).

196. Zanotto, S. *et al.* Ultrafast optical bleaching of intersubband cavity polaritons. *Physical Review B* **86**, 201302 (2012).

197. Laurent, T. *et al.* Short-wave infrared ($\lambda = 3$ μm) intersubband polaritons in the GaN/AlN system. *Applied Physics Letters* **110**, 131102 (2017).

198. Dietze, D., Benz, A., Strasser, G., Unterrainer, K. & Darmo, J. Terahertz meta-atoms coupled to a quantum well intersubband transition. *Optics Express* **19**, 13700–13706 (2011).

199. Dietze, D. *et al.* Ultrastrong coupling of intersubband plasmons and terahertz metamaterials. *Applied Physics Letters* **103**, 201106 (2013).

200. Geiser, M. *et al.* Strong light-matter coupling at terahertz frequencies at room temperature in electronic LC resonators. *Applied Physics Letters* **97**, 191107 (2010).

201. Geiser, M. *et al.* Ultrastrong coupling regime and plasmon polaritons in parabolic semiconductor quantum wells. *Physical Review Letters* **108**, 106402 (2012).

202. Wallace, P. The band theory of graphite. *Physical Review* **71**, 622–634 (1947).

203. Castro Neto, A. H., Peres, N. M. R., Novoselov, K. S. & Geim, a. K. The electronic properties of graphene. *Reviews of Modern Physics* **81**, 109–162 (2009).

204. Woessner, A. Exploring flatland nano-optics with graphene plasmons. *PhD thesis* (2017).

205. Ni, G. X. *et al.* Fundamental limits to graphene plasmonics. *Nature* **557**, 530–533 (2018).

206. Wunsch, B., Stauber, T., Sols, F. & Guinea, F. Dynamical polarization of graphene at finite doping. *New Journal of Physics* **8**, 318 (2006).

207. Hwang, E. H. & Das Sarma, S. Dielectric function, screening, and plasmons in two-dimensional graphene. *Physical Review B* **75**, 205418 (2007).

208. Eberlein, T. *et al.* Plasmon spectroscopy of free-standing graphene films. *Physical Review B* **77**, 233406 (2008).

209. Liu, Y., Willis, R. F., Emtsev, K. V. & Seyller, T. Plasmon dispersion and damping in electrically isolated two-dimensional charge sheets. *Physical Review B* **78**, 201403 (2008).

210. Zhou, W. *et al.* Atomically localized plasmon enhancement in monolayer graphene. *Nature Nanotechnology* **7**, 161–165 (2012).

211. Ju, L. *et al.* Graphene plasmonics for tunable terahertz metamaterials. *Nature Nanotechnology* **6**, 630–634 (2011).

212. Yan, H. *et al.* Tunable infrared plasmonic devices using graphene/insulator stacks. *Nature Nanotechnology* **7**, 330–334 (2012).

213. Yan, H. *et al.* Damping pathways of mid-infrared plasmons in graphene nanostructures. *Nature Photonics* **7**, 394–399 (2013).

214. Brar, V. W., Jang, M. S., Sherrott, M., Lopez, J. J. & Atwater, H. A. Highly confined tunable mid-infrared plasmonics in graphene nanoresonators. *Nano Letters* **13**, 2541–2547 (2013).

215. Fang, Z. *et al.* Gated tunability and hybridization of localized plasmons in nanostructured graphene. *ACS Nano* **7**, 2388–2395 (2013).

216. Jang, M. S. *et al.* Tunable large resonant absorption in a midinfrared graphene Salisbury screen. *Physical Review B* **90**, 165409 (2014).

217. Rodrigo, D. *et al.* Mid-infrared plasmonic biosensing with graphene. *Science* **349**, 165–168 (2015).

218. Watanabe, K., Taniguchi, T. & Kanda, H. Direct-bandgap properties and evidence for ultraviolet lasing of hexagonal boron nitride single crystal. *Nature Materials* **3**, 404–409 (2004).

219. Mayorov, A. S. *et al.* Micrometer-scale ballistic transport in encapsulated graphene at room temperature. *Nano Letters* **11**, 2396–2399 (2011).

220. Dean, C. R. *et al.* Boron nitride substrates for high-quality graphene electronics. *Nature Nanotechnology* **5**, 722–726 (2010).

221. Bandurin, D. A. *et al.* High electron mobility, quantum Hall effect and anomalous optical response in atomically thin InSe. *Nature Nanotechnology* **12**, 223–227 (2017).

222. Yin, G., Yuan, J., Jiang, W., Zhu, J. & Ma, Y. Plasmon-phonon coupling in graphene-hyperbolic bilayer heterostructures. *Chinese Physics B* **25** (2016).

223. Woessner, A. *et al.* Electrical detection of hyperbolic phonon-polaritons in heterostructures of graphene and boron nitride. *npj 2D Materials and Applications* **2** (2017).

224. Poddubny, A., Iorsh, I., Belov, P. & Kivshar, Y. Hyperbolic metamaterials. *Nature Photonics* **7**, 948–957 (2013).

225. Dai, S. *et al.* Tunable phonon polaritons in atomically thin van der Waals crystals of boron nitride. *Science* **343**, 1125–1129 (2014).

226. Caldwell, J. D. *et al.* Sub-diffractional volume-confined polaritons in the natural hyperbolic material hexagonal boron nitride. *Nature Communications* **5**, 5221 (2014).

227. Li, P. *et al.* Hyperbolic phonon-polaritons in boron nitride for near-field optical imaging and focusing. *Nature Communications* **6**, 7507 (2015).

228. Dai, S. *et al.* Subdiffractional focusing and guiding of polaritonic rays in a natural hyperbolic material. *Nature Communications* **6**, 6963 (2015).

229. Yoxall, E. *et al.* Direct observation of ultraslow hyperbolic polariton propagation with negative phase velocity. *Nature Photonics* **9**, 674–678 (2015).

230. Dai, S. *et al.* Graphene on hexagonal boron nitride as a tunable hyperbolic metamaterial. *Nature Nanotechnology* **10**, 682–686 (2015).

231. Ambrosio, A. *et al.* Mechanical detection and imaging of hyperbolic phonon polaritons in hexagonal boron nitride. *ACS Nano* **11**, 8741–8746 (2017).

232. Kurman, Y. *et al.* Control of semiconductor emitter frequency by increasing polariton momenta. *Nature Photonics* **12**, 423–429 (2018).

233. Lundeberg, M. B. Transfer matrix method calculator background. *unpublished work* (2016).

234. Zhan, T., Shi, X., Dai, Y., Liu, X. & Zi, J. Transfer matrix method for optics in graphene layers. *Journal of Physics: Condensed Matter* **25**, 215301 (2013).

235. Xia, F., Wang, H. & Jia, Y. Rediscovering black phosphorus as an anisotropic layered material for optoelectronics and electronics. *Nature Communications* **5**, 4458 (2014).

236. Qiao, J., Kong, X., Hu, Z. X., Yang, F. & Ji, W. High-mobility transport anisotropy and linear dichroism in few-layer black phosphorus. *Nature Communications* **5**, 4475 (2014).

237. Wieting, T. J. & Verble, J. L. Infrared and Raman studies of long-wavelength optical phonons in hexagonal MoS_2. *Physical Review B* **3**, 4286–4292 (1971).

238. Alcaraz Iranzo, D. *et al.* Probing the ultimate plasmon confinement limits with a van der Waals heterostructure. *Science* **360**, 291–295 (2018).

239. Kurman, Y., Schmidt, P., Koppens, F. & Kaminer, I. The ultimate Purcell factor in van der Waals heterostructures. *CLEO conference* (2019).

240. Goossens, A. M. *et al.* Mechanical cleaning of graphene. *Applied Physics Letters* **100**, 073110 (2012).

241. Cooper, L. N. Bound electron pairs in a degenerate Fermi gas. *Physical Review* **104**, 1189–1190 (1956).